The Dissertation Committee for Ryan Phillip Deschner Certifies that this is the approved version of the following dissertation:

Lithographic Patterning of Polymeric Media for Biotechnology Applications

Committee:

C. Grant Willson, Supervisor

Andrew Ellington

Christopher Ellison

Roger Bonnecaze

Brian Korgel

Lithographic Patterning of Polymeric Media for Biotechnology Applications

by

Ryan Phillip Deschner, B.S.Ch.E.

Dissertation

Presented to the Faculty of the Graduate School of

The University of Texas at Austin

in Partial Fulfillment

of the Requirements

for the Degree of

Doctor of Philosophy

The University of Texas at Austin

December, 2013

Dedication

To my wife, Katie.

Acknowledgements

This work would not have been possible without the strong support given to me by several individuals. I would first like to thank Dr. Willson for allowing me to be a part of his research laboratory and for giving me the opportunity to work him and the other great minds he surrounds himself with. It is only with his support, guidance, and penchant for challenging me that I have been able to become the researcher I am today. His integrity, his genuine enthusiasm for research, and his dedication to challenging and forming the minds of young scientists is truly something I aspire to.

I extend my heartfelt thanks to all of the members of the Willson Group for their collaboration and friendship, specifically: Dr. Saul Lee, Dr. Michael Jacobsson, Dr. Younjin Cho, Dr. Kane Jen, Dr. Todd Bailey, Dr. Michael Stewart, Dr. Andrew Jamieson, Dr. Elizabeth Costner, Dr. Chris Taylor, William Bell, Greg Blachut, Andrew Dick, Kelvin Lo, Alejandro Maurer, Brendan Foley, and Patrick Sermas. Special thanks to Cecilia Hall for her countless hours of work in the lab, excellent ideas, and centrifuging prowess; and to Rocco Hlis for his hard work and helpful discussions in the lab.

I would also like to thank Dr. Chris Ellison for his advice and friendship, and for always having an open office and laboratory door. I thank Dr. Andy Ellington for letting me and my undergraduates run rampant (and sometimes amok) in his laboratory and for his idea-packed, always enlightening, and never predictable conversations. Dr. Peter Allen also deserves many thanks for his high-quality conversations and for helping me trudge through experiments at all hours. I thank Dr. Georgiou and Brandon DeKosky for a terrific collaboration and their always-innovative approaches.

I would like to express my gratitude to my project partner, Dr. Hao Tang. I learned a great deal from working with you. Without your perseverance and knowledge of polymer synthesis, we would have never gotten to the final stage of the project. A special thanks to Dr. David Peyrade and the members of his laboratory for graciously hosting me at the CEA facility. I thank Dr. Thibault Honegger for his helpful conversations and ideas regarding my projects.

I extend my gratitude to my incredible parents Bob Deschner and Susan Suchecki for their constant love and support no matter what I've gotten myself into. Thank you both for instilling in me a love of learning and always being there for me. I thank my grandfather, Reinhart Deschner, for his moral guidance and inspiring my enthusiasm for tinkering. I thank Blake and Alma Pizzolato for treating me like their own son and constantly traveling to Austin to help out with my family. Without Alma's tireless support, this work certainly would not have been possible. I'd also like to thank Burns Cleland for his candor, his kind friendship and for letting me run wild in his machine shop unsupervised; and Karen Cleland for always being there for me and teaching me resourcefulness and how to laugh at myself. Thanks to Lapin for always being at my side through the late nights studying and writing. Thank you to my son, Sam, for inspiring me and keeping me company during the wee hours.

Finally, I would like to thank my wife, Katie, for even entertaining the idea of me leaving a stable job and going back to graduate school, and for putting up with all of the late nights and weekends in the lab for five and a half years. Thank you for believing in me, supporting me, keeping my head out of the clouds, and challenging me. You have gracefully stood beside me throughout all of the craziness, and if it weren't for you I would probably still be eating Ramen out of a coffee pot. You are truly a formidable human being, a terrific mother, and great partner.

Lithographic Patterning of Polymeric Media for Biotechnology Applications

Ryan Phillip Deschner, Ph. D

The University of Texas at Austin, December 2013

Supervisor: C. Grant Willson

Lithographic patterning has heavily utilized in the semiconductor industry for its ability to pattern vast numbers of complex shapes down to the nanometer scale. However, only recently has this technology been employed in the biotechnology field despite the fact that most of that the most important biological components such as cells, antibodies, DNA and proteins operate at this level. This work is an exploration of the use of lithographic printing methods in two areas deeply-entrenched in biotechnology: self assembly and microarray-based manipulation of biological media. It was inspired by the natural self assembly which occurs in nature and in our bodies at all scales. The majority of this work dealt with the patterning of bioreactive copolymers into different three-dimensional microshapes which could be functionalized with single strands of DNA for subsequent sequence-specific particle assembly. This type of technology, where very small-scale matter can be directed to self assembly into programmed macrostructures in a highly-specific manner has the capability to be adapted for many next-generation applications in drug delivery, nanofabrication, biosensing, and microelectronics.

A secondary technology was explored in this work involving the paired sequencing of antibody gene sequences with the aid of lithographically-patterned microarrays. This methodology represents a bridging of bottom-up fabrication methods

of DNA and proteins with top-down optical fabrication techniques which is already finding increasing utility in applications such as vaccine discovery, diagnostics, and autoimmune research. Because of the versatile nature of the components of this research, it is the hope of the author that the techniques discovered and explored here provide support and inspiration for future research in the biotechnology field as well as in other fields which may benefit as well.

Table of Contents

List of Tables

List of Figures

Chapter 1: Introduction to DNA-Mediated Self Assembly

1.1 Characteristics of Self Assembly

Self assembly can be described as the spontaneous and autonomous organization of matter into patterns demonstrating a higher state of order.[1] This phenomenon is ubiquitous in the world around us, appearing at size scales from the organization of galaxies and solar systems to the crystalline shapes of snowflakes. Self assembly processes can generally be decomposed into a few elements: some type of building block, associative forces, and dissociative forces. The building blocks can be any type of matter from individual molecules such as phospholipids and DNA, to macroscopic materials such as crystals, cells, polymer domains, and nanoparticles. These building blocks must also have the ability to move around so that the balance of the associative and dissociative forces acting between these mobile building blocks can serve as the fundamental driving force for the organization to more ordered states. Changes to the environment of the system such as the introduction of thermal energy, pressure changes, new chemical species, shear, or electric field have the capability of shifting the steady state balance of the forces to promote new, higher levels of order simultaneously for vast multitudes of building blocks.

1.2 Self Assembly in Nature

The main motivation for self assembly research is the potential to produce advanced materials with superior properties that can be controlled and exploited in a wide range of applications. Scientists often turn to nature for inspiration in developing advanced materials because millions of years of evolution and natural selection have

yielded biological organisms which make use of self assembly to find food, protect themselves from predators and the elements, reproduce, and resist disease. An interesting example of this is the shell of Haliotis refuscens (red abalone). This sea snail has a shell which is formed by the biological assembly of sheets of calcium carbonate (aragonite) crystal sandwiched in between layers of viscoelastic proteins[2] (Fig. 1.1). The abalone secretes protein and minerals from its mantle tissue to form organized aragonite tiles in layers in order to protect the soft organs of the organism. This composite material is essentially a ceramic with excellent compressive and tensile strengths which are much greater than those of the individual components.

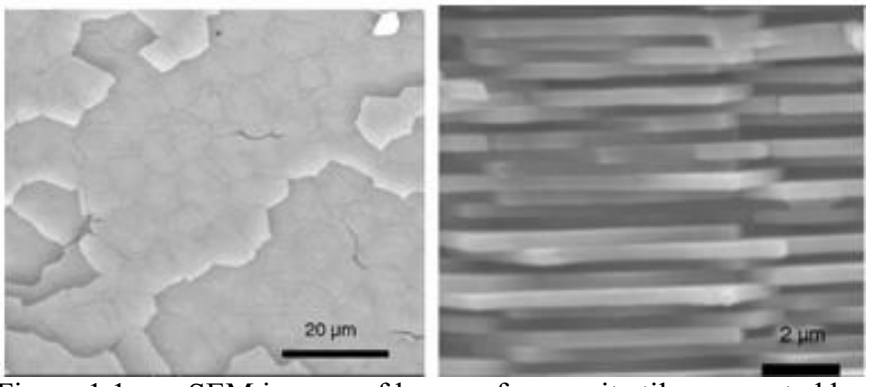

Figure 1.1: SEM images of layers of aragonite tiles separated by a protein matrix. *Reprinted with permission from*[2].

At smaller scales, biological cells are rife with different hierarchies of self assembly activity. They are encompassed by membranes which are made up of amphiphilic phospholipid molecules which self assemble into bilayer membranes to protect and retain the contents of the cell. These amphiphilic molecules[3], comprising a hydrophilic head and a hydrophobic tail organize themselves into tightly-packed non-covalent bilayers in an attempt to minimize the exposure of the hydrophobic tails to the aqueous solution (Fig. 1.2) when exposed to aqueous solutions. The non-polar

component in the cell wall makes these bilayers very effective at keeping out aqueous-soluble molecules which could damage the cell; however, they can also incorporate proteins into their structure to allow for the controlled flow of ions into the cell.

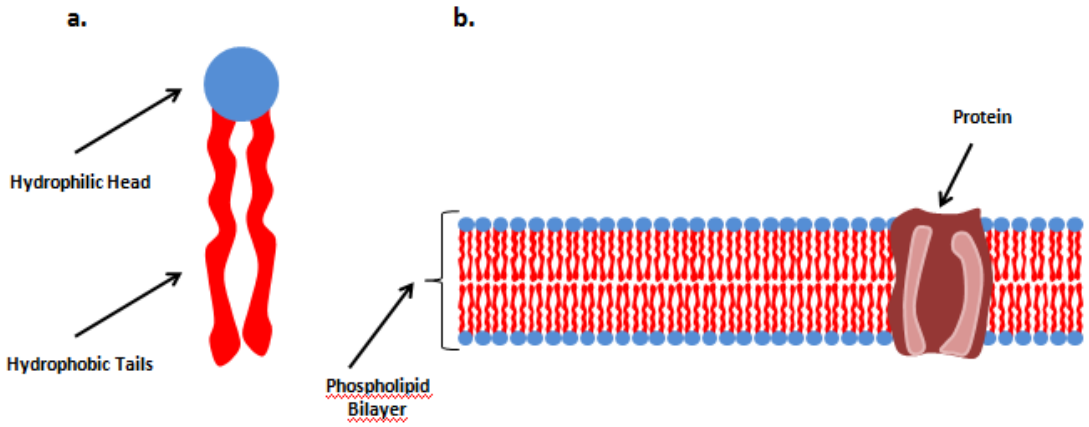

Figure 1.2. Structures of a. phospholipid molecule and b. cross section of bilayer cell membrane including a protein channel.

Inside the cell nucleus, the genetic information required for the development of all living organisms is encoded in the deoxyribonucleic acid (DNA). It is constructed from long polymer-like strands comprising covalently-bound combinations of four different types of building blocks called nucleobases (guanine, cytosine, adenine, and thymine) held together by a phosphate-sugar backbone. DNA usually exists in two nucleobase-complementary single strands of DNA that assemble into double helices via hydrogen bonding between the nucleobase pairs. Replication of the double-stranded DNA occurs when DNA helicase disrupts the hydrogen bonding of the base pairs, unzipping the double helix into two individual strands. Nucleobases bound to sugar and phosphate groups, known as nucleotides, assemble onto the single-strand DNA scaffold by pairing with only complementary nucleotides and then polymerizing incrementally into the new double helix with the help of a DNA polymerase enzyme. Each single strand of the

original double helix fully assembles with a complementary sequence eventually producing two new double helices from the original as shown in Figure 1.3.

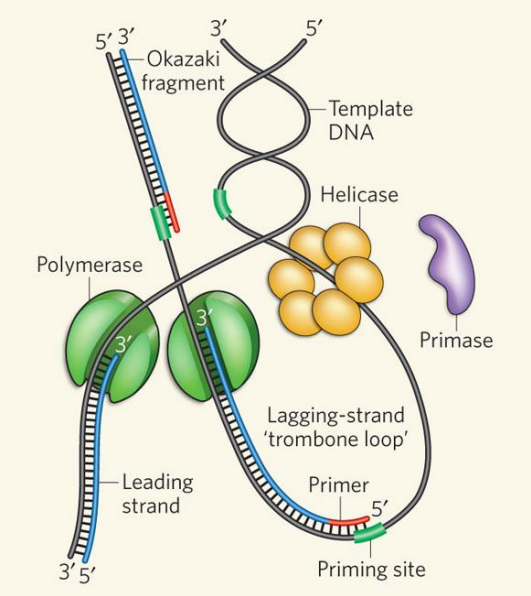

Figure 1.3. Schematic of the DNA replication process. *Reprinted with permission from* [4].

At a higher level of self assembly, double-stranded DNA self-assembles into larger macrostructures called chromosomes along with RNA and structural proteins to prepare themselves for cell division, or, mitosis. Chromosomes are formed in the process of DNA compaction whereby very long, single molecules of double-stranded DNA are first wrapped around structural proteins (histones) to form nucleosomes which shorten the end-to-end length. The DNA-nucleosome hybrid further assembles into tightly-wound DNA fibers called chromatin with a diameter of 30 nanometers[5]. These fibers wrap themselves around more structural proteins to further condense the DNA and shorten its length until roughly a few centimeters of genetic code has been condensed into a chromosome that is a few micron in size.

These highly-organized, densely-packed self assembly hierarchies allow for all of the genetic information, equivalent to about 2 meters of DNA, needed to produce a human being to fit inside a cell has roughly one fourth the diameter of a single human hair. At its highest packing ratio, this complex self assembly methodology also converts the thin strand of DNA into a much stronger macrostructure capable of withstanding the harsh conditions of cell mitosis. It is evident that the entire development of the human body is guided by increasingly higher orders of self assembly beginning at the nanometer scale and continuing all the way up to the visible scale of organs and tissue. Furthermore, the DNA displays remarkable accuracy and energy efficiency[6] during the replication process, and even has a mechanism for correcting sequence errors in real time[7].

1.3 APPLICATIONS OF SELF ASSEMBLY RESEARCH

As researchers develop more and more powerful techniques for observing units of matter at increasingly smaller scales, the desire to control, manipulate, and organize these units has driven a vast and diverse range of techniques targeting a multitude of valuable applications. In the latter half of the 20th century, scientists have made great strides in producing large numbers of highly organized materials down to the nanometer scale. The microelectronics industry has pushed the limits of microscopic patterning using techniques such as chemical vapor deposition, sputtering of metals, photolithography, liquid and gas phase etching and chemical mechanical polishing. Such advances have driven feature dimensions for use in semiconductor devices from the millimeter scale down to the tens of nanometer scale and below[8]. Researchers at IBM[9] in 1990 were even able to manipulate single xenon atoms into precise locations on a crystal nickel substrate

to generate an Angstrom-scale company logo with a scanning tunneling microscope (STM). Sophisticated imaging techniques have also been developed to characterize these patterns such as scanning electron microscopy (SEM), transmission electron microscopy (TEM), atomic force microscopy (AFM) and scanning tunneling. However, these top-down techniques generally utilize several external subtractive and additive operations to a larger bulk material to produce such small, organized features and convert energy into states of higher order very inefficiently. Self assembly represents an alternative bottom-up solution for fabricating complex, highly-ordered nanostructures which often enjoy the benefits of higher feature resolution, fewer process steps, more efficient use of energy, and the capability of operating as dynamic systems.

A novel application of practical self assembly is the formation of self assembled monolayers. Monolayer films of single-molecule thickness can be adsorbed or covalently bound to substrates to modify characteristics of the surface such as adhesion for subsequent processing steps. For example, the treatment of templates with fluorinated silanes in step-and-flash imprint lithography[10] can promote facile release of the template from the resist pattern by lowering the surface energy of the template leading to defect reduction over several imprints (Figure 1.4). Conversely, species such as alkyl siloxanes or alkyl thiols can be deposited onto poly(dimethyl siloxane) (PDMS) templates and then subsequently stamped onto silicon or gold substrates[11], respectively, yielding monolayer patterns which can be subsequently etched and processed using microelectronic fabrication techniques without the employment of expensive lithography tools.

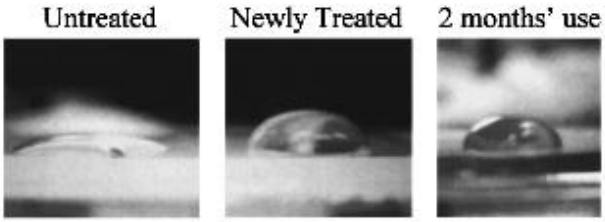

Figure 1.4. Images of a water droplet on the surface of a template used for Step-and-Flash imprint lithography a. before and b. after treatment with a fluorosilane SAM; and c. after 2 months of imprint use. *Reprinted with permission from* [10].

At larger dimensions of molecular assembly, block copolymers have been studied extensively for their ability to orient themselves into organized phase domains at large scales. Block copolymers can be synthesized with two or more immiscible homogenous sequences of monomer unit. In bulk films, these blocks self assemble into well-defined types of morphologies[12] where the constituent blocks of each copolymer aggregate to achieve energetically favorable configurations. AB diblock copolymers form very useful morphologies including hexagonally-packed cylinders[13], lamellae[14], body-centered-cubic spheres, and bicontinuous gyroids in the nanometer regime as shown in Figure 1.5.

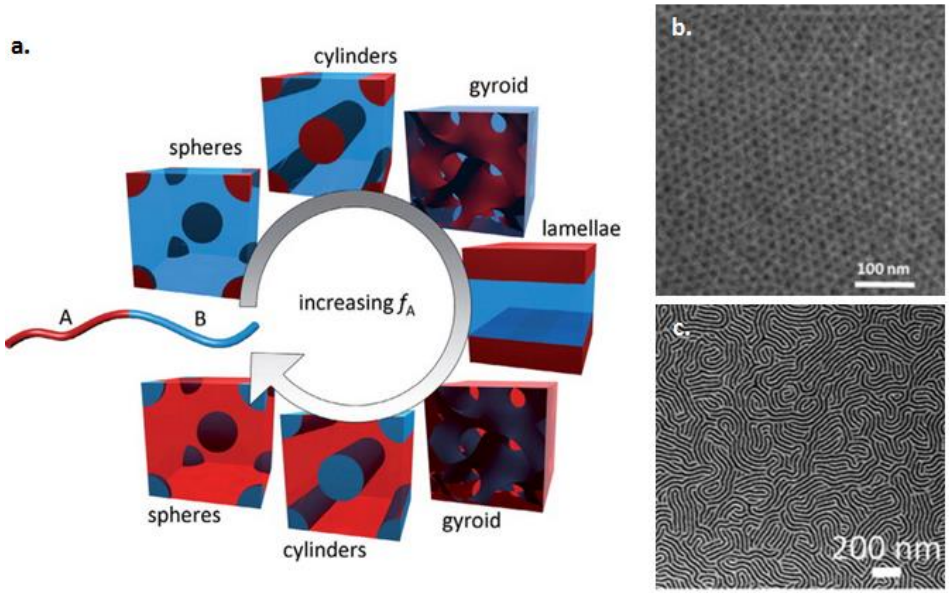

Figure 1.5. a. Domain morphologies of bulk diblock copolymers as a function of fraction of block A (red). SEM images of b. etched block copolymer cylinders and c. lamellae. *a. Reprinted with permission from [15], b. Reprinted with permission from [13], c. reprinted with permission from [14].*

It is easy to imagine the utility of such lamellar, spherical or cylindrical morphologies used in conjunction with an etch process to selectively remove one of the block domains in nanopatterning applications for microelectronics. In fact directed self assembly of polystyrene-poly(methyl methacrylate) (PS-PMMA) diblock copolymer lamellae by lithographically-printed gratings has been demonstrated[16] which could be adapted to the formation of integrated circuit features below 20 nm. Simarly, PS-PMMA cylinder morphologies have also been used to create large arrays of magnetic metal dots with the goal of adapting this process to magnetic data storage[17] devices.

Liposomes behave in a manner similar to bulk diblock copolymers, self assembling into complex three-dimensional structures dependent on their immiscible components. They are generally lipids or block copolymers that comprise a hydrophobic component and a hydrophilic component, allowing them to form bilayer sheets just as

phospholipids in cellular membranes do. In dilute aqueous solutions, they efficiently self assemble in into stable capsule-like shapes (Fig 1.6) which are highly resistant to aqueous permeation.[18] These structures can be assembled in solutions containing agents such as chemotherapy drugs or ssDNA, effectively loading their inner volume with a secured cargo that can injected into the body. Programmed release of the drug cargo is also possible by decorating the surface of the liposomes with ssDNA[19], or antibodies[20], which can target specific cells or areas in the body for delivery. These structures have already found important applications in the targeted delivery of anti-cancer drugs, vaccines, and antibiotics; and they have also been loaded with other cargo such as fluorophores[21], ssDNA[22], and electronic[23] markers for use in very sensitive biosensor applications.

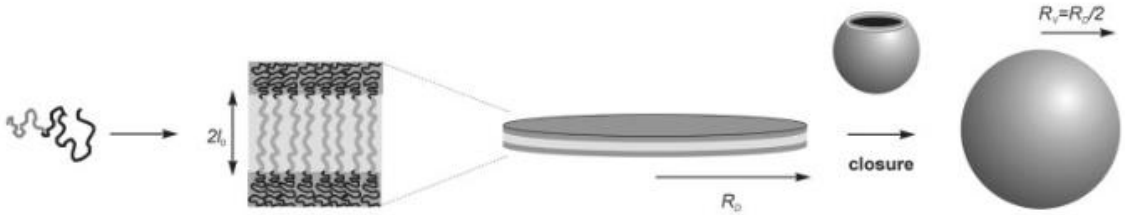

Figure 1.6. Schematic of the formation of amphiphile bilayers and the process for their closure into liposomes. *Reprinted with permission from* [18]

At even larger scales, bulk particles of materials such as polymers and metals have been used as building blocks for creating highly-organized macrostructures. Capillary force assembly can be used to draw arrays of fixed[24] or mobile[25,26] structures together using strong capillary forces at liquid interfaces (Figure 1.7). These associations can be used to control aggregation of media on surfaces or at liquid interfaces, or with incorporation of species such as ssDNA for use in biosensor applications detect analytes in aqueous solutions[27]. This type of self assembly is useful for creating arrays and aggregates with long-term order; however it lacks the independent ability to form more

complex structures of which other self assembly schemes such as diblock copolymers are capable.

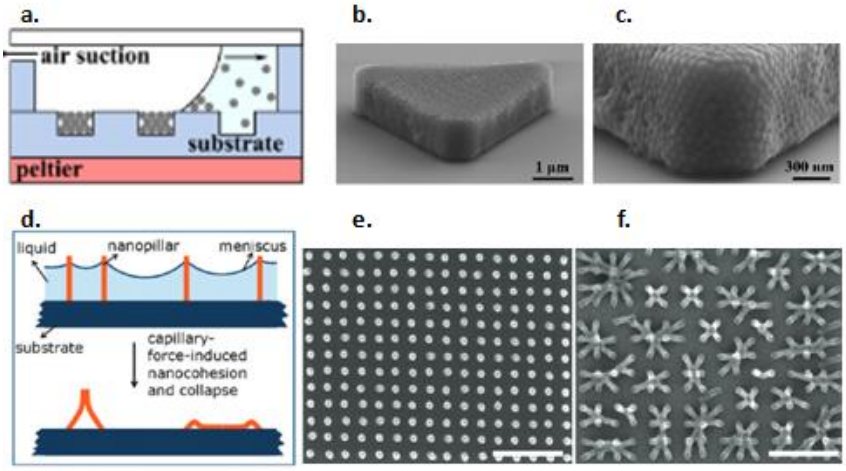

Figure 1.7. a. Schematic of the capillary force assembly of liposomes. b. SEM image of triangular aggregates of polystyrene nanobeads. c. Zoomed in SEM of aggregates. d. Schematic of the capillary force assembly of PMMA nanopillars. SEM images of PMMA nanopillars e. before and f. after assembly. *a-c. Reprinted with permission from* [26]. *d-f. Reprinted with permission from* [24].

1.4 DNA-FACILITATED SELF ASSEMBLY

Another exciting subfield of self assembly that borrows from natural phenomena is DNA-facilitated self assembly. Since the discovery of its structure in 1953, DNA has been a very attractive candidate for the associative driving force between building blocks because it is highly specific, it is dynamic in that the reversibility of its binding can be controlled[28], and it operates at very small size scales where Brownian motion is dominant. In self assembly applications, it can be used as both the building block and the coupling media or as just the coupling media for larger bulk materials. The advantage of DNA-assisted self assembly of other associative media is that it imparts a programmable

nature to the associations, allowing for controllable coupling which can be modified by changing the sequence coding or chain length of the DNA.

DNA is itself self-assembled from nucleobases, deoxyribose sugars, and phosphate groups to form long chains of coded sequences which are generally found hybridized in pairs in helical form. The four base pairs: guanine (G), cytosine (C), adenine (A), and thymine (T), which serve as the unique building blocks for DNA associate only with their designated complement (G binds with C and A binds with T) via hydrogen bonding, known as Watson-Crick base pairing. This association is non-covalent in nature and allows for the individual strands to reorganize at relatively low energies. Because the hybridization strength of DNA is a function of the number and type of interacting base pairs, the strength of the particle associations can be tuned to the desired level. In addition, temperature and salt concentration can also be tuned to manipulate binding strength.

Since the advent of oligonucleotide synthesis in the 1950s, synthetic DNA technology has advanced to the point where single-strand DNA (ssDNA) can be manufactured relatively cheaply up to 100 nucleobases in length and with a wide range of terminal functional groups such as amines, thiols, aldehydes, fluorophores, and alkyl and polyethylene glycol (PEG) spacers. The availability of these sequences led to the first reports of synthetic DNA structures in the early 1980's. In 1982, Seeman et al[29] first assembled ssDNA into four-way junctions and higher-order lattices by designing strands that have multiple sections which are complementary to sections of other strands (Fig. 1.8). The component ssDNA strands were mixed together in a buffer solution and temperature cycled to yield the desired shapes. This groundbreaking work kicked off a new field known as structural DNA nanotechnology which is essentially the study of the

fabrication of complex nano-scale structures formed by the specific interactions of strands of DNA.

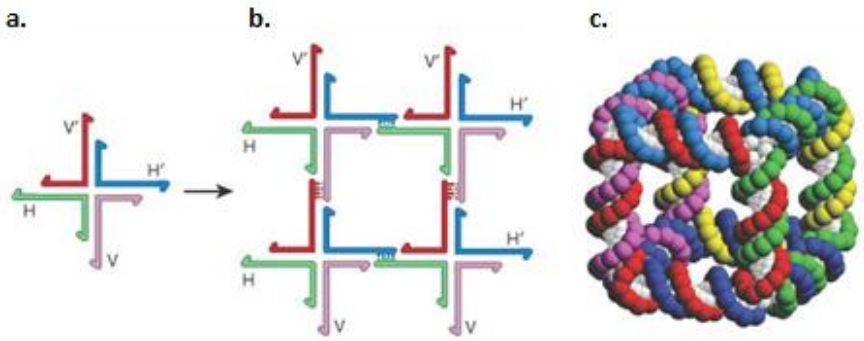

Figure 1.8: Self assembly of DNA molecules into a. a self assembled junction with sticky overhands (V, V', H, and H') and b. a superlattice of DNA junctions. c. Assembly of double-crossover DNA units into a polyhedron. *a-c. Reprinted with permission from* [30].

Seeman et al[31] later made improvements to the technology, adding more rigidity to the structures by incorporating stick-like building blocks called "double-crossover molecules" (DX molecules) made up of two intertwined double helices laced together at two points with ssDNA which participates in hybridization on both helices. These units can be constructed into polyhedron formations as shown in Figure 1.8c. The formation of these building blocks shares many similarities with DNA packing of nucleosomes and chromatin into chromosomes to prepare for cell division. It also exploits the enhanced structural integrity of the double helix configuration.

In 2006, Rothemund[32] folded very long (~7,000 nt) single-stranded virus DNA into "DNA origami" using large numbers of pre-designed connective "staple" strands in a manner structurally similar to DX molecules. The hundreds of 10-20 nt staples used were designed to be complementary to two or more sections of the virus DNA sequence to force spontaneous assembly of the virus DNA into intricate shapes such as stars, smiley faces, and map projections (Fig. 1.9). The self assembly in DNA origami would be

fundamentally impossible without the power of DNA to selectively hybridize many unique sequences of staples only to the portions of the virus DNA that they were designed for.

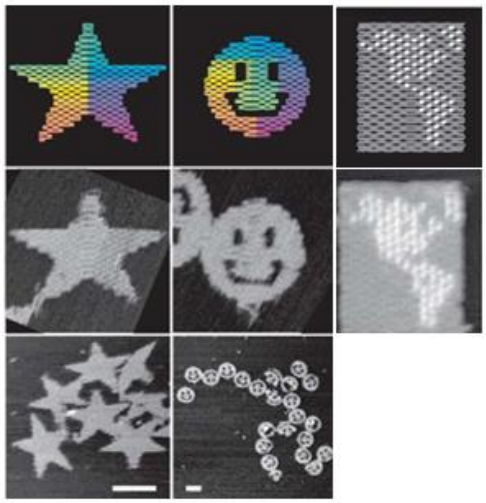

Figure 1.9. Design graphics and SEM images of DNA Origami shapes formed by folding 7,249 nt virus DNA with the aid of DNA "staple" strands. *Reprinted with permission from* [32].

Dynamic self assembly of DNA has also been demonstrated. Gu et al[33] constructed ssDNA tracks on a substrate and ambulatory "walker" DNA junctions which were capable of moving along the substrate as different strands of the walker were substituted which hybridized with the different points along the track. This technique is enabled by the ability of DNA to spontaneously swap single strands already hybridized to the walker and the track in the presence of new strands with larger affinities for the walker and then track; meaning that new strand hybridizes more base pairs than the former. These walkers were also capable of capturing and delivering ssDNA-functionalized gold nanoparticles to a location at the end of the track, incorporating a form of composite DNA nanotechnology. This swapping of ssDNA with higher hybridization affinities shows off the dynamic capabilities of DNA construction.

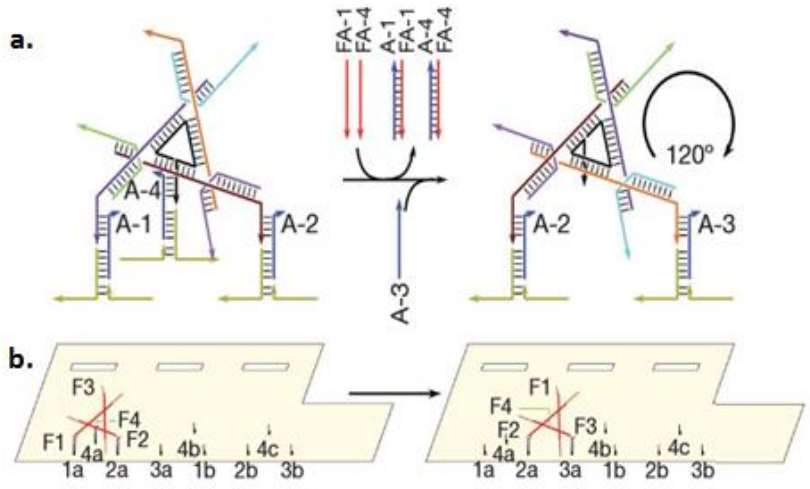

Figure 1.10. The dynamic movement of a. DNA "nanowalker" structures on a b. DNA track. The rear "leg" of the nanowalker moves to the "head" position as the "head" moves to the front "leg" position at the next station on the track via the swapping of ssDNA with higher hybridization affinities. *Reprinted with permission from* [33].

Composite DNA nanotechnology employs DNA as a "smart glue" rather than as a structural component to assemble larger building blocks into organized configurations. Composite DNA nanotechnology lacks the specificity of structural DNA nanotechnology, but it has a greater range of material options and is not constrained by the cost of custom-designed ssDNA. Gold nanoparticles were among the first non-DNA building blocks to be assembled with this technology because they can be easily covalently functionalized with thiol-terminated ssDNA, they can be produced in large quantities at easily-tunable sizes via citrate reduction chemistry[34], and they have very attractive optical and electronic properties. Mirkin et al[35] functionalized gold nanoparticles with thiolated ssDNA and then introduced an ssDNA linker strand to induce aggregation of the gold particles. They also showed that this process could be completely reversed by increasing the system temperature above the melting point of the DNA hybridizations. In the same journal edition, Alivisatos et al[36] reported the assembly of gold nanoparticle dimers and trimers

and characterized them using gel electrophoresis. Kim et al[37] also successfully demonstrated the formation of unit nanometer-scale gold-DNA conjugates in which the ssDNA is laid out in several different empirical configurations based on steric hindrance.

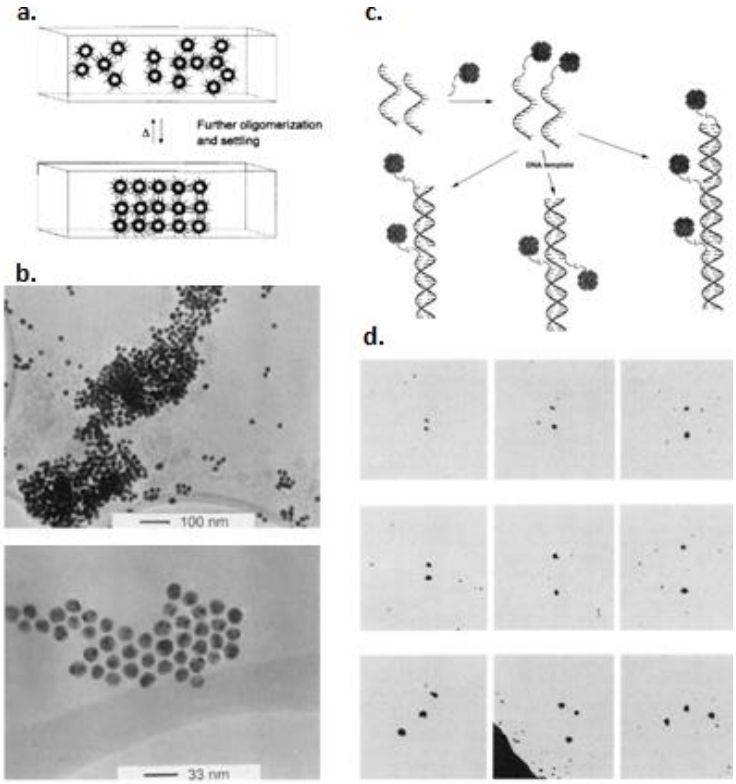

Figure 1.11. a. Schematic of reversible hybridization and b. SEM images of the aggregation of ssDNA-functionalized gold nanoparticles. c. Schematic of reversible hybridization and d. SEM images of dimer and trimer ssDNA gold nanoparticle assemblies. *a. Reprinted with permission from [35]. b. Reprinted with permission from [36].*

These experiments have led to many useful applications of DNA-functionalized gold particles which can be used as vitro biosensors with femtomolar sensitivities[38], in vivo carriers which can transfect through cellular membranes to deliver DNA for gene therapy[39, 40], and bio-barcode probes for detecting cancer biomarkers coupled to magnetic beads which very high sensitivity[41]. These technologies have even been developed to the

point that they have become the basis for several successful biotechnology companies. Other materials have been used as the building blocks in composite DNA technology. Functionalized magnetic particles such as iron oxide can be used to hybridize DNA and mRNA in solution for purification processes[42, 43] that do not require centrifuging or electrophoresis. DNA-functionalized polymer particles such as polystyrene-based beads can also be used to purify DNA with the help of centrifugation[44, 45].

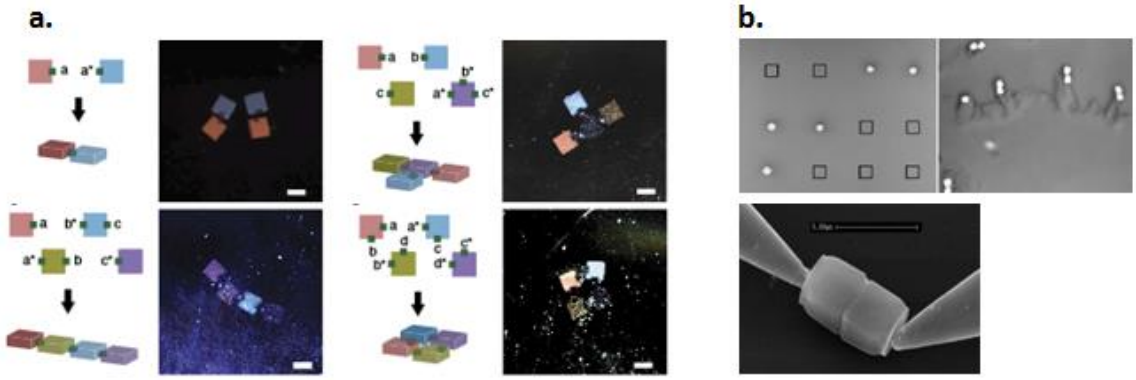

Figure 1.12. a. Cubic poly(ethylene glycol) (PEG) hydrogel superparticles assembled into dimmers, chains, T-junctions, and a 2 x 2 array. b. ssDNA functionalized silicon cubes assembly and electrical testing with probes. *a. Reprinted with permission from [46]. b. Reprinted with permission from [47].*

Two-part composite spherical particles called Janus particles have been produced which consist of two different "sides" which can be independently functionalized with ssDNA containing different terminal groups. Siloxane-acrylate-based Janus particles have been liquid-extruded in a microfluidic device with both a hydrophilic and a hydrophobic hemisphere.[48] Janus particles fabricated by sputtering gold onto polystyrene beads[49] can also be used to selectively functionalize ssDNA to different hemispheres. These particles are still geometrically single-sided (spherical), but they exhibit dual-functionality because they are composed of two different materials. More recently,

hydrogel cubes crosslinked with ssDNA primers were printed photolithographically, using a polymerase reaction to create a "giant DNA" functionalization on the surfaces.[46] Larger cubic shapes containing different ssDNA in the hydrogel matrix were also printed over two or three of the smaller cubes with a lithography tool with mask-to-substrate alignment capability to produce "supercubes" with multiple partially-functionalized facets containing different ssDNA sequences. These cubes were assembled into dimers, chains, T-junctions and two-dimensional arrays. In addition, DNA-assisted assembly of truly polyfaceted particles[47] has been reported by reactive ion etching silicon cubes on a SiO_2 lift-off layer using a photoresist mask. A self assembled monolayer of an aminosilane was bound to the surfaces of the cubes for glutaraldehyde conjugation with amine-terminal ssDNA sequences.

1.5 PROJECT OBJECTIVES

Many novel DNA-building block combinations have been explored and applied in useful applications in composite DNA nanotechnology. This self assembly has led to configurations such as dimers, chains, aggregates, T-junctions, and arrays. However, at the time of the writing of this dissertation, programmable 3-dimensional self assembly of particles on the micron and nanometer scales has yet to be demonstrated. This scientific breakthrough requires the generation of polyfaceted particles with a processing scheme that allows for the independent functionalization of different ssDNA sequences to three or more faces of the particles. The goal of this project is to develop the unit operations necessary to fabricate polyfaceted DNA-functionalized particles using adaptations of modern photolithography techniques combined with surface functionalization chemistry.

Once this has been established, these polyfaceted particles can be assembled into limitless programmable configurations, providing for the easy assembly of highly-complex nanostructures such as nanoscale gears for nanorobotics, smart capsules for drug delivery, or advanced nanostructured surfaces for improved catalyst performance.

.

1.6 PROCESS OUTLINE

The proposed process flow for the fabrication of polyfaceted DNA-functionalized parallelepipeds is outlined in Figure 1.13. First, a film stack consisting of the thick patternable and bioreactive copolymer over a thin sacrificial lift-off layer (LOL) is spin-coated onto a bare silicon wafer (Fig. 1.13a). The first sequence of ssDNA (ssDNA A) is covalently bound to the surface of the copolymer (Fig. 1.13b) followed by a rinse and exposure to a blocking agent to passivate any unreacted sites to render them unreactive toward further covalent substitution. Following the functionalization and blocking procedure to the top surface if the film, it is irradiated through a chromium-on-glass (COG) quartz photomask with large arrays of grating structures (Fig. 1.13c). The pattern is then developed to remove the exposed copolymer in the irradiated regions. The sides of the line patterns in the grating present newly exposed reactive surfaces, which are functionalized with a second ssDNA sequence (ssDNA B) (Fig. 1.13d). After a second blocking step the mask is rotated 90° and a second irradiation of the stack is performed (Fig. 1.13e). The pattern is developed a second time to yield large numbers of parallelepipeds whose newly-exposed sides are then functionalized with ssDNA C (Fig. 1.13f), followed by another blocking step. In the final fabrication step, the particles are lifted off of the substrate by dissolving the LOL (Fig. 1.13g) and the parallelepipeds are

functionalized in solution with ssDNA D (Fig. 1.13h). This proposed process flow is capable of generating particles with six different sides and four different (A-D) ssDNA functionalizations.

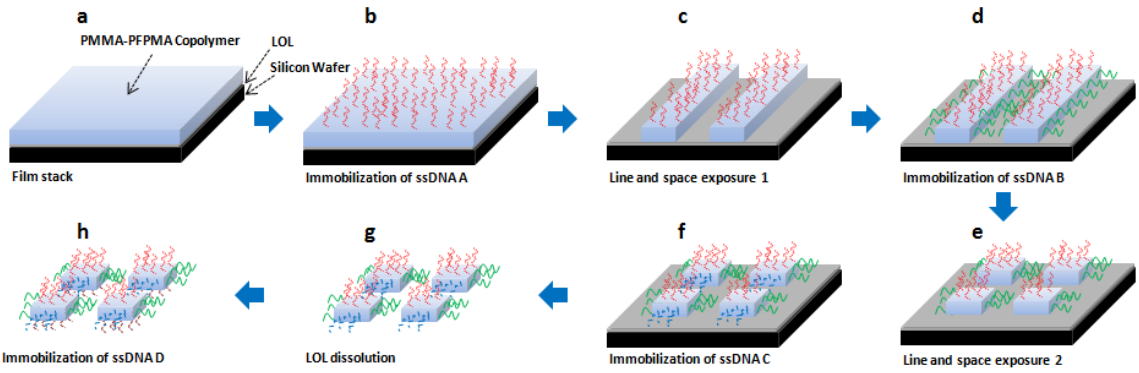

Figure 1.13: Fabrication process flow for ssDNA-functionalized polymer particles: a. The LOL and copolymer are spin-coated onto a bare silicon wafer followed by the b. ssDNA A immobilization and block. Next a c. line and space grating is exposed into the copolymer and developed, followed by d. the immobilization of ssDNA B. The e. second line and space pattern is exposed and developed, and followed by f. the ssDNA C immobilization and block. Finally, the particles are g. lifted off the substrate in LOL stripper and h. ssDNA D is immobilized to the bottoms of the particles.

This process flow is designed to be compatible with a non-aligning contact lithography system without mask-to-substrate alignment capability. The generation of particles with six different ssDNA functionalizations on six different sides is also possible with this same basic process flow; however, four different exposures are required as well as a lithography tool with a sophisticated alignment system.

1.7 Outline of Dissertation

This dissertation is primarily a summary of scientific research performed for the purpose of developing a 3-dimensional DNA-assisted programmable assembly process.

The first six chapters catalog the development of each unit operation of the 3-dimensional self assembly process followed by a single chapter on the high-throughput microwell-based paired sequencing of antibodies. Chapter 2 describes the optimization of the photolithographic patterning of the particles. Chapter 3 is an analysis of the techniques used to functionalize the particles and characterize the presence of ssDNA on their surfaces. In Chapter 4, the development of a robust sacrificial lift-off layer is presented. In Chapter 5, several studies exploring the specific details of the carbodiimide-based DNA coupling reaction are presented in which carboxyl-functionalized polystyrene microspheres are used as an analog for the patterned acrylate polymer particles. Chapter 6 is an analysis of the results for the DNA-assisted self assembly of the particles including conclusions and a description of future work. Finally, Chapter 7 is a self-contained chapter which entails an introduction to high-throughput antibody sequencing, a description of the work executed in the development of a functioning microwell array-based platform, and a summary of the sequencing results achieved.

Chapter 2: Patterning of Dual-Functional Materials

2.1 LITHOGRAPHY PLATFORM

In 1947, William Shockley, Walter Brattain, and John Bardeen developed the first solid state transistor at Bell Labs, surpassing the current vacuum-tube-based technology. This work was later integrated with p-n junctions to create a bipolar transistor platform, and in 1958 and 1959, respectively, Jack Kilby at Texas Instruments and Robert Noyce at Fairchild Semiconductor independently developed the first working monolithic integrated circuit (IC) which is the basis for modern-day solid state devices. This work catalyzed the birth of the modern semiconductor industry and put the dream of personal computing within reach. This led to the need for a technology which could shrink down integrated circuit designs in order to print extremely large numbers of transistors onto increasingly smaller silicon chips for the purpose of advanced computing and data storage. Modern projection photolithography was introduced in 1970's and established itself as the primary method for printing integrated circuits for microelectronic devices. Since then, the density of transistors per unit area has increased steadily year after year. In 1965, an engineer at Intel Corporation named Gordon Moore made the famous observation that integrated circuit densities tend to double every year. This prediction, known as Moore's Law, has remained roughly accurate to this day and is the basis for the International Technology Roadmap for Semiconductor (ITRS) which serves as a technology development guide for semiconductor manufacturers.

Photolithography is a top-down, subtractive imaging technique that is capable of transferring vast numbers of two-dimensional shapes into a photosensitive polymer using actinic light. Instead of directly patterning the wires and interconnects needed for ICs,

photolithography prints photoresist structures such as gratings which can be printed onto semiconductor or metallic substrates to physically mask an etch process. An example of a general photolithography-etch process is outlined in Figure 2.1. First, photoresist is coated onto the surface of a silicon wafer, generally by a spin-coating process. The wafer is then exposed with a light source at the desired wavelength through a mask with opaque (chromium) regions and clear (quartz) regions, transferring the mask pattern into the photoresist. In a positive resist scheme, the areas which are exposed to the light through the clear regions of the mask become more soluble in developer. Conversely, in a negative resist scheme, the areas which are exposed to light become more insoluble in developer. After selective development, the photoresist patterns are generally transferred into a metal, silicon, or polycrystalline silicon substrate via wet chemical or reactive ion etching (RIE). The photoresist is typically stripped away with a plasma ashing process, resulting in a complete transfer of the mask pattern into the substrate of choice. In a typical IC device manufacturing process, this process is repeated several times in conjunction with further processing steps such as chemical mechanical polish (CMP), ion implantation, RIE, and metal deposition.

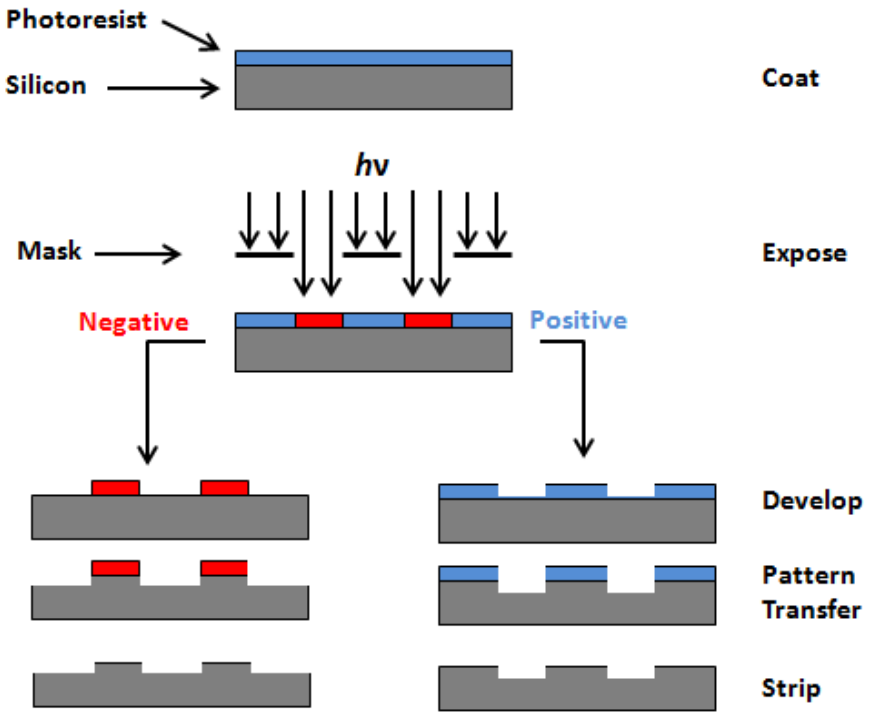

Figure 2.1 General process flow for a lithography process flow for positive and negative photoresists including etch and resist stripping steps.

The main advantage of projection photolithography is that it can be scaled down to very small feature resolution following Rayleigh's Law:

$$R = k_1 \frac{\lambda}{NA} \tag{2.1}$$

where R is the minimum resolution of the feature, k_1 is a system-dependent parameter, λ is the wavelength of the incident light, and NA is the numerical aperture of the lens. The resolution of the printed feature is proportional to the k_1 factor and the wavelength of light used and inversely proportional to the numerical aperture. Current lithography systems in state-of-the-art semiconductor manufacturing sites use 193 nm light to print half-pitch features at 22 nm for working memory and processor devices.

2.2 PHOTOLITHOGRAPHY PLATFORM

For this project, a deep-UV (DUV) mercury arc lamp source was selected because it is relatively inexpensive and it generates light that is absorbed by thin films of poly(methyl methacrylate) (PMMA). PMMA is a basic positive photoresist that can be patterned with DUV contact lithography, meaning that during exposure the photomask comes into close contact with the photoresist surface. This process is capable of printing features in PMMA down to just below 1 μm dimensions. It was selected as the base polymer platform because it can be patterned with DUV light at reasonable doses without the need for chemical amplification which would introduce local pH variations which could potentially interfere with the ssDNA immobilized on its surfaces. It can also be copolymerized with a variety of organic monomer units which can be covalently bound to different ssDNA terminal groups. PMMA undergoes chain scission[50] of the polymer backbone, as shown in Figure 2.2, to yield smaller molecular weight (MW) polymer fragments that have higher solubility in developer than the coated polymer. The exposed, low-MW polymer fragments can then be dissolved away using an appropriate developer, leaving the mask pattern in the unexposed regions of the polymer.

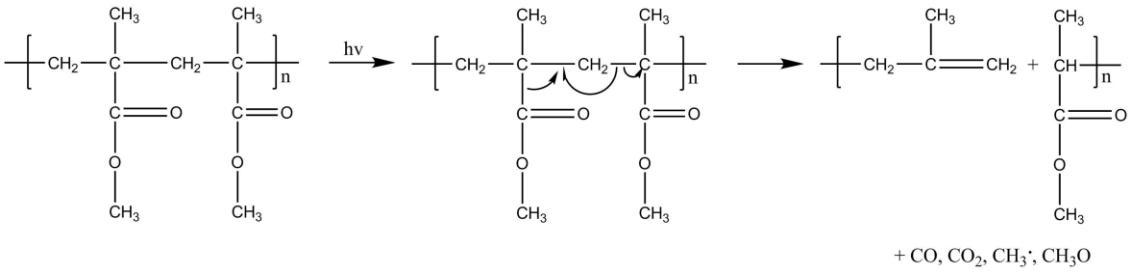

Figure 2.2: Description of the PMMA polymer backbone chain scission induced by irradiation with DUV light.

A chromium-on-quartz photomask was used for the DUV exposure of the copolymers. The mask layout was designed with computer aided design (CAD) software (L-edit) to generate several arrays of repeated two-dimensional chromium shapes for the 1 : 1 correspondence of mask pattern to photoresist pattern in a contact lithography system. The bright-field photomasks for this project were purchased from Photronics, Inc. and were written by an e-beam mask writer. Since the minimum resolution for this system is roughly 1 μm at one-to-one line-space pattern densities in the absence of resolution enhancement techniques, arrays of shapes were printed in sizes ranging from 1 μm to 100 μm to test the resolution of the system. These shapes included one-to-one gratings, squares, rectangles, circles, and longhorn shapes. In order to accommodate the double-exposure process outlined in Chapter 1, the mask layout was divided into quadrants and several superimposable line-space gratings were positioned in corresponding locations on the mask so that the patterns lined up perpendicularly after a 90° rotation of the mask. Each square-shaped feature array on the mask (excluding the dose-to clear macros) is laid out with respect to the true center origin of the physical mask such that they all line up no matter how the mask is turned. This allowed for an edge-of-the-mask based course alignment of the second grating exposure to the existing grating already printed on the wafer. This mask design is capable of printing squares and rectangles directly or from two exposures of perpendicular gratings in series without the use of an expensive mask aligner tool (Fig. 2.3), however, superimposable alignment marks were designed periodically on the mask for use with mask-to-substrate alignment.

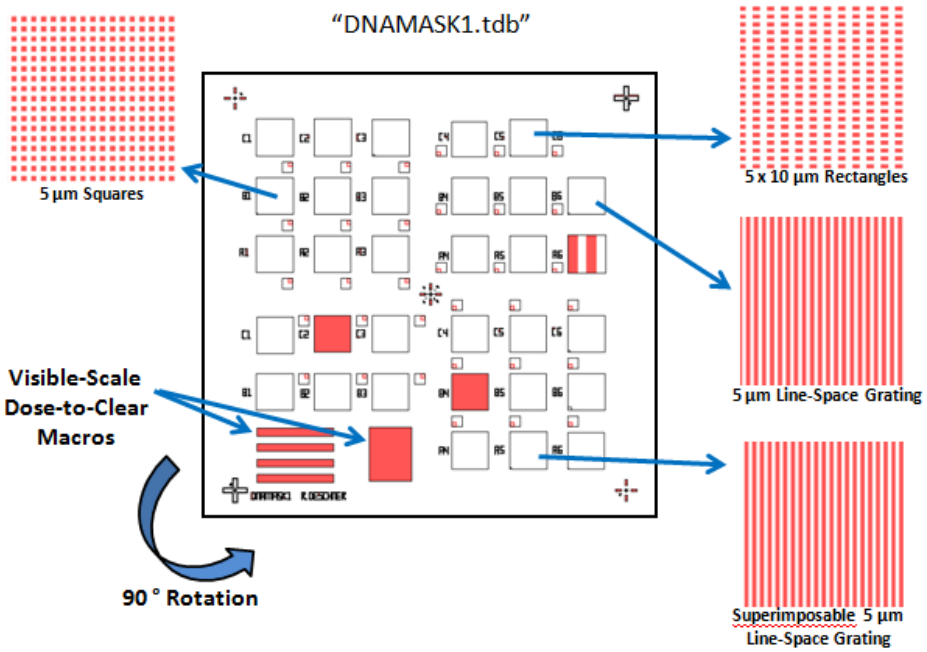

Figure 2.3: Layout of chromium-on-quartz photomask including example arrays for square, rectangular, and line-space grating features. The gratings are designed such that they can be perpendicularly superimposed over each other in a double-exposure process with a 90° turn of the mask.

A 500 W broadband mercury arc lamp (68810, Oriel Corporation) with a manual shutter switch (71445, Oriel Corporation) was used as the light source. The full exposure system, shown in Figure 2.4 used a 90° bend mirror to direct the light from the source to a custom-designed mask holder consisting of a custom-designed aluminum mask frame on a base with a micrometer to support the wafer and bring it into close contact with the mask. A water filter (Model 6127, Oriel Corporation) was also used to filter out infrared (IR) wavelengths generated by the source to avoid excessive heating of the silicon substrate. The entire setup shown was enclosed in an orange light box with high optical density (OD) walls to keep stray low-wavelength light from injuring students in the lab.

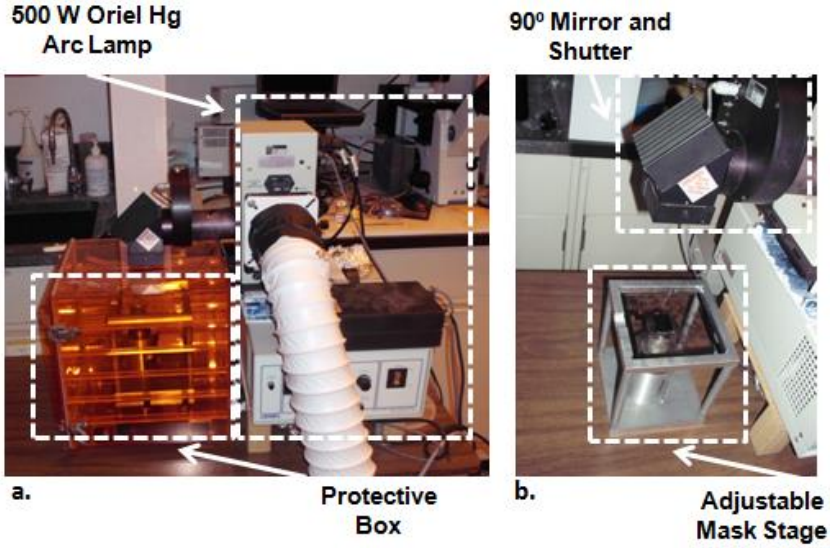

Figure 2.4. a. Photograph of original exposure system configuration showing the 500 W mercury arc lamp which directs light into a protective box, which houses b. the aluminum mask stage with an adjustable micrometer.

Unfortunately, the light intensity delivered to the photoresist in this configuration was not enough to fully expose the patterns into the photoresist at reasonable time scales (<30 mins). In addition, the spectral output of the IR water filter unit allowed only 60% transmittance of wavelengths below 350 nm. Thus, a new configuration was assembled in which mask was aligned to the vertical wall of the light box without the use of a 90° turn or IR water filter in order to minimize the distance from the light source to the substrate (Fig 2.5). This configuration was capable of delivering an intensity of 1.1 W/cm^2 as measured with an optical power meter, reducing the exposure times to on the order of 10 minutes. Even with these improvements, the required dose to print the mask patterns was roughly 50X more than that required for high-end projection lithography systems used in semiconductor manufacturing today. This is largely due to the fact that modern photoresists are chemically amplified, meaning they rely on photoacid or photobase-generating additives which catalyze the deprotection of pendant moieties on the polymer backbone making them more soluble in developer. We chose to avoid these

additives due to potential degradation of the functionalized ssDNA on the surface of the copolymer.

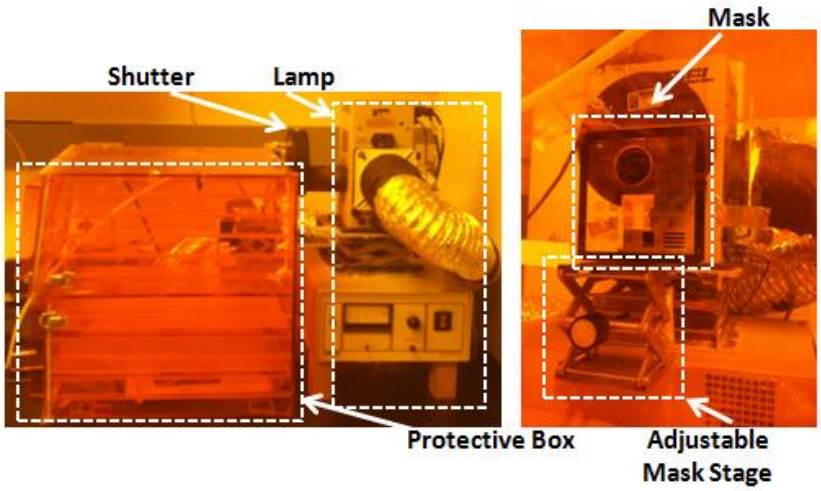

Figure 2.5. Photograph of the exposure system modified for minimized optical path length to the substrate.

Two other light sources were tested to pattern the PMMA copolymer: a 248 nm KrF excimer laser and a 193 nm ArF excimer laser. Unfortunately, the intensity output to the substrate was too weak to expose thick (>1 μm) PMMA films at exposure times of less than 1 hr. Additionally, it was found that film thicknesses greater than 2.5 μm were difficult to print with good fidelity using the mercury arc lamp, leaving significant footing in the resist profile even at much higher doses.

In addition to relatively long exposure times, heat generation from the broadband light reaching the substrate without the 90° bend module or the water filter was a problem. Raising the substrate temperature to levels above the T_g of the copolymer caused the material to flow and stick to the chromium mask features, requiring them to be regularly cleaned with solvents or piranha solution. To counter this, two types of cooling systems were devised to reduce the substrate temperature. For the first cooling device,

water tubing was run from a liquid circulator chilling unit (GP-100, Neslab) to a hollowed-out aluminum base with a thermocouple attachment. The chiller pumped a 50-50 mixture of ethylene glycol and water through the base which was attached to the back of the wafer to decrease the temperature and collect temperature data during exposure. This device was capable of reducing the substrate temperature by approximately 25 °C. An air-cooling system consisting of air tubing run from the laboratory air source with a valve was affixed to the interior of the light box and the air flow was directed toward the back of the wafer during exposure. This system was only able to decrease the substrate temperature by 10 °C during exposure. However, this proved to be adequate to maintain sub-T_g substrate temperatures for the copolymers used and was employed for the general operation of the exposure system.

To test the performance of the lithography system, 25,000 MW PMMA (Sigma Aldrich) was dissolved in PGMEA to yield a 10% w/w solution that was spin-coated (Headway Research spin coater) onto a silicon wafer at a thickness of 2.5 μm. Multiple coatings in series were necessary with 160 °C baking steps for 5 minutes after each coating to achieve a thickness of 2.5 μm at this concentration. A final 30 minute hard bake at 160 °C was performed in order to remove as much residual solvent as possible from the film. After baking, the wafer was brought into contact with the photomask, exposed, and developed for 2 minutes in a of 3 : 1 v/v solution of isopropyl alcohol (IPA) to methyl isobutyl ketone (MIBK). Images of the PMMA gratings in the resolution testing macro were taken on an optical microscope (BX60, Olympus) as shown in Figure 2.6. Based on these images, the process was capable of resolving 1 : 1 line-space gratings down to 2 μm. The 1 μm gratings printed very poorly and were presumably lifted-off by the developer process. The 2, 2.5 and 3 μm gratings printed well, though a

very small amount of residual PMMA was present between the lines, and the 5 µm grating printed extremely well, having clean-cut lines with little to no residual PMMA.

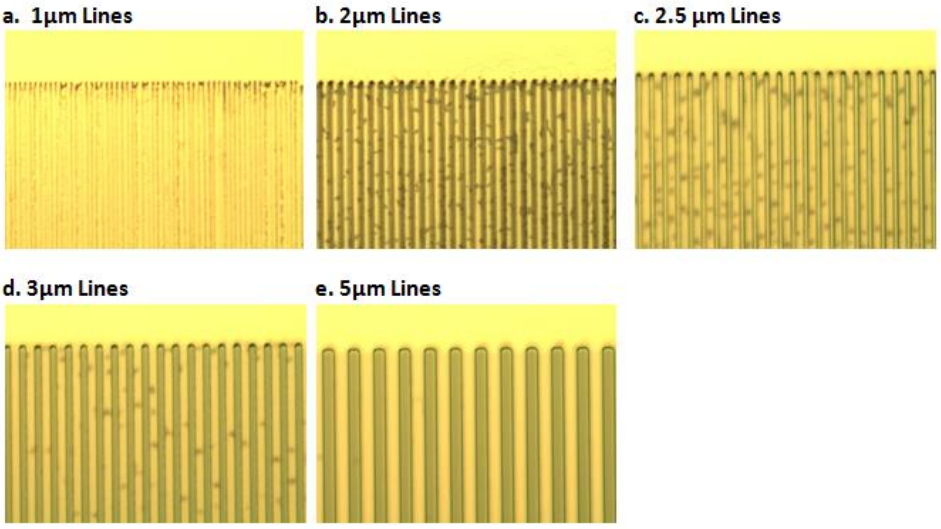

Figure 2.6. PMMA line-space gratings on bare silicon at a. 1 µm, b. 2 µm, c. 2.5 µm, d. 3 µm, and e. 5 µm line dimensions.

2.3 COPOLYMER PERFORMANCE AS PHOTORESISTS

A variety of reactive copolymers containing MMA and other monomer units with a reactive group for ssDNA conjugation were synthesized for photolithographic performance testing. The strategy was to use copolymerizations of MMA and another MMA-based unit containing a functional group capable of reacting with one of the many 5' or 3' terminus modifications available for synthetic ssDNA. Glycidyl methacrylate (GMA), N-hydroxysuccinimide methacrylate (NHSMA), pentafluorophenyl methacrylate (PFPMA), and methacrylic acid (MAA) were selected because the epoxy[51], NHS[52], PFP[53], and carboxylic acid groups can form amide bonds with terminal amines. In addition, maleimidoethylmethacrylate[54] (MEMA) and propargyl methacrylate[55] (PMA)

were selected for their reactivity with thiols and azide groups, respectively. The chemical structures for these copolymers are shown in Figure 2.7.

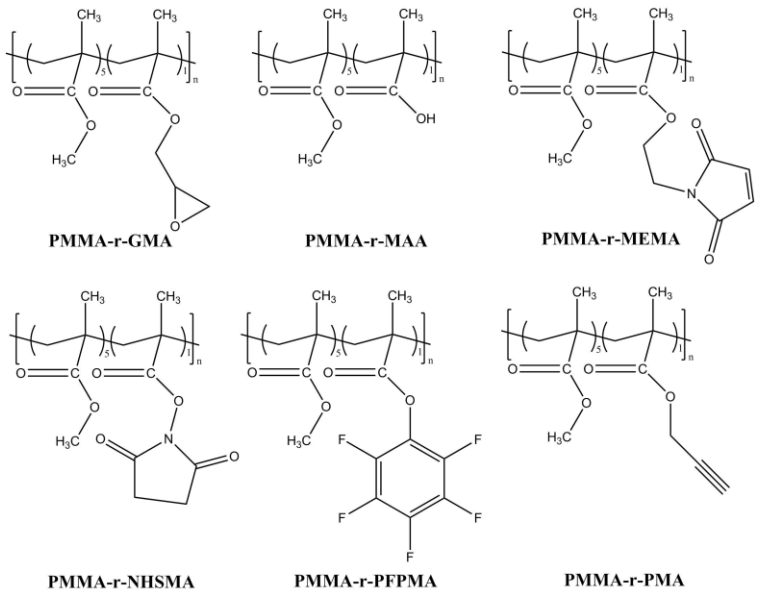

Figure 2.7: Chemical structures of the bioreactive acrylate-based copolymers.

In order for these materials to be used as photoresists, the exposed regions must be rendered soluble in developer whereas the unexposed regions must remain highly insoluble to the developer at reasonable time scales. Photoresists which have an unexposed developer rate of greater than a few nanometers per minute are not suitable for patterning because the pattern fidelity begins to significantly degrade. A developer study was performed in which unexposed films of each copolymer were coated onto silicon substrates and exposed to different compositions of developer. A 1 : 3 v/v mixture of MIBK in IPA[56] is a standard developer for PMMA commonly used in the microelectronics industry and typically has a an unexposed dissolution rate of less than 2 nm/min. Four dilutions of MIBK in IPA as well as neat IPA were used to develop each of the copolymer samples for 5 minutes. The film thickness reduction rates were

measured on a variable angle ellipsometer (M-2000V VASE, J. A. Woollam) after exposure to the developer as shown in Figure 2.8.

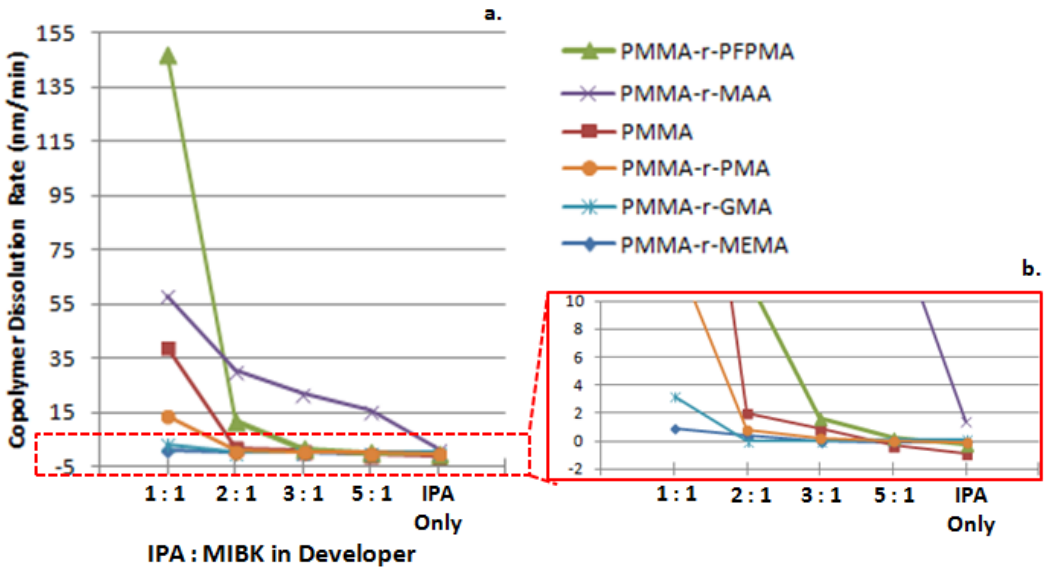

Figure 2.8 a. Unexposed dissolution rate for the reactive copolymers for developer solutions of decreasing MIBK concentration. b. (inset) Zoom-in of low dissolution rate area of plot.

MEMA, GMA, and PMA performed very well, having unexposed dissolution rates that were lower than PMMA for the 1 : 1, 2 : 1, and 3 : 1 IPA to MIBK mixtures, thus a 2 : 1 ratio was recommended to develop these materials. PFPMA had a dissolution rate curve that was slightly higher than that of PMMA, but it was still in the 2 nm/min regime; a 3 : 1 ratio of developer was recommended for these materials. MAA had a significantly elevated dissolution rate curve, and it was only in the 2 nm range in the neat IPA developer. Thus, it was recommended that MAA only be developed with an IPA solution. A 3 : 1 ratio of IPA : ethyl acetate was found to be a good developer for the PMMA-r-NHSMA material and exhibited an unexposed developer rate of less than 2 nm.

A primary metric used to quantify the performance of photoresists is contrast. Theoretical photoresist contrast is defined[57] as:

$$\gamma = \frac{1}{log_{10}\frac{E_{100}}{E_0}} \tag{2.2}$$

where γ is the photoresist contrast, E_{100} is the dose required to begin development of the photoresist, and E_0 is the dose required to completely develop away the exposed photoresist. On a contrast curve which plots percent thickness remaining versus exposure dose on a semi-log plot, the contrast is the slope of the linear portion of the curve. Photoresists with higher contrast result in more vertical resist profiles and thus better feature resolution.

The contrast performance of these materials as photoresists was tested by coating films of each copolymer onto a silicon substrate at a thickness of 2.5 μm and performing a series of exposures at increasing dose to establish a contrast curve plot of film thickness decrease versus exposure dose. Each wafer was baked at 160 °C for 5 minutes after each coating step, followed by a 30 minute bake at 160 °C. The contrast curves for the reactive copolymers produced are plotted in Figure 2.9.

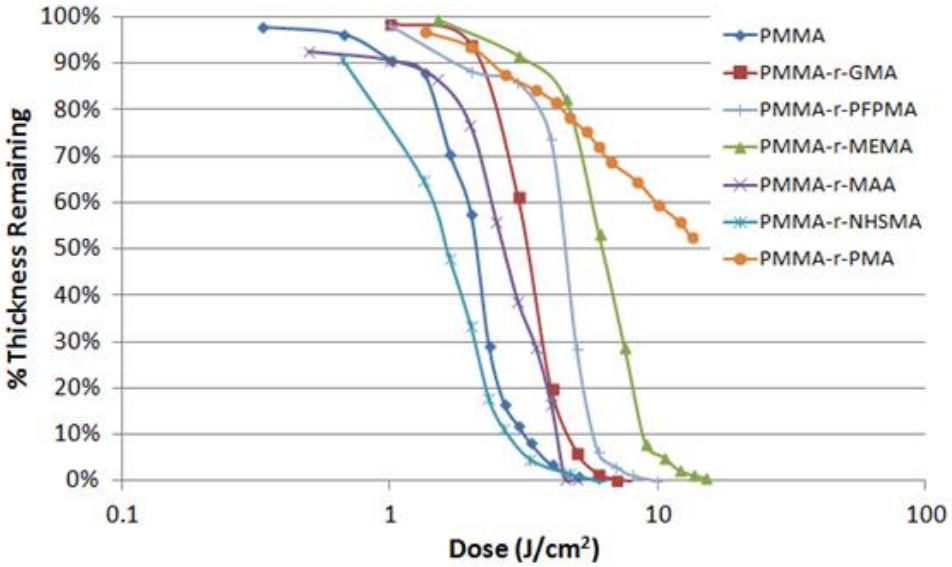

Figure 2.9. Semi-log plot of contrast curves for the copolymers auditioned as photoresists.

Because these copolymers deviate from an ideal photoresist profile, i.e. the majority of the curve is non-linear, especially in the thickness ranges near E_{100} and E_0, E_{95} and E_5 values were used to estimate contrast values for each copolymer for comparison. The contrast values for the copolymers are listed in Table 2.1. GMA, PFPMA, and MEMA had the highest contrast values and were considered to be the best copolymer candidates in terms of performance as photoresists. MAA and NHSMA had lower contrast values but were still considered to be acceptable, and PMA was deemed to be unsuitable as a photoresist.

Polymer	E_0 (J/cm^2)	γ
PMMA	9.0	1.4
PMMA-r-GMA	7.5	2.2
PMMA-r-PFPMA	11.0	1.5
PMMA-r-MEMA	16.0	1.5
PMMA-r-MAA	5.5	1.2
PMMA-r-NHSMA	7.2	1.0
PMMA-r-PMA	>25.0	<<1

Table 2.1: Dose-to-clear and contrast values for the reactive copolymers auditioned.

Included in the table is a list of the photospeed (E_0) values for each polymer. Photospeed is a measure of the quantum efficiency of the resist which is a ratio of the number of photoevents in the resist and the incident photon flux density, commonly characterized by the required dose to completely remove the photoresist from the exposed areas, or, dose-to-clear. The photospeeds of the MEMA and PMA copolymers were significantly larger than the other materials, with the PMA photospeed being so high (>20 J/cm^2) that it was considered unusable with its excessive required exposure time (>1 hr). The recommended exposure conditions for each copolymer are listed in Table 2.2.

Material	Developer	Estimated Dose (J/cm^2)	Bake Condition
PMMA	3 : 1 (IPA : MIBK)	9.0	160 °C / 5 min
PMMA-r-GMA	2 : 1 (IPA : MIBK)	7.5	160 °C / 5 min
PMMA-r-PFPMA	3 : 1 (IPA : MIBK)	6.4	160 °C / 5 min
PMMA-r-MEMA	2 : 1 (IPA : MIBK)	16.0	160 °C / 5 min
PMMA-r-MAA	IPA only	5.5	160 °C / 5 min
PMMA-r-NHSMA	3 : 1 (IPA : Ethyl Acetate)	7.2	160 °C / 5 min
PMMA-r-PMA	2 : 1 (IPA : MIBK)	Unacceptable	160 °C / 5 min

Table 2.2: Recommended processing conditions for each copolymer.

The PMMA-PFPMA copolymer performed well both as a photoresist and a reactive surface for ssDNA conjugation as described in Chapter 3. A 2.5 μm thick film

of this material was used to print several arrays of shapes down to 2.5 µm dimensions to demonstrate the capability of the patterning process on a lift-off layer. Figure 2.10 is a collection of optical microscope images taken of 2.5 µm squares, 5 µm squares, 10 µm squares, 5 x 10 µm rectangles, 5 x 10 µm rectangles printed using a double-exposure scheme, and 10 x 20 µm rectangles.

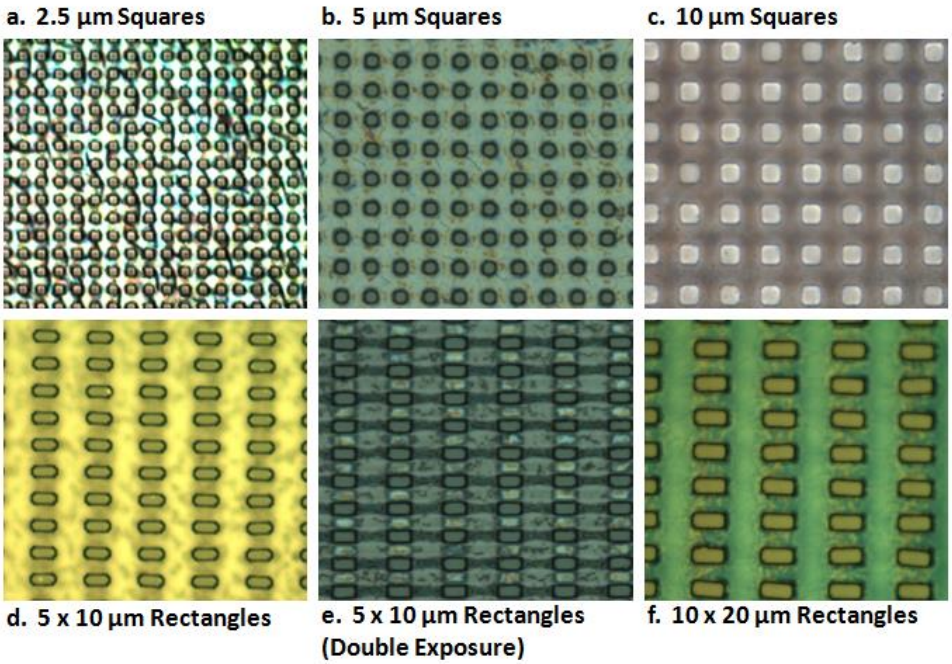

Figure 2.10. Optical microscrope images of 2.5 µm thick PMMA-PFPA on a 200 nm poly(methyl glutarimide) lift-off layer patterned into a. 2.5 µm squares, b. 5 µm squares, c. 10 µm squares, d. 5 x 10 µm rectangles, e. 5 x 10 µm rectangles (5 µm grating + 10 µm grating), and f. 10 x 20 µm rectangles.

This process was capable of printing on the order of 10^5 – 10^7 features for each exposure depending on the size of the shapes. The resolution of the patterns was considered to be acceptable down to 2.5 µm squares. Serendipitously, the 5 µm/10 µm double exposure rectangles (Fig. 2.10e) actually printed with sharper edges and corners than the 5 x 10 µm single exposure rectangles. This is due to the fact that resolving sharp

corners is very challenging for a single exposure process, but well-defined long line edges are not.

Some non-uniformity of the feature shapes was present. This was most likely caused by the fact that the contact printing process never comes uniformly into contact with the entire surface of the copolymer during exposure, especially if foreign material or defects are present on the mask. These defects tend to increase with each successive printing unless they are removed from the surface of the mask by solvent or Piranha etc. In addition, the beam had a radial intensity gradient which caused features at the center of the exposure area to receive higher doses, leading to smaller printed dimensions, than those at the edge.

Chapter 3: ssDNA Immobilization of Dual-functional Materials

3.1 Introduction to Single-Stranded DNA

Deoxyribonucleic acid, or DNA, is the characteristic design source from which all living things are created. It contains, within its sequence of nucleobase building blocks crammed into tiny packaging, the entire code for the construction of unique complex organisms from nanometer-scale bacteria to meter-scale blue whales. It accomplishes the construction of these organisms through activities such as copying itself, translating itself into larger building blocks, and folding itself into very compact and complex configurations which are all carried at the nanometer scale. These activities can be thought of as the holy grail of bottom-up self assembly-based construction. It is for these reasons that DNA has been targeted by researchers for the nanoscale self assembly of nanoscale building blocks with the goal of developing a process for constructing any complex shape desired in large quantities.

Single-stranded DNA (ssDNA) is essentially a biopolymer consisting of a backbone of phosphate groups and sugars called deoxyribose. This backbone supports a heterogeneous combination of nucleobases: adenine, thymine, guanine, and cytosine. Nucleotides, or nucleobase units coupled with deoxyribose and phosphate groups, are combined like monomers in very long strings (measured in kilonucleotides) generating vast numbers of permutations which form a biological code containing information on the order of megabytes. ssDNA is usually found in very stable duplex structures called double helices, wherein they are paired with other ssDNA in a twisting configuration held together by hydrogen bonding called Watson-Crick base pairing as shown in Figure 3.1. This binding scheme consists of adenine binding with thymine and cytosine binding with

guanine. This aggregate hydrogen bonding, known as strand hybridization, is the associative mechanism sought after by researchers for controlling the self assembly of larger media.

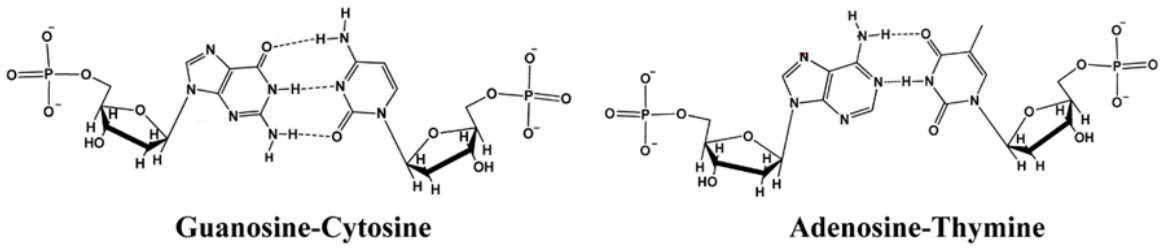

Figure 3.1. Watson-Crick base pairing exhibited in double-stranded DNA. *Reprinted with permission from* [58]

In order to make use of this mechanism, single stranded forms of DNA with known compositions must be isolated. In the 1970's, the development of phosphoramidite synthesis made the production of synthetic ssDNA sequences a reality. This chemistry led to modern technology capable of producing highly accurate and reproducible ssDNA strands in quantitative yields. Today, several companies produce custom DNA oligomers in sequence lengths up to hundreds of nucleotides which can be modified with an array of functional groups like amines or thiols for further conjugation, markers such as fluorescent dyes, or spacers such as alkanes or poly(ethylene glycol) units.

3.2 DNA CONJUGATION CHEMISTRIES FOR THE BIOREACTIVE ACRYLATE-BASED COPOLYMERS

Custom-designed synthetic ssDNA is essential to forming functionalized polymer particles which can be selectively coupled together according to their DNA labeling. To accomplish this, six different potential reactive copolymer structures were explored for the covalent immobilization of ssDNA with various terminal modifications. Glycidyl Methacrylate (GMA), pentafluorophenyl methacrylate (PFPMA) and N-hydroxysuccinimide methacrylate (NHSMA) groups were selected to react directly with ssDNA-bearing terminal amine groups to form covalent amide bonds. Methacrylic acid (MAA) was chosen to react with amine-terminated ssDNA sequences via carbodiimide chemistry to form an amide bond. Maleimidoethylmethacrylate (MEMA) forms a carbon-sulfur bond with thiol-terminated ssDNA sequences. Also, propargyl methacrylate (PMA) was selected for its reaction with azide-terminated ssDNA sequences in the presence of a copper(I) catalyst. The reactions schemes for the covalent binding of ssDNA to the copolymers are shown in Figure 3.2.

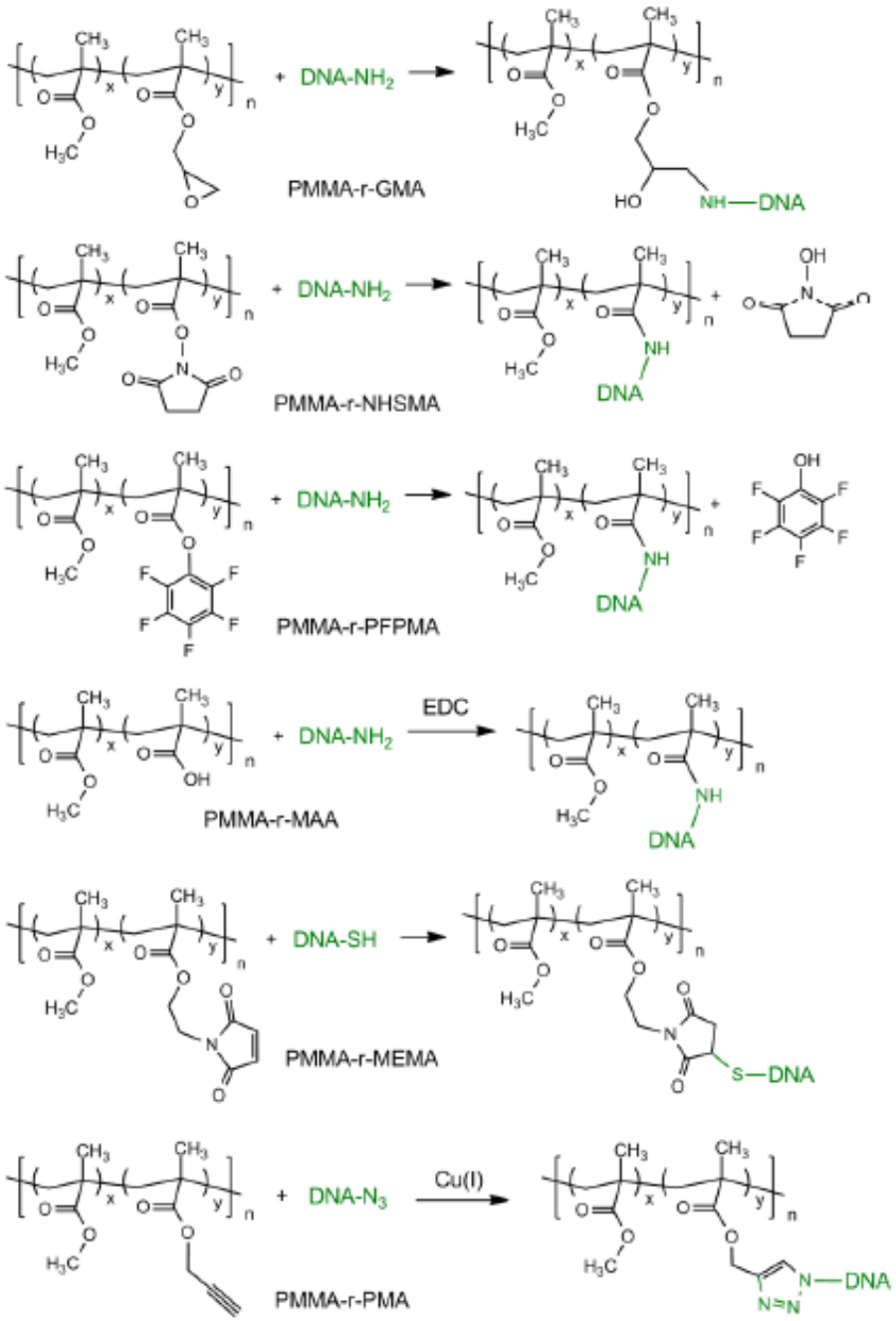

Figure 3.2. Reaction schemes for the formation of covalent bonds with different terminal ssDNA modifications.

3.3 FLUORESCENT DETECTION OF ssDNA IMMOBILIZATION

Once ssDNA has been successfully conjugated to the surface of a bulk material, the effectiveness of the surface functionalization must be characterized. This can be done by employing ssDNA with terminal fluorophore groups, whose presence can be detected with a fluorometer which consists of a laser light source which emits light at a specific wavelength to excite the fluorophores, causing them to emit light at in a known wavelength range. This emitted light is detected by a transducer which converts it into an electronic signal which is translated into a fluorescence intensity reading proportional to the number of fluorophores present on the surface of the material. Fluorophores are molecules which release energy in the form of light when excited to higher energy states by incident light at a specified wavelength. This emission of light occurs at specific wavelength range which is characteristic of the fluorophore. Accordingly, combinations of different fluorophores which emit light at significantly different wavelengths can also be used to distinguish between different ssDNA functionalizations. In order to accomplish this, fluorophores with different emission wavelength ranges must be paired with light sensors which only detect.

In order to estimate the ssDNA density present on the surface of the reactive copolymer films, a calibration control experiment was performed in which 10 μL spots of known concentrations of fluorophore-tagged ssDNA (terminated with either Cy3 or HEX fluorophores) were dispensed onto a 300 nm film of PMMA coated onto a glass slide and allowed to dry in ambient conditions for three hours. The spots were read on a fluorescence scanner tool commonly used for microarrays (GenePix 4000B, Molecular Devices). This tool was equipped with two different lasers with wavelengths of 532 nm and 635 nm and fluorescent sensors designed to collect fluorescent emission at 557 - 592 nm and 650-690 nm, respectively. The fluorescence signal detected using the 532 nm

laser at PMT (photomultiplier tube) gains of 400, 500, and 600 was plotted against the known concentrations of the spots for each fluorophore as shown in Figure 3.3. Both plots contain calibration curves which are almost linear and can be used to roughly estimate the amount of ssDNA immobilization from fluorescence signal.

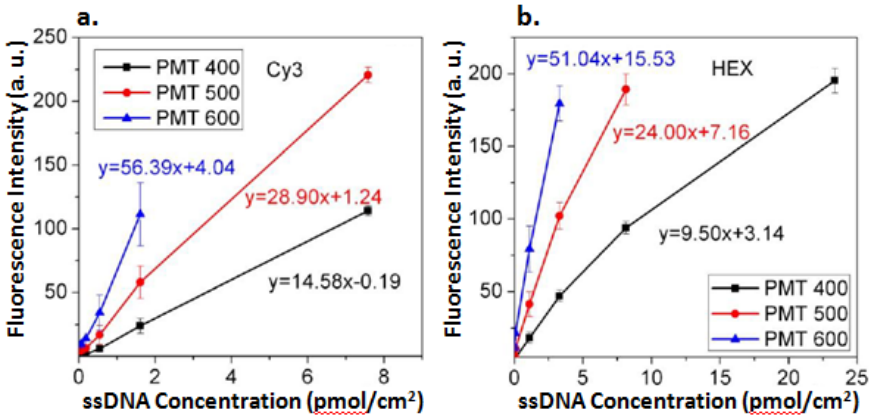

Figure 3.3. Fluorescence intensity versus DNA density calibration curves at gains of 400, 500, and 600 for a. Cy3 and b. HEX fluorophores. *Courtesy of Dr. Hao Tang.*

3.4 AMINE CONJUGATION CHEMISTRIES

Three of the materials developed for the surface immobilization of ssDNA were designed to react with strands modified with an aliphatic amine and the 3' or 5' terminus. They react to form covalent amide bonds at basic conditions under conditions. This type of chemistry was selected because it is a one-step process involving reaction conditions that are mild enough to not damage the oligonucleotide sequence of the DNA strands.

To test the ssDNA surface functionalization of these materials after reaction, films of each material were coated onto glass microscope slides using a spin-coater at a nominal thickness target of 300 nm. The slides were first cleaned with a piranha solution consisting of a 5 : 1 ratio of sulfuric acid to hydrogen peroxide. It is important to note

that piranha solutions can be very dangerous and proper safety precautions must be taken when using them. Proper face shielding, a heavy duty protective apron, and gloves were worn at all times during the preparation and utilization of the piranha solution. In addition, concentration sulfuric acid should never be poured into hydrogen peroxide. After cleaning a 30 nm film of AP-410 adhesion promoter was coated onto the slide and baked for 5 minutes at 160 °C, followed by spin-coating of the reactive copolymer and an additional 30 minute 160 °C bake to remove any residual solvent in the film. Solutions of 10 μM amine-terminated ssDNA tagged with Cy3 fluorophores in 100 mM carbonate or phosphate buffer solutions ranging from pH 7 to pH 11 containing 2 mM ethylenediaminetetraacetic acid (EDTA) were dispensed onto the surfaces of the films and allowed to react in a vapor chamber for 16 hours. The vapor chambers consisted of a plastic petri dish with approximately 2 mL of water droplets scattered around the area where the microscope slide was positioned.

After 16 hours, the slides were carefully immersed in 1x saline-sodium phosphate-EDTA (SSPE) with 0.1 wt% Tween20 surfactant twice, followed by three 0.1x SSPE-only rinses. Each rinse step was accompanied by a 5 minute rotation at 60 RPM on a shaker table. After rinsing, the slides were dried with a nitrogen gun and then analyzed on a fluorescence scanner. Fluorescence intensity data using the 532 nm laser was correlated to ssDNA concentration using the calibration curves to yield a plot of ssDNA concentration to pH as shown in Figure 3.4. From this plot it is evident that the PFPMA copolymer had a significantly higher signal than the other two copolymers. Furthermore, the higher pH conditions yielded improved ssDNA, with a pH of 11 having the best performance.

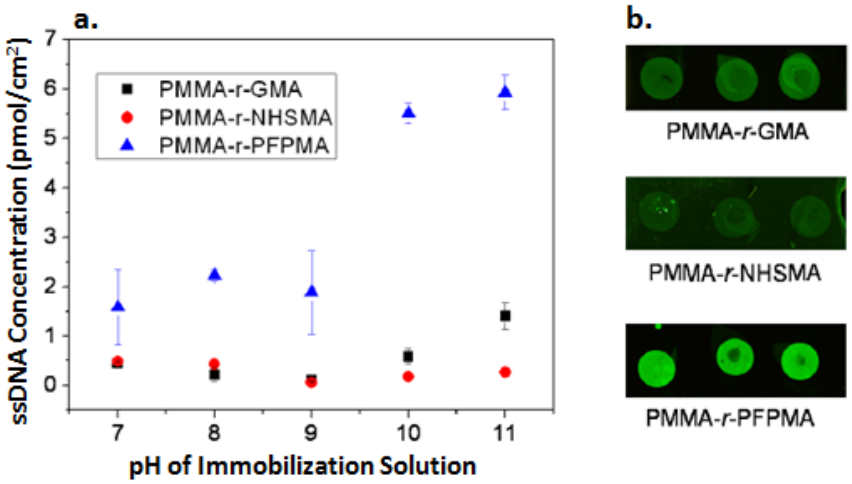

Figure 3.4. a. pH-dependent surface immobilization of fluorescent ssDNA and b. sample images taken on fluorescence scanner. *Courtesy of Dr. Hao Tang.*

Another study was performed to analyze the pH dependence of the surface functionalization reaction with the PFPMA copolymer in more depth. For this experiment, ssDNA immobilization solutions with pH values from 7 to 13 were prepared similar to the previous experiment with carbonate or phosphate buffers and 10 µM Cy3-tagged aminated ssDNA. The results, shown in Figure 3.5 depict a parabolic response in ssDNA surface density to reaction pH, with a maximum value at a pH of 10.5. This pH was selected for subsequent PFPMA reaction conditions. Higher pH conditions than pH 11 were not used for subsequent immobilizations reactions with the PFPMA copolymer to ensure that no degradation to the ssDNA occurred.

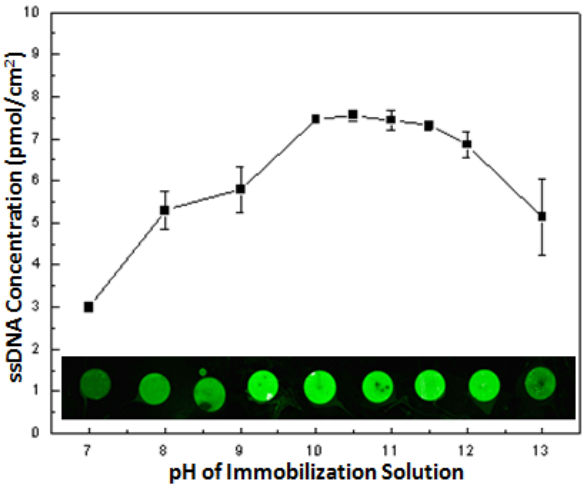

Figure 3.5. a. pH-dependent surface immobilization of fluorescent ssDNA on PMMA-r-PFPMA and b. sample images taken on fluorescence scanner. *Courtesy of Dr. Hao Tang.*

3.5 THIOL CONJUGATION CHEMISTRY

The MEMA copolymer was tested for ssDNA immobilization performance in a similar manner. The maleimide group of the copolymer reacts with thiol-terminated ssDNA to form a thioether bond. Disulfide-terminated ssDNA is commercially available, but before it can be conjugated to the MEMA copolymer, it must be reduced with tris(2-carboxyethyl phosphine) (TCEP)[59]. This reaction was carried out in a one-step process in an immobilization solution consisting of 5x saline-sodium citrate buffer (SSC), 100 µM TCEP, and 10 µM disulfide-terminated ssDNA tagged with a Cy3 fluorophore. Five different reaction solutions were prepared with pH values ranging from 6 to 8, and 10 µL of each solution was spotted onto the surface of 300 nm-thick films of PMMA-r-MEMA. After a 16 hour reaction in a vapor chamber, the films were rinsed with the SSPE/Tween20 rinsing protocol and dried with a nitrogen gun. Fluorescence scanner analysis of these slides yielded the ssDNA density plot in Figure 3.6. The pH 7 reaction

condition was selected as the standard and was used for subsequent ssDNA immobilizations of the MEMA-based material.

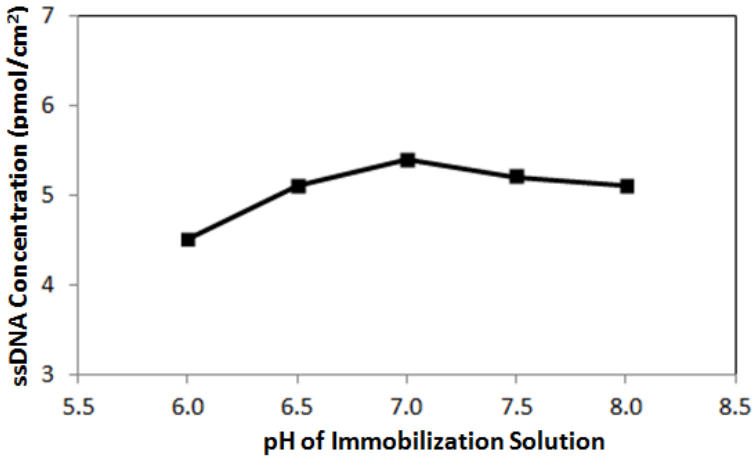

Figure 3.6. a. pH-dependent surface immobilization of fluorescent ssDNA on PMMA-r-MEMA.

3.4 CARBODIIMIDE-MEDIATED AMINE CONJUGATION CHEMISTRIES

The PMMA-r-MAA reactive copolymer was designed with a carboxylic acid group for amide bond formation[60] with amine-terminated ssDNA. This chemistry was inspired by classical peptide bond chemistry which can be carried out using a carbodiimide which forms an O-acylisourea intermediate with a carboxyl group[61]. This intermediate readily reacts with terminal amines to form an amide bond with a urea as a by-product as shown in Figure 3.7. Many carbodiimides are used for covalent immobilization of ssDNA onto carboxyl-functionalized substrates or resins such as N,N'-dicyclohexylcarbodiimide (DCC), N,N'-diisopropylcarbodiimide (DIC), and 1-ethyl-3-(3-dimethylaminopropyl)carbodiimide (EDC). EDC was chosen for this application since it is reasonably water-soluble, unlike the other commonly-used carbodiimides, and compatible with ssDNA preservation.

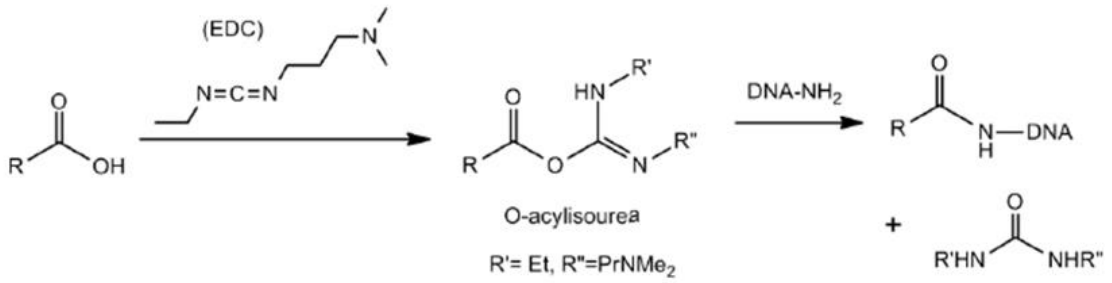

Figure 3.7. Reaction scheme for carboxyl groups on the PMMA-MAA copolymer with amine-terminated ssDNA using carbodiimide chemistry.

To test the performance of the carbodiimide-mediated PMMA-r-MAA reaction, six different immobilization solutions were prepared with 10 μM amine-terminal ssDNA tagged with Cy3, 100 mM 2-(N-morpholino)ethanesulfonic acid (MES), and a range of EDC concentrations from 2 to 100 mM. Figure 3.8 is a plot of the ssDNA density on the surface 10 μL spots of each solution reacted with a PMMA-MAA film for 16 hours. The fluorescence signal increases almost linearly to an EDC concentration of 20 mM, then levels off at higher concentrations.

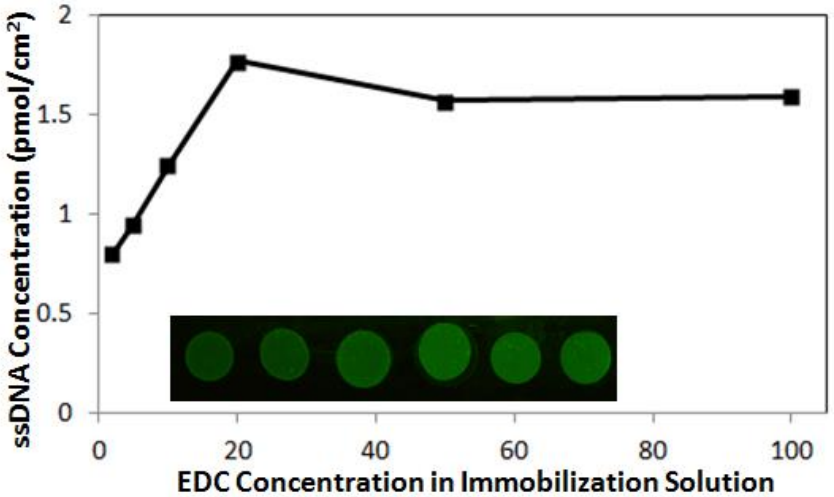

Figure 3.8. Response of PMMA-r-MAA ssDNA (Cy3 tagged) density to increasing concentrations of EDC in the immobilization solution.

3.5 CONCLUSIONS

The fluorescence scanner served as an effective tool for the surface density analysis of fluorophore-tagged ssDNA on the selected copolymer materials. The PFPMA copolymer had the highest ssDNA mobilization density out of the amine-reactive copolymers studied, including PMMA-r-GMA and PMMA-r-NHSMA. Because this material exhibited very good ssDNA immobilization as well as above average patterning capability, it was selected for further performance analysis in subsequent steps in the process flow. The maleimide-containing polymer also displayed very good patterning and ssDNA immobilization properties and was selected for further analysis. The MAA-containing material which used carbodiimide chemistry for ssDNA conjugation had modest immobilization results and fair patterning results. However, it was excluded from further performance testing because the PMMA-MAA copolymer turned out to be somewhat soluble in water. Water-soluble materials are not acceptable for this application because the ssDNA surface functionalization will not live through processing steps which involve long-term exposure to aqueous solutions. Finally, the propargyl methacrylate material was not retained for ssDNA immobilization analysis or further performance testing because of its inordinately high dose-to-clear requirement.

It is important to note that the fluorescence data resulting from the ssDNA surface density experiments on bulk films were helpful in selecting the reaction conditions for each platform, but repeatability of these experiments was not very good. The fluorescence signals were highly dependent on the execution of the rinsing conditions and were used primarily as a qualitative tool for comparing different reaction conditions on the same slide. Figure 3.9 is an example of an immobilization experiment wherein fluorescent, aminated ssDNA was immobilized onto the surface of a PMMA-PFPMA film for 16 hours followed by the standard SSPE/Tween20 rinsing process.

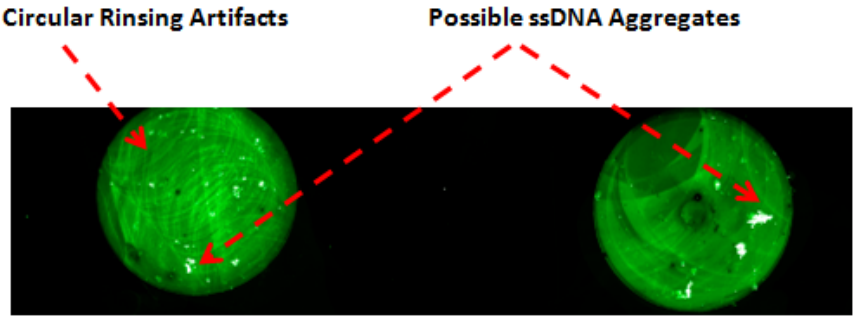

Figure 3.9. Circular rinsing artifacts and possible ssDNA aggregates observed on zoomed-in fluoresecent images of the ssDNA spots on a PMMA-r-PFPMA film.

Overlapping rings of high-intensity fluorescent DNA are seen in the zoomed-in fluorescent image on the left. These rings were most likely caused by the circular agitation associated with the shaker table during the 60 RPM rinsing step. These rings are less pronounced in the image on the right, but they can still be seen. In addition ssDNA aggregation occurred as exhibited by the white-colored bright regions on the spots. These aggregates tended to artificially increase the fluorescent signals for each spot, introducing unwanted variability.

Chapter 4: Sacrificial lift-off layer

4.1 INTRODUCTION

The development of a sacrificial layer capable of withstanding multiple wet and dry processing steps involving high temperatures and exposure to both organic and aqueous solvents was crucial to the development of patternable DNA-functionalizaed particles. The lift-off process essentially bridges the top-down patterning process with the three-dimensional self assembly process which must be carried out in solution. It must be able to withstand several harsh processing steps without appreciable phase change or dissolution, however, it must also be easily removed on demand at conditions which do not damage the reactive copolymer or the ssDNA functionalized on its surface.

4.2 MATERIALS

Several materials were identified to function as the lift-off layer (LOL) for this process flow. The initial requirements were that they could not dissolve in the casting solvent of the copolymers deposited on top of them (usually propylene glycol monomethyl ether[62] (PGMEA)) and that they could not be soluble in the photoresist developer, a 2 : 1 volumetric ratio of isoproplyl alcohol to methyl isobutyl ketone. Poly(octadecyl mthacrylate) (PODMA) was first targeted for this application because it was not soluble in the developer or PGMEA. However, this material turned out to have a very low glass transition temperature (-100 °C) and melting point (38 °C) rendering it incompatible with the up to 160 °C bake temperatures used to rid the copolymer of residual solvent after spin-coating. Poly(acrylic acid) (PAA) and poly(methyl glutarimide) (PMGI) were also identified as potential LOL materials because they met

both of the developer and casting solvent requirements, and they were thermally stable at least up to 125 °C.

PAA is a water-soluble acrylate-based polymer[63] that was selected because it is insoluble in the organic solvents used in fabrication of patterned copolymer microparticles, but readily soluble in aqueous solutions. It is commonly used in applications which require materials with high water absorption such as hydrogels[64,65] and materials used in diapers.

PMGI is a polymer commonly used in the semiconductor industry as an undercut layer employed to partially dissolve in strong base developers such as tetramethyl ammonium hydroxide[66,67]. For this application it is employed as the bottom layer in a bilayer stack with PMMA such that during development of the primary photoresist it begins to dissolve at a quicker rate, leaving a hanging cliff-like structure which can be further processed with sputter coating to generate thin metallic wires.

4.3 MATERIALS PERFORMANCE TESTING

To test the patterning capability of PAA and PMGI, 300 nm films of each material were coated onto a wafer with a spin-coater and baked at 120 °C. A thicker film (2.5 μm) of copolymer was coated on top of these materials followed by a 160 °C bake for 30 minutes. Despite the low T_g of the PAA film, both of these film stacks printed well as an underlayer and survived 2 minutes of development in the IPA/MIBK developer as shown in Figure 4.1. Figure 4.1a shows well-printed 5 μm PMMA-PFPMA squares on a PMGI LOL and Figure 4.1b and 4.1c show 5 x 10 μm PMMA-PFPMA squares on a PAA LOL. In Figure 4.1b some movement of the particles has taken place, presumably due to absorption or dissolution by the developer. However, these particles

remained on the substrate, even after rigorous air-drying with a nitrogen gun. In Figure 4.1c, strange worm-like structures in the background of the particles are visible. These structures seemed to dissolve later during the lift-off process and did not contaminate the particle solutions. In addition, these structures served as a sort of visual detection device which helped determine the end point of the exposure process.

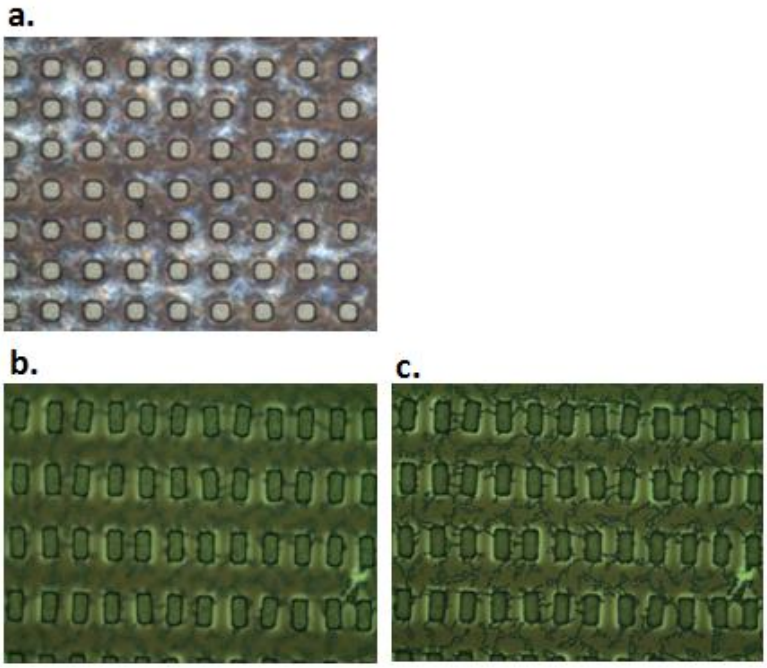

Figure 4.1. Post-develop optical microscope images of a. 5 x 5 µm squares on PAA and b., c. optical images at two different focus settings of 5 x 10 µm rectangles on PMGI patterned using PMMA-PFPMA copolymer.

The lift-off step for the PAA LOL was carried out in DI water, and usually the particles lifted off of the surface in less than 5 minutes. The PMGI LOL took slightly less than 5 minutes for lift-off in a 4 : 1 dilution of potassium borates in water (400k developer, Clariant). Unfortunately, the PAA LOL was not able to withstand the aqueous buffer conditions of the ssDNA functionalization process, and only parallelepipeds with six sides functionalized with the same sequence could be generated. This was useful

initially for initial analysis of the lifted-off particles, but this LOL could not be used for a process involving multiple ssDNA functionalizations. The PMGI LOL was printed into several shapes down to 2.5 x 2.5 x 2.5 μm cubes and was able to withstand multiple 24-hour in situ ssDNA functionalizations ranging from pH 4 MES buffer to pH 11 carbonate buffer, as well as multiple Tween20 surfactant treatments (used for the ssDNA blocking process). This led to PMGI being the LOL of choice for this process.

An undesirable complication was encountered during the lift-off of some arrays of printed features using PMGI. From time to time the PMGI lift-off layer would crack in multiple places during basic dissolution and these cracked macro-regions would remain insoluble in the solution, even after hours in the basic stripping solution. It was found that the edges of the array were susceptible to underexposure due to the radial decrease in intensity of the light source. During lift-off, these portions of the arrays still contained residual incompletely-exposed portions of PMMA-PFPMA and remained intact as thin sheets dotted with arrays of patterned shapes as shown in Figure 4.2. Eventually it was understood that underexposure was the underlying cause of this defect, and future printed arrays were trimmed at the edges with a razor blade to remove any potentially underexposed copolymer from the array. This technique worked quite well and this problem was no longer encountered.

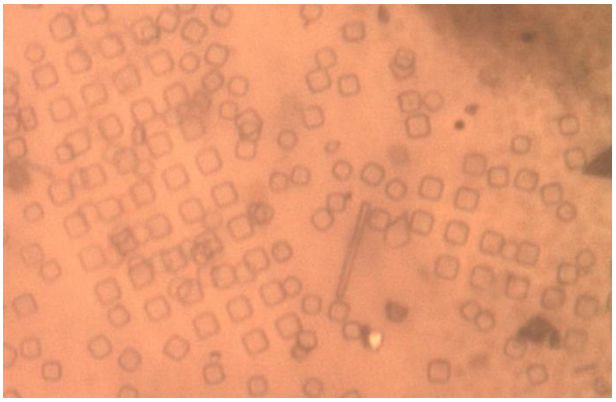

Figure 4.2. Optical microscope image of intact arrays of PMMA-PFPMA squares due to underexposure at the edges of the pattern array.

The PMGI lift-off layer was also compatible with a double exposure process in which line-space gratings were printed followed by a 90°-turned printing of another grating after development. This methodology actually yielded better-defined particle shapes because the corners no longer needed to be resolved in one exposure step. Figure 4.3a and 4.3b are examples of the PMMA-PFPMA copolymer printed as 5 µm line-space patterns and double-exposed 5 x 10 µm rectangles. These particles printed well and were readily lifted off into solution as shown in Figure 4.3c.

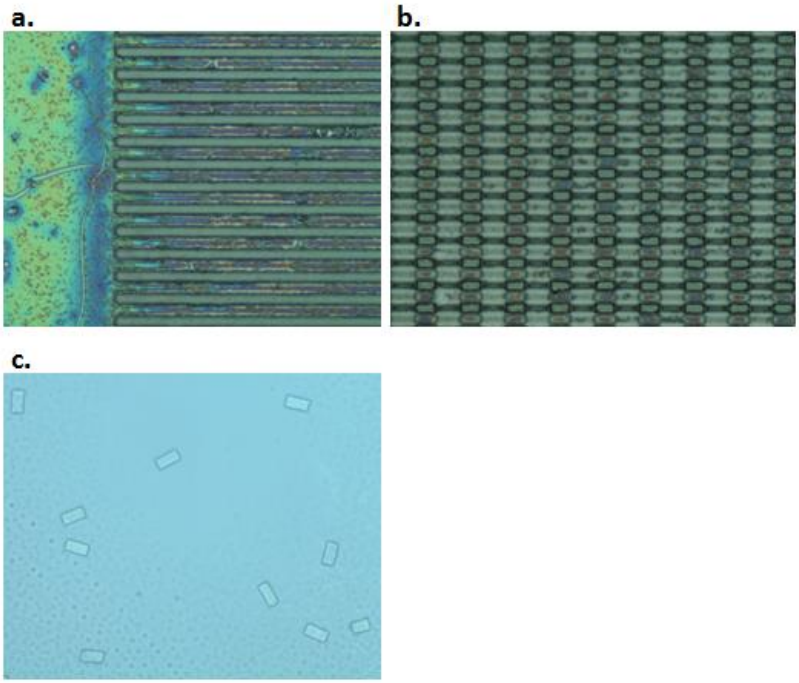

Figure 4.3. Optical microscope images of 5 µm line-space patterns and b. 5 x 10 µm rectangles printed on PMGI. c. Optical image of 5 x 10 µm rectangles lifted off of PMGI into solution.

4.4 CONCLUSIONS

The particle lift-off process is a step which is critical to the production of polyfaceted ssDNA-functionalized particles. Two primary LOL candidates were tested for their printing and functionalization processing compatibility by subjecting them to the harsh conditions of each step. PAA performed well through the printing process, but was incompatible with the aqueous immobilization buffers used in the ssDNA functionalization process. PMGI printed very well using both single and double-exposure patterning techniques yielding well-defined particles in solution.

This LOL material was also the only that was able to withstand all of the prolonged wet and dry processing steps required for the particle fabrication process flow. Finally, this material was readily dissolved in less than 5 minutes making it the only candidate suitable for this application.

Chapter 5: ssDNA EDC Coupling Reaction Optimization

Reprinted in part with permission from Deschner, R.; Tang, H.; Allen, P.; Hall, C.; Hlis, R.; Ellington, A.; and Willson, C. G., Chem. of Mat. (submitted November 3rd, 2013), Copyright the American Chemical Society.

5.1 INTRODUCTION

The carbodiimide-mediated reaction auditioned for the methacrylic acid-containing copolymer resulted in low ssDNA immobilization densities, prompting abandonment of further processing analysis of this material. However, when used with a hydrolyzed version of the PMMA-PFPMA copolymer, this chemistry led to very high levels of ssDNA surface functionalization. Hydrolysis of the pentafluoro ester of the copolymer results in the formation of a carboxyl group similar to that of PMAA. However, the PFPMA copolymer does not suffer from solubility issues in aqueous solutions and has patterning characteristics reasonable similar to a PMMA homopolymer. This conjugation chemistry was preferred over those of all of the other reactive copolymer materials because it achieved the highest ssDNA immobilization density, the PFPMA material had high patterning performance, and it was also compatible with the PAA and PMGI lift-off steps.

In order to characterize the EDC-based conjugation[61] of amine-terminal ssDNA with polymeric carboxyl groups before the full development of a repeatable process for generating PFPMA particles was established, carboxyl-functionalized polystyrene (PS) microspheres were used as a test vehicle. These particles are reasonably similar to printed PFPMA particles and can be acquired in large numbers at reasonable cost. These PS beads are compatible with applications where ssDNA is covalently bound to the

surface using EDC chemistry. They are also insoluble in the reaction solutions employed for the PFPMA processing. The primary goal of this analysis using PS beads was to determine whether polymer particles with carboxyl surface groups could be fully saturated with ssDNA such that the particles are rendered unreactive to subsequent functionalizations. This would allow for facet-specific ssDNA to be conjugated to the particles without any cross-functionalizing of strands. In addition, if the surface of the particles could not be easily saturated with ssDNA, an investigation into possible blocking strategies to passivate unreacted sites would be carried out using the PS beads.

5.2 Fluorescence-Based Flow Cytometry Analysis of EDC-Coupled ssDNA

6 μm-diameter carboxyl-modified PS beads (PolySciences) were used for the EDC reaction analysis because they roughly match the size scale of 5 x 5 x 2.5μm PFPMA parallelepipeds. A standard coupling protocol was designed to optimize the surface immobilization density of the PS beads with ssDNA. First, 50 μL of beads were dispensed into a 1.5 mL centrifuge vial. The beads were centrifuged four times, removing the supernatant and replacing it with 100 mM pH 4.5 MES for each cycle in order to remove any additives present in the stock solution. The beads pelleted very nicely, being concentrated in an angular clump at the bottom of the conical centrifuge vial. This allowed for easy and almost complete removal of the supernatant during each cycle. On the final cycle, the beads were left pelleted at the bottom of the vial for subsequent introduction of the immobilization solution. The immobilization solution consisted of a mixture of 100 mM pH 4.5 MES, 10 μM ssDNA, and 100 mM EDC. The ssDNA was thermally cycled on a PCR tool to separate entangled ssDNA chains for improved conjugation. The recipe comprised a quick ramp up to 80 °C, followed by a

slow 0.1 °C/sec ramp back down to ambient temperature. The dry EDC was dissolved in Millipore water and quickly added to the immobilization solution for each reaction. The immobilization solution was added to dried PS bead pellet and placed on a temperature-controlled shaker table rotating at 1,200 RPM to keep the beads moving in solution so they would not sediment during reaction. After reaction, the beads were rinsed via centrifugation and removal of supernatant four times with pH 8 0.4M triethylammonium bicarbonate (TEAB) buffer. The solutions were stored in the 0.4 M TEAB buffer at 4 °C if not being analyzed right away.

Several fluorophore-tagged ssDNA sequences were used to characterize the ssDNA functionalization density of the beads for various experiments. Table 5.1 is a summary of the sequences used including details on their modifications and fluorophore emission wavelengths.

Name	**5' Group**	**DNA Sequence**	**3' Group**	**Fluorophore Emission (nm)**
short	None	CATCA	NH2	N/A
A_{FAM}	Fluorescein (FAM)	$(AAAAA\ AAAAA)_5$	NH2	540
A'_{TYE}	Tye665	$(TTTTT\ TTTTT)_5$	NH2	665
B_{FAM}	Fluorescein (FAM)	CCTCC CCTTT TATGC GTATG TATGC GTGCG TGCGT	NH2	540
B'_{TYE}	Tye665	ACGCA CGCAC GCATA CATAC GCATA AAAGG GGAGG	NH2	665
A_{HEX}	Hexachloro-fluorescein (HEX)	$(AAAAA\ AAAAA)_5$	NH2	555

Table 5.1. Summary of ssDNA sequences used for the PS bead functionalization experiments.

In order to ascertain the reaction time necessary for adequate functionalization of the beads using EDC chemistry, three standard reactions were prepared using A_{HEX} ssDNA and allowed to run for 15 minutes, 2 hours, and 12 hours. The results of this experiment in Figure 5.1 show that the majority of the surface loading occurs within the first 15 minutes of reaction. The 2 hour reaction time had the highest fluorescence value, and by 12 hours, the loading had actually decreased a little. The 2 hour reaction time suggested by multiple manufacturers of PS beads designed for EDC chemistry (PolySciences, Bangs Labs, Pierce) appeared to be acceptable and was used for subsequent experiments.

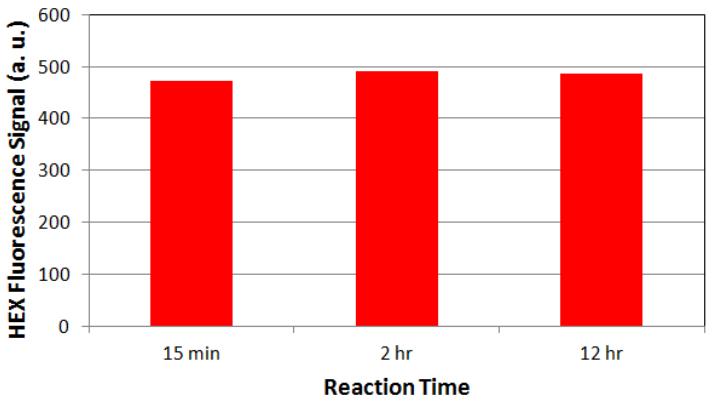

Figure 5.1. Fluorescence signals for A_{HEX}-labeled PS beads for three different reaction times: 15 min, 2 hr, and 12 hr.

DNA with the primary fluorophores used for the PS bead studies, Tye665 and HEX, were purchased (IDT) and functionalized onto sets of PS beads using immobilization reactions with varying ssDNA concentrations to get a set of relative calibration curves for each fluorophore. Two sets of beads, functionalized in 2 hour reactions with either A_{HEX} or B'_{TYE} ssDNA were run on a flow cytometer (FACSCalibur, BD Biosciences) to measure the fluorescence signal generated by the PS beads as shown in Figure 5.2. Six different bead reactions over a concentration gradient from 0 μM to 60

µM, where the 0 µM concentration represents a no-DNA background, were run for each fluorophore-labeling. At a concentration of about 10 µM ssDNA, the concentration starts to stabilize for both the Tye665 (Fig. 5.2a) and HEX (Fig. 5.2b) functionalized beads. The fluorescence continues to increase at a slower rate until the maximum 60 µM ssDNA concentration. The 60 µM level represents a large portion of the stock solutions for each fluorophore-labeled ssDNA sequence which can be quite expensive. Accordingly, 10 µM concentrations of fluorophore-labeled ssDNA were used for the majority of the PS bead experiments.

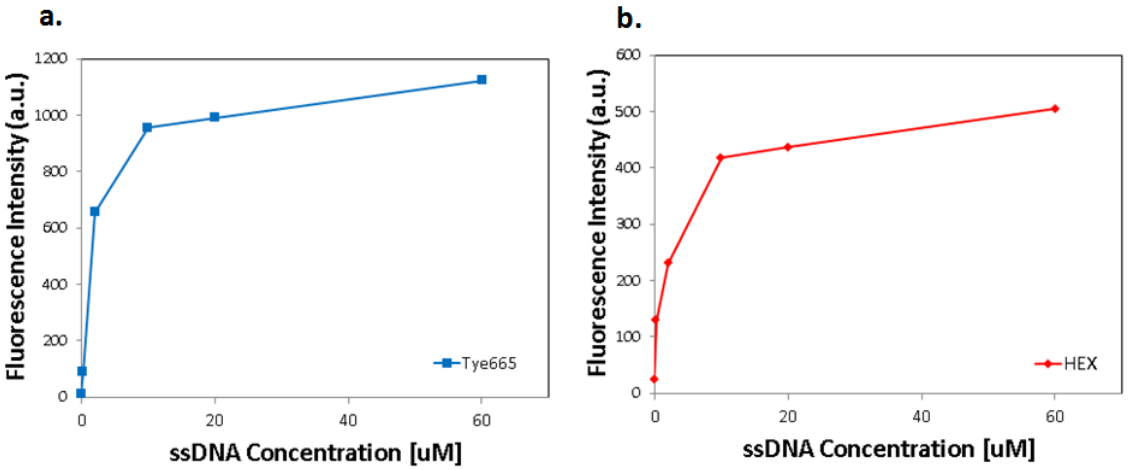

Figure 5.2. Fluorescence intensity curves of 6 µm polystyrene beads functionalized with a gradient of concentrations from 0 to 60 µM of a. A_{HEX} (red) and b. B'_{TYE} (blue) ssDNA sequences.

The surface functionalization of ssDNA on the beads was also measured using flow cytometry for a range of EDC concentrations. Immobilizaton solutions for the A_{HEX} and B'_{TYE} sequences were prepared for a gradient of EDC concentrations from 0 mM to 500 mM (100 max for the A_{HEX} ssDNA) . The beads were reacted using the standard protocol to yield the fluorescence versus EDC concentration plot in Figure 5.3. In the A_{HEX} plot, the ssDNA loading appears to plateau starting at the 10 mM EDC

concentration, slightly increasing up to the 100 mM condition. The B'$_{TYE}$ plot also begins to plateau at 10 mM, but the concentration continues to increase modestly up to 500 mM. Unfortunately, EDC concentrations above 100 mM were problematic because the concentration was so high that the PS beads started to aggregate, which may have led to the more significant increase at the 500 mM concentration condition for the B'$_{TYE}$ plot. The 100 mM EDC condition was primarily used for subsequent experiments because at this level, no aggregation was seen. For the 0 mM concentration conditions where no EDC was used in the immobilization solution, the fluorescence signals were comparable to signals for PS beads which had not undergone any reaction.

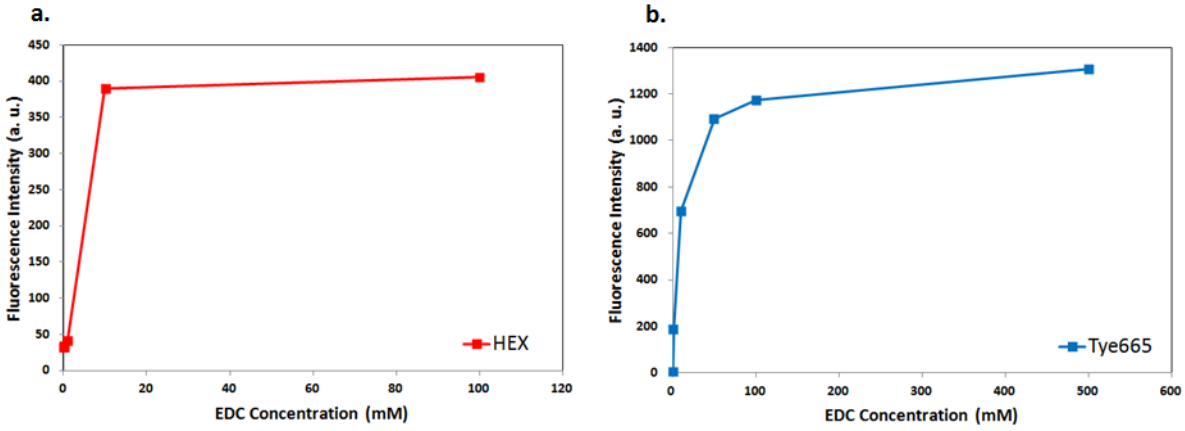

Figure 5.3. Fluorescence intensity curve of a. A$_{HEX}$ (red) and b. B'$_{TYE}$ (blue) 6 µm polystyrene beads functionalized with a gradient of EDC concentrations from 0 to 100 mM and 0 to 500 mM, respectively.

5.3 Analysis of ssDNA Double-Functionalization

An experiment was designed to determine the extent to which the surface of the PS beads was saturated with ssDNA during EDC-mediated immobilization. To do this, an experiment to double-functionalize beads that were already functionalized with A$_{HEX}$

ssDNA was performed. Three different sets of PS beads were prepared for analysis on the flow cytometer. This first sample was a 4x rinsed aliquot of the beads with no surface functionalization to provide a background signal. The second and third samples were functionalized and rinsed using the standard protocol with either A_{HEX} or B'_{TYE} ssDNA. The HEX and Tye665 fluorescence signals for each set of these beads are shown in Figure 5.4 (a., b., and d., respectively). From this plot, we can see that the unreacted beads have a small background signal in the HEX fluorescence channel, but a negligible background signal in the Tye665 channel. The A_{HEX}-labeled sample was then exposed again to the standard immobilization solution, but this time using B'_{TYE} ssDNA. The resulting Tye665 signal shown in Figure 5.4c is approximately 40% of the height of the standard B'_{TYE} reaction in Figure 5.4d, suggesting that a significant amount of the secondary B'_{TYE} ssDNA is binding to unreacted sites on the surface of the beads.

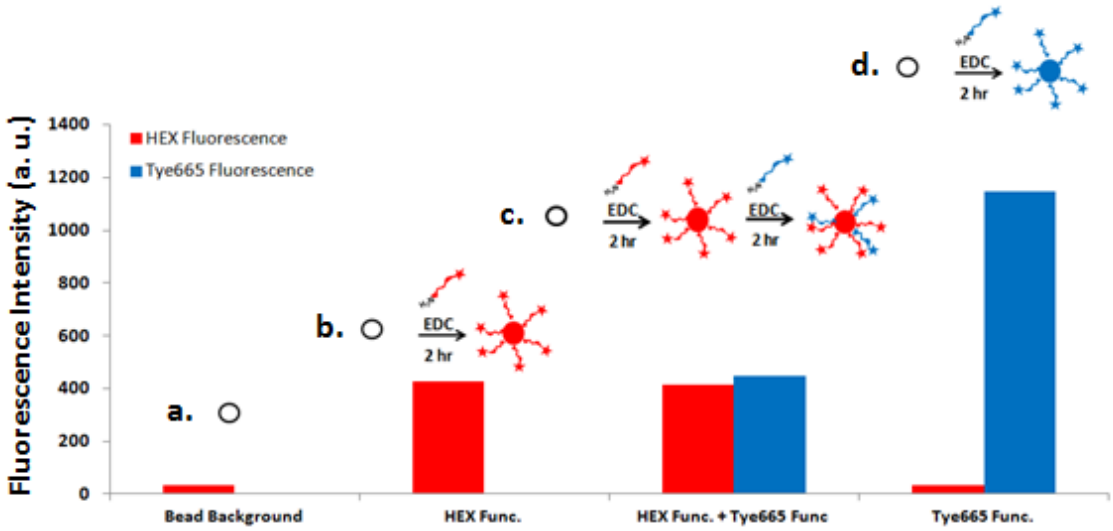

Figure 5.4. HEX (red) and Tye665 (blue) fluorescence signals measured on a flow cytometer for a. naked PS beads with no ssDNA (background signals), b. PS beads functionalized with A_{HEX} ssDNA, c. A_{HEX}-labeled beads double-functionalized with B'_{TYE} ssDNA, and PS beads functionalized with B'_{TYE} ssDNA.

In an attempt to try to better saturate the surface of the PS beads, an aliquot of beads was functionalized repeatedly with A_{FAM} ssDNA using the standard protocol nine times in series, with reaction times of 15 minutes each. The results of this repeated functionalization in Figure 5.5 show a steady increase at the beginning of the reaction sequence, followed by a drop of after the sixth 15-minute reaction. After the ninth reaction, the beads starting to stick to the sides of the centrifuge vial making fluorescence readings on the cytometer difficult.

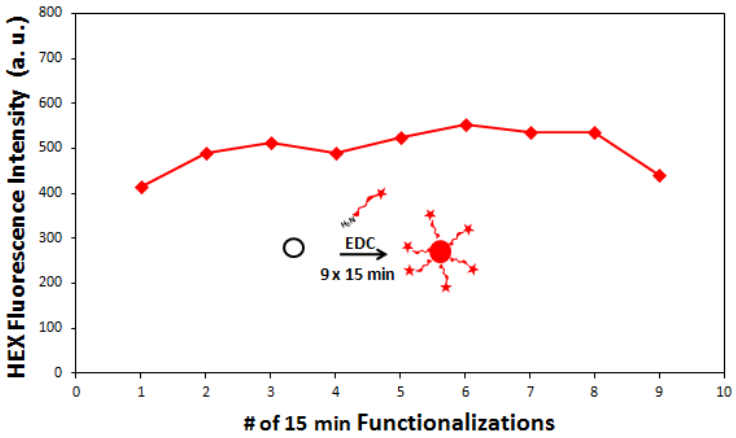

Figure 5.5. Chronological HEX fluorescence signals for 9x 15-minute ssDNA functionalization reactions with PS beads.

After the 9x reaction sequence, these same beads were then double-functionalized with a secondary ssDNA, B'_{TYE}, using the standard 2 hour functionalization protocol. The resulting Tye665 fluorescence signal is shown in Figure 5.7c. This result is plotted along with the Tye665 fluorescence signals for naked PS beads (Fig 5.6a), the PS beads functionalized with A_{HEX} using the 9x 15-minute reaction protocol (Fig. 5.6b), and PS beads functionalized with B'_{TYE} using the standard 2-hour protocol (Fig. 5.6d) to provide a minimum and maximum signal range for comparison. The double functionalized beads had a Tye665 fluorescence that was approximately 26% of the value for the standard 2-

hour B'$_{TYE}$ reaction. While this is an improvement, this value still represents a significant number of ssDNA double functionalized to the surface which could be detrimental to specificity in a polyfaceted particle platform with different ssDNA on each face.

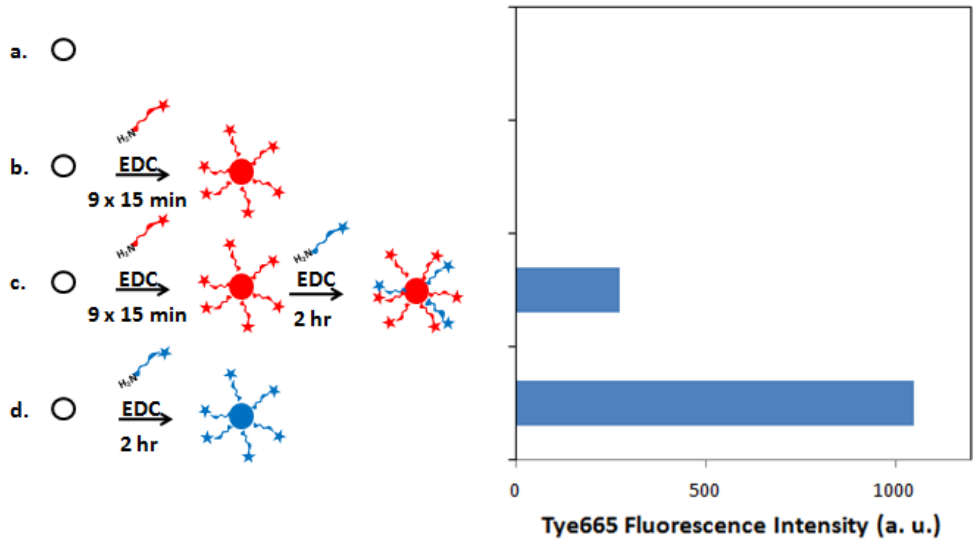

Figure 5.6. Tye665 fluorescence signal results for a. naked PS beads with no functionalization, b. PS beads functionalized in 9x 15-minute reactions with A$_{HEX}$, c. the 9x A$_{HEX}$-functionalized beads after being double-functionalized with B'$_{TYE}$ using the standard 2-hour protocol, and d. PS beads functionalized with B'$_{TYE}$ using the standard 2-hour protocol as a reference.

5.4 Development of Blocking Process

The results from the double-functionalization experiments prompted an investigation of possible species to block the unreacted sites remaining after ssDNA surface functionalization. Three main types of candidates were selected: amines, nucleoside-based molecules, and surfactants. The amines included 2-methoxyethylamine and aminated methoxy-poly(ethylene glycol) (referred to as methoxy-PEG-amine). The nucleoside-based molecules included a 5-mer sequence of aminated ssDNA (denoted

"short") and the purine nucleoside, adenosine. Tween20 and sodium dodecyl sulfate (SDS) were auditioned as the non-ionic and ionic surfactants, respectively, and isourea as also selected in an attempt to passivate residual carboxyl groups on the surface of the beads. Several samples of naked PS beads were incubated with each of these species using the standard functionalization protocol and then rinsed 4x with 100 mM MES buffer. Each bead sample was then functionalized with A_{HEX} ssDNA using the standard functionalization protocol, and the resulting fluorescence was read on a flow cytometer yielding the chart in Figure 5.7. All of these blocking candidates significantly reduced the HEX fluorescence signal of the beads, with the exception of the 5-mer ssDNA which caused a slight increase in the signal. It is evident from the plot that the 0.1 wt% Tween20 treatment was by far the most effective blocking agent, reducing the HEX signal by approximately 94%. This is potentially due to a significant adsorption of the Tween20 surfactant molecules at the surface of the particles, which is apparently stable enough to withstand a subsequent 2-hour EDC coupling reaction under agitation.

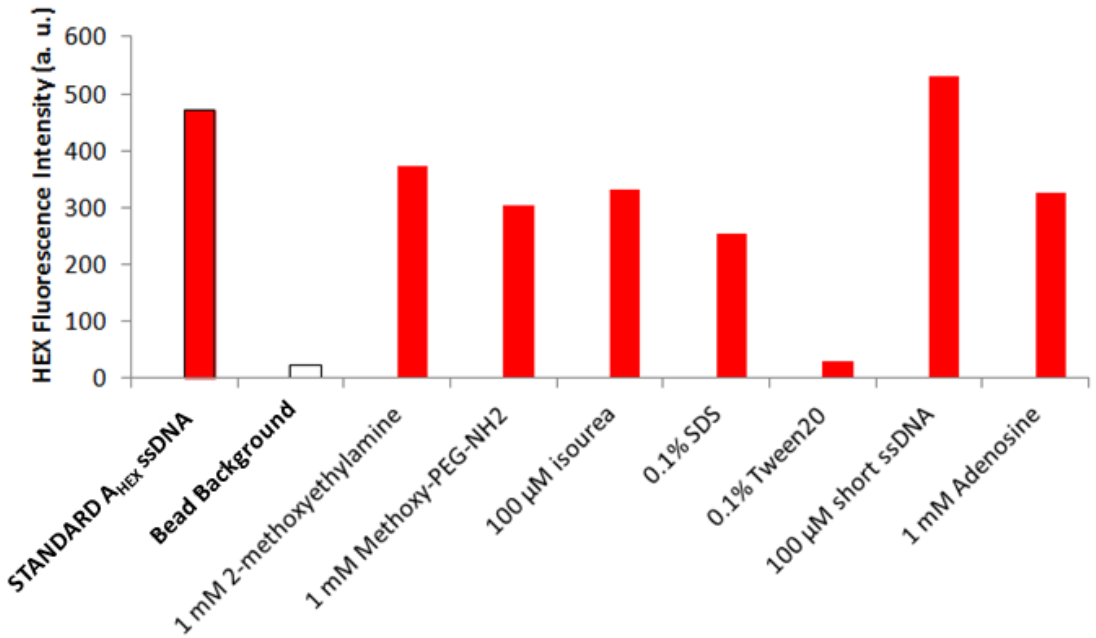

Figure 5.7. Analysis of potential blocking candidates via functionalization of naked 6 µm PS beads with A_{HEX} using the standard ssDNA functionalization protocol.

This fortunate result led to further exploration into the use of Tween20 as a surfactant-based blocking strategy. To test the performance of Tween20 in a double-functionalization scenario, two aliquots of PS beads were functionalized with A_{FAM} ssDNA using the standard 2-hour functionalization protocol. Afterwards, each sample of beads was rinsed 4x in 100 mM buffer. One bead sample was immediately double-functionalized with B'_{TYE} ssDNA using the standard functionalization protocol, whereas the other was treated with 1 wt% Tween20 in DI water for 24 hours under 1,200 RPM of agitation on a shaker table. After this blocking step, the second bead sample was also functionalized with B'_{TYE} ssDNA using the standard functionalization protocol. After rinsing, FAM and Tye665 fluorescence signals were taken on a flow cytometer as shown in Figure 5.8. In Figure 5.8a, a significant double-functionalization denoted by the high Tye665 signal (blue) is evident, as previously seen. In Figure 5.8b, however, the Tye665

fluorescence is drastically reduced to approximately 1.5% of the value for a B'$_{TYE}$ functionalization process using the standard 2-hour protocol on naked beads.

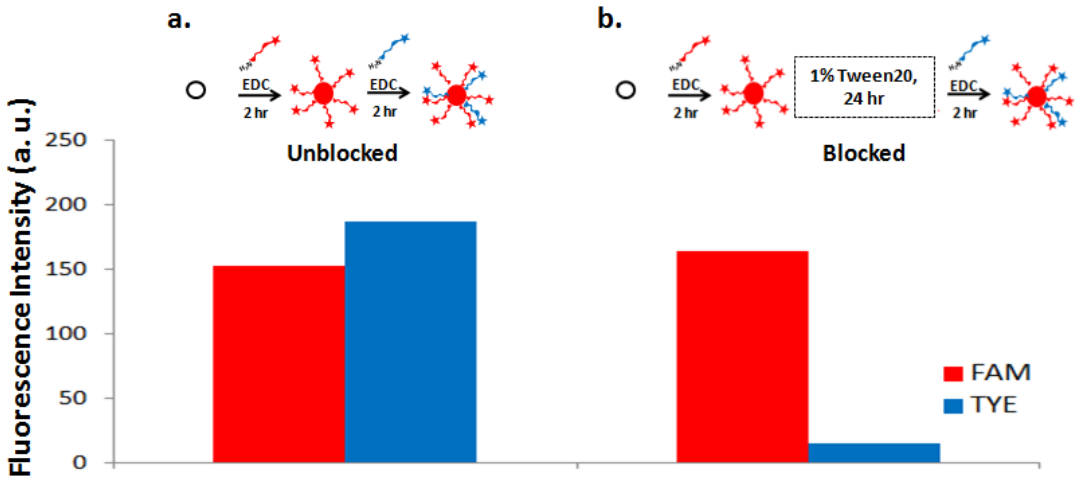

Figure 5.8. HEX and Tye665 fluorescence signals plotted on the same axis for a. an unblocked double-functionalization process where B'$_{TYE}$ is functionalized over A$_{HEX}$ ssDNA, and b. the same double functionalization process with an intermediate blocking treatment of 1 wt% Tween20 surfactant for 24 hours.

5.5 HYBRIDIZATION VERIFICATION OF TWEEN20 BLOCKING PROCESS

These Tween20 blocking results were very encouraging, however, to truly understand the potential of this blocking process as it applies to the assembly of polyfaceted particles, a verification of hybridization was necessary. An imaging flow cytometer (ImageStream, Amnis) was used for this analysis because it is not only capable of measuring fluorescence at several different wavelength ranges, but it has the capability to take thousands of images of micron-scale particles and particle aggregates each second. The tool accomplishes this pumping a highly-focused stream of the particle solution through a capillary in the flow cell of the tool. This stream is optimized such that the particles flow nearly one-at-a-time past incident bright field and laser sources,

yielding vast numbers of images, fluorescence data at multiple wavelengths, and bright field scattering data. This technique was used to quantify the extent to which ssDNA-functionalized PS beads were participating in assembly, in order to correlate the amount of double-functionalization to actual unwanted assembly yield.

Four assembly schemes were chosen for hybridization analysis. Scheme I (Fig. 5.9a) was designed as a control assembly wherein cognate B_{FAM} (red) and B'_{TYE} (dark green) PS beads functionalized using the standard 2-hour protocol were generated. These beads were mixed together in approximately a 1 : 1 ratio, vortexed for 30 seconds, and then inserted into an imaging flow cytometer for analysis. Figure 5.9b is log-log scatter plot of the Tye665 and FAM fluorescence signals for each bead or bead assembly that passed through the flow cell of the imaging cytometer. The linear groups of white data points near the axes represent unbound B_{FAM} and B'_{TYE} beads which did not participate in assembly, and the green and blue colored data points between these two groups represent the beads which were found in assemblies of two or more. The green data points in within the blue boundary represent only beads which were found to be bound together as dimers. The corresponding blue and green percentages in the upper left hand of the plot indicate the percentage of beads which participated either in dimer (green) or higher order (blue) assembly. For the cognate assembly in Scheme I, 26% of the particles participated in assembly, with 21% assembling in dimer format.

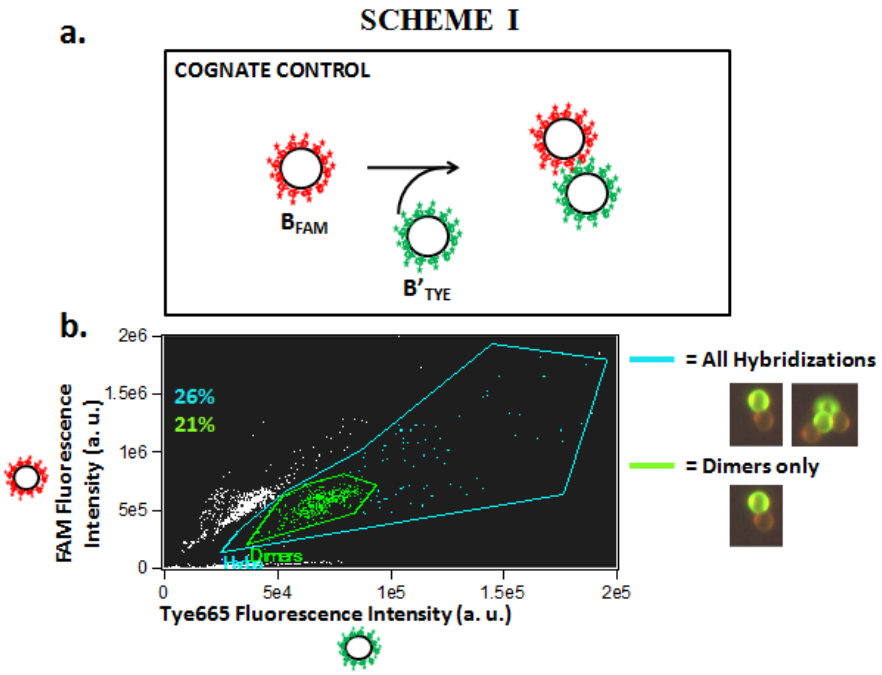

Figure 5.9. a. Graphic description of Scheme I assembly of cognate B_{FAM} (red) and B'_{TYE} (dark green) PS beads. b. FAM and Tye665 fluorescence signals plotted against each other on a log-log plot grouped into regions showing all hybridizations (blue) and only dimer hybridizations (green), including image-labeled legend.

Assembly scheme II was designed to ascertain the amount of binding present in a mixture of non-cognate sets of PS beads (A'_{TYE} and B'_{TYE}, both green), wherein the A'_{TYE} beads were double-functionalized with B_{FAM} before assembly (Fig. 5.10a). The fact that one set of the unbound particles shows up with a significant signal in the FAM detection channel shows that the double-functionalized particles had a significant amount of B_{FAM} ssDNA on the surface. These particles hybridized at a frequency very similar to the cognate beads in scheme I at values of 22% and 19% for the assembly and dimer assembly configurations, respectively, indicating that even a relatively low amount of double-functionalization is capable of effectively causing undesired assembly of the beads.

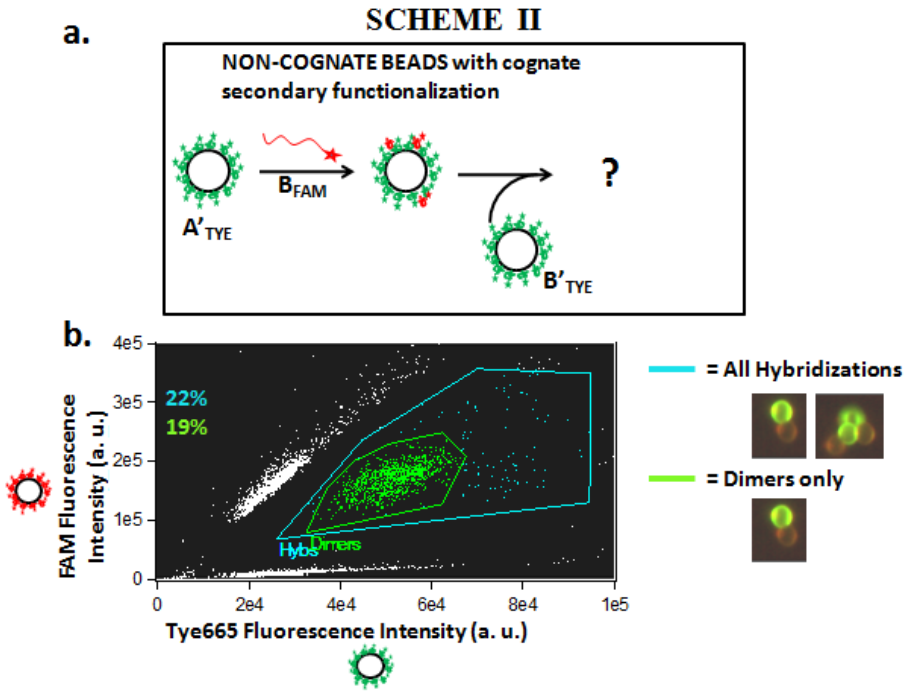

Figure 5.10. a. Graphic description of Scheme II assembly of non-cognate double-functionalized A'$_{TYE}$ (dark green) and B'$_{TYE}$ (dark green) PS beads. b. FAM and Tye665 fluorescence signals plotted against each other on a log-log plot grouped into regions showing all hybridizations (blue) and only dimer hybridizations (green), including image-labeled legend.

Assembly scheme III is a hybridization verification of the Tween20 surfactant treatment that seemed to block double-functionalization quite well in the previous section of this chapter. Once again, non-cognate sets of PS beads (A'$_{TYE}$ and B'$_{TYE}$) were used, but in this scheme, the double-functionalization with B$_{FAM}$ occurred after a 24-hour 1% Tween20 treatment for 24 hours (Fig. 5.11a). In Figure 5.11b, a significantly lower rate of self assembly is seen wherein 5% of the beads assemble into any hybridization configuration, and 4% of the beads in the solution were found as dimers. This represents a 77% reduction in the overall assembly yield of the beads with respect to the double-functionalized non-cognate control case in Scheme II. While this assembly yield is still

significant, the reduction due to the Tween20 blocking treatment is impressive and encouraging.

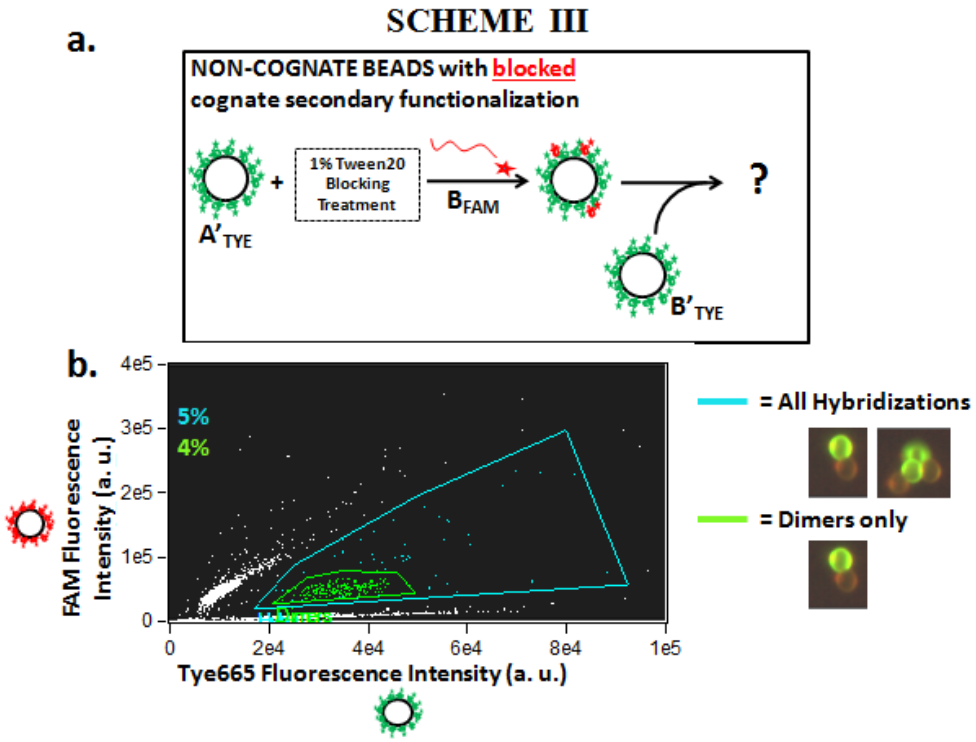

Figure 5.11. a. Graphic description of Scheme III assembly of non-cognate blocked and double-functionalized A'$_{TYE}$ (dark green) and B'$_{TYE}$ (dark green) PS beads. b. FAM and Tye665 fluorescence signals plotted against each other on a log-log plot grouped into regions showing all hybridizations (blue) and only dimer hybridizations (green), including image-labeled legend.

Finally, in scheme IV, the same cognate sets of PS beads from scheme I (A'$_{TYE}$ and B'$_{TYE}$), but in this case, the A'$_{TYE}$ beads were double functionalized with B$_{FAM}$ ssDNA before assembly. This scheme (Fig 5.12) was designed as a control to verify that the 24-hour Tween20 treatment was not somehow indirectly inhibiting the general

assembly of the particles. Surprisingly this blocking control scheme did just the opposite, increasing the overall hybridization yield by 31%.

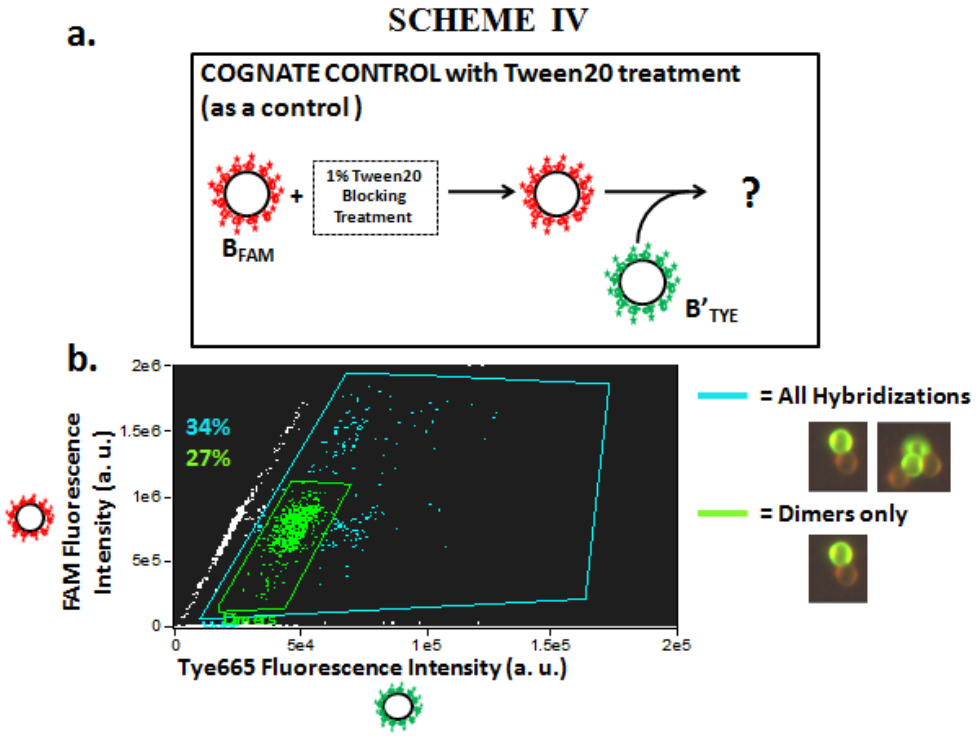

Figure 5.12. a. Graphic description of Scheme I assembly of cognate blocked B_{FAM} (red) and B'_{TYE} (dark green) PS beads. b. FAM and Tye665 fluorescence signals plotted against each other on a log-log plot grouped into regions showing all hybridizations (blue) and only dimer hybridizations (green), including image-labeled legend.

Figure 5.13 is a summary of the overall and dimer-only hybridization yields for the four assembly schemes. A relative comparison of the overall hybridization yields for scheme II and scheme III suggest that the Tween20 blocking treatment significantly suppressed the amount of undesirable double-functionalization occurring in the assemblies. The hybridization data for scheme IV indicates that the blocking process does not interfere with cognate assembly, and in fact, it improves it. The relative

similarity of the hybridization values for scheme I and scheme II show that assembly due to double-functionalization is quite significant and should be major problem for a platform based on the sequence-specific self assembly of polyfaceted particles.

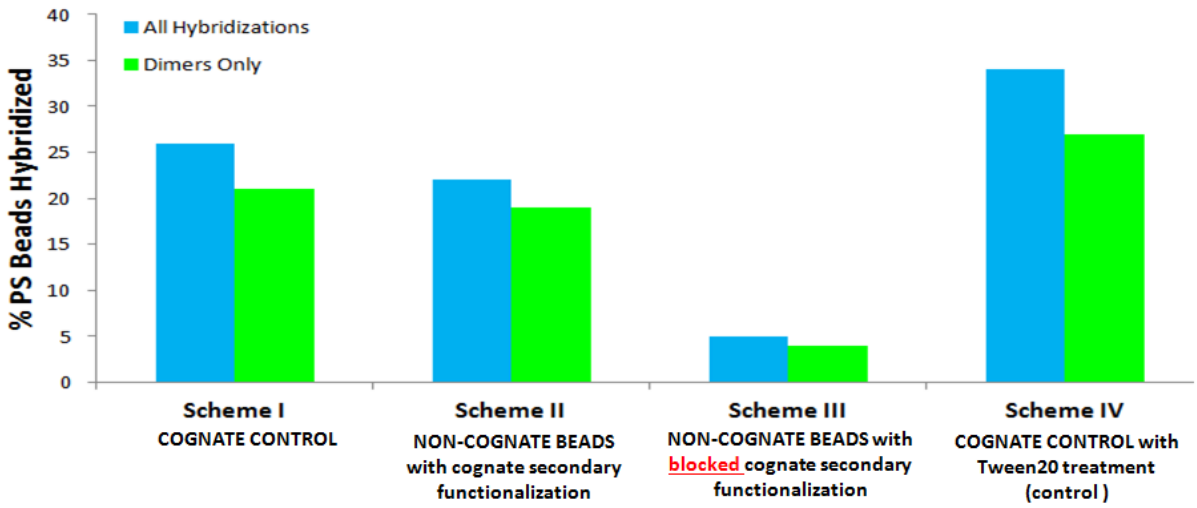

Figure 5.13. Summary of overall and dimer-only hybridization yields for the assembly schemes used as a verification of the Tween20 blocking treatment.

5.6 CONCLUSIONS

The use of 6μm-diameter carboxyl-modified PS microspheres as an analog for patterned polyfaceted parallelepipeds was very useful in developing and optimizing the assembly process. It was discovered that not only is there significant double-functionalization of ssDNA for two sequential ssDNA functionalizations of the same particle, but that this has a significant impact on selective particle hybridization yield. This double-functionalization appears to be caused by a lack of complete saturation of reactive carboxyl sites on the surface of the beads, which so far has been unavoidable. Fortunately, a solution to this problem in the form of a blocking strategy involving a non-

ionic surfactant, Tween20, was discovered in an investigation of possible blocking agents. This particular blocking agent appeared to significantly suppress double-functionalization at the surface of the particles, reducing overall undesired hybridization yields by 77%, which should be able to significantly improve the selectivity of the polyfaceted patterned copolymer platform.

Chapter 6: Particle Assembly

Reprinted in part with permission from Deschner, R.; Tang, H.; Allen, P.; Hall, C.; Hlis, R.; Ellington, A.; and Willson, C. G., Chem. of Mat. (submitted November 3rd, 2013), Copyright the American Chemical Society.

6.1 INTRODUCTION

Organized selective self assembly in solution is accomplished when different sets of building blocks are introduced in an environment that allows them to interact with each other at a high rate. This process is similar to a molecular chemical reaction where different molecules are constantly coming into close enough contact with each other to form chemical bonds. If the reaction is reversible in nature, these bonds are formed and broken at a high rate and the molecules are able to bind with a large number of other unique molecules to form steady state concentrations of products.

In macro-scale self assembly, building blocks can be designed such that they form stable, specific associations with specific partner building blocks when they are allowed to interact with each other. However in the case where these blocks participate in associations with a range of different energies, a disruptive force is required to break up lower-energy associations so that the higher-energy associations are preferred. This gives the system a reversible characteristic which can be exploited to form selective configurations of higher order.

An experiment performed by Dr. Peter Carmichael exemplifies this phenomenon. Five polycarbonate tiles were fabricated, each with two different "reactive" sides designed to contain different combinations of three magnets with either "north" or "south" orientation as shown in Figure 6.1a. These tiles were labeled "T", "E", "X",

"A", and "S" and designed such that they would bind together, if complementary magnets were brought into contact with each other, to spell the word "TEXAS". The tiles were floated onto an air-water interface in a petri dish and placed on a shaker table to induce interaction (Fig. 6.1b). After a short time, the tiles began to collide with each other and low-energy associations were made when one or two complementary magnets came into contact, making temporarily stable couplings. If the shaking force was high enough, these partial associations became reversible, and after longer periods of time, full three-magnet associations began to appear. After five minutes of shaking, equilibrium was established in which all of the magnets had found their full complements and the word "TEXAS" was spelled out in a stable sequence as shown in Figure 6.1c and Figure 6.1d.

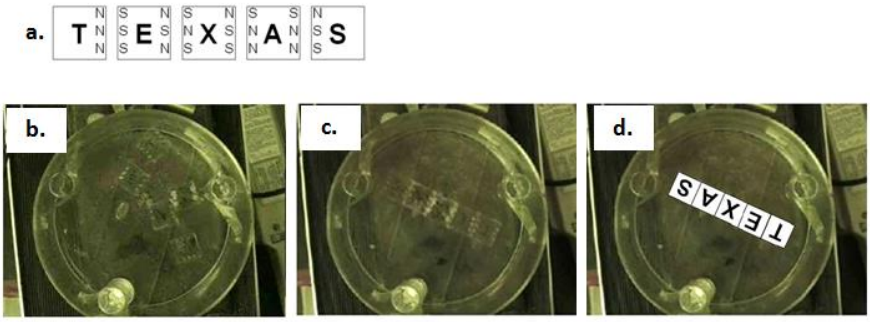

Figure 6.1. Centimeter-scale self assembly of magnet-laden polycarbonate tiles at an air-water interface in a petri dish. a. Magnet layout for each of the five tiles. b. Completed stable assembly of the tiles in the desired configuration. c. Completed assembly labeled with the letter on each tile. *Reprinted with permission from Dr. Peter Carmichael.*

This assembly scheme was possible because of three key factors: 1. there was a gradient of associative forces, 2. particle interactions were induced in the system, and 3. the disruptive force (mechanical mixing) was able to overcome at least some of the associative forces (one and two magnet couplings) so that new configurations could be

formed. If the disruptive force was too low or the associative forces too high, the particles would have formed initial couplings and then stopped, incorrectly forming the TEXAS sequence. If the disruptive force was too high and the associative forces too low, the particles would not have formed any stable couplings. Control of these associative and disruptive forces, along with adequate particle interaction, is vital establishing ordered assemblies at equilibrium.

Similarly, in the case of DNA-assisted assembly of particles, hybridization must be designed such that it is able to overcome significant tensile forces caused by shear acting on the particles in solution during mixing. A very useful characteristic of DNA is that complementary strands of it can form very strong hydrogen bonds in series, while non-complementary strands have very weak affinities[68]. This is what gives DNA hybridization its binding selectivity, making sequence-specific self assembly of particles possible. These associations are characterized by the melting temperature (T_m) of the hybridized DNA, which is defined as the temperature at which 50% of the strands are participating in hybridization. This characteristic temperature is a function of system conditions such as salt concentration, as well as a function of sequence coding and length. In a system with equal amounts of two complementary ssDNA strands, A and A', which form a hybridized strand, AA', the equilibrium constant is defined as:

$$K = \frac{[AA']}{[A][A']} \tag{6.1}$$

where [A], [A'], and [AA'] are the concentrations of the single and double stranded DNA in the solution. At the melting temperature, the numbers of single strands which are hybridized and non-hybridized are equal. If the total concentration of ssDNA in the solution is denoted as C_{ssDNA}, then, at the melting temperature:

$$K = \frac{\frac{1}{4}C_{ssDNA}}{\frac{1}{4}C_{ssDNA} * \frac{1}{4}C_{ssDNA}} = \frac{C_{ssDNA}}{4} \tag{6.2}$$

From thermodynamics, the change in Gibbs free energy is:

$$\Delta G° = \Delta H° - T\Delta S° = -RTlnK \tag{6.3}$$

Substituting our new expression for K into this equation and solving yields:

$$T_m = \frac{\Delta H°}{\Delta S° + Rln(\frac{C_{ssDNA}}{4})} \tag{6.4}$$

The so-called nearest-neighbors method is commonly used to predict the thermodynamic parameters necessary for the calculation of melting temperatures. This model established thermodynamic values for the interactions of isolated complementary sets of two base pairs in a double helix. The total Gibbs free energy of the double strand can then be calculated by taking the sum of the individual contributions two base pairs at a time[69]:

$$\Delta G°_{Total} = \Delta G°_{Init.w/\ term\ GC} + \Delta G°_{Init.w/\ term\ AT} + \sum_i n_i\, \Delta G°(i) + \Delta G°_{symmetry}$$

(6.4)

Where the two $\Delta G°_{Init}$ terms are the change in Gibbs free energy for the initiating base pairs at each terminus, the $\Delta G°_{Symmetry}$ term is a correction for the symmetry of self-

complementary duplexes, the $\Delta G°(i)$ term is the Gibbs free energy of the nearest neighbor base pairs (see Table 6.1), and n_i is the number of times each unique nearest neighbor base pair shows up in the double helix.

Sequence	ΔH° (kcal/mol)	ΔS° (cal/K*mol)	$\Delta G°_{37}$ (kcal/mol)
AA/TT	-7.9	-22.2	-1.01
AT/TA	-7.2	-20.4	-0.88
TA/AT	-7.2	-21.3	-0.58
CA/GT	-8.5	-22.7	-1.45
GT/CA	-8.4	-22.4	-1.44
CT/GA	-7.8	-21.0	-1.28
GA/CT	-8.2	-22.2	-1.30
CG/GC	-10.6	-27.2	-2.17
GC/CG	-9.8	-24.4	-2.24
GG/CC	-8.0	-19.9	-1.84
Initial w/ term GC	0.1	-2.8	0.98
Initial w/ term AT	2.3	4.1	1.03
Symmetry correction	0	-1.4	0.43

Table 6.1. Thermodynamic parameters for nearest neighbor melting temperature calculation at 37 °C w/ 1 M NaCl. Adapted with permission from [69].

We can see from this table that nearest neighbors with G-C pairing have higher free energies than those with A-T pairing. This stems from the fact that G-C base pairs form three hydrogen bonds, whereas A-T pairs only form two as shown in Figure 6.2. Thus, the GC content of the duplex can be increased for a given strand length to increase the melting temperature during design[70].

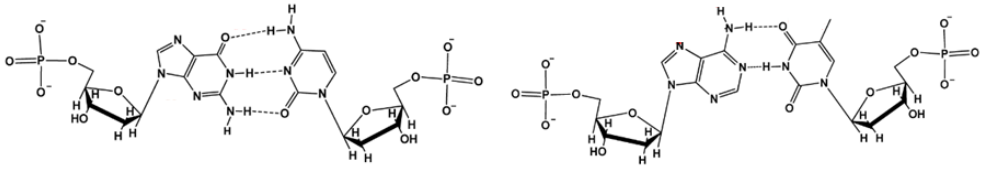

Figure 6.2. Chemical structure of G-C and A-T Watson Crick base pairing. Reprinted with permission from [58]

Salts such NaCl can also be added to the DNA solution to modify the melting temperature[71]. The influence of salt ions on the free energy of the double helix is dependent on its length. The salt correction for the free energy of the double DNA at 37 °C can be estimated by:

$$\Delta G°_{37}([NA^+]) = \Delta G°_{37}(NN, 1M\ NaCl) - 0.114 * N * \ln[Na^+] \quad (6.5)$$

where $\Delta G°_{37}([NA^+])$ is the free energy of a double stranded DNA helix at a given salt concentration, $\Delta G°_{37}$(NN, 1M NaCl) is the free energy predicted for the DNA using the nearest neighbor parameters, N is the number of phosphates in the double strand divided by two, and $[Na^+]$ is the salt concentration of the solution. This correction is necessary the salt shields the charge repulsion between the strands, making the double helix more stable and increasing the melting temperature. These methods are useful for estimating melting temperatures for complementary DNA strands of any sequence, making it possible to easily design DNA for self assembly with a desired hybridization strength.

6.2 INDUCED PARTICLE INTERACTION

Once particles with ssDNA conjugated to the surface had been successfully generated, we explored several methods for inducing interaction between different sets of particles with complementary DNA. Above the micron scale, polymer particles in aqueous solutions are generally non-colloidal solutions which sediment to the bottom of the vessel they are contained in. Unlike Brownian motion at the molecular level which is rapid, erratic, and does not exhibit long-range order, bulk motion due to mechanical

mixing is much less efficient at inducing particle interactions. In addition, since these particles are denser than water, they only remain suspended for short periods of time, generally less than 15 minutes. In dilute particle solutions which are static, the time during which different sets of particles interact is limited to the sedimentation time. This interaction time can be increased by agitating the solution aggressively enough to overcome the force of gravity; however, this action also introduces high shear forces which can decouple particle aggregates.

6.3 Assembly Verification Methodologies and Self Assembly Results

Several methodologies were utilized to verify that sequence-specific particle assembly was taking place. Initial attempts at verification were carried out using optical or fluorescence microscopy. These techniques turned out to be useful for determining that the particles were coupling together, but could only be used in a qualitative manner. Eventually, use of a sophisticated imaging flow cytometer (ImageStream, Amnis) was used to detect the coupling of the particles, which turned out to be more efficient and yielded quantitative results. The following ssDNA sequences in Table 6.2 were used for the assembly verification experiments.

Name	5' Group	DNA Sequence	3' Group	Fluorophore Emission (nm)
PolyA	None	$(AAAAA\ AAAAA)_5$	NH2	N/A
PolyT	None	$(TTTTT\ TTTTT)_5$	NH2	N/A
A_{FAM}	Fluorescein (FAM)	$(AAAAA\ AAAAA)_5$	NH2	540
A'_{TYE}	Tye665	$(TTTTT\ TTTTT)_5$	NH2	665
B_{FAM}	Fluorescein (FAM)	CCTCC CCTTT TATGC GTATG TATGC GTGCG TGCGT	NH2	540
PolyA30	None	$(AAAAA\ AAAAA)_3$	NH2	N/A
$PolyA30_{HEX}$	Hexachloro-fluorescein (HEX)	$(AAAAA\ AAAAA)_3$	NH2	555
$PolyT30_{HEX}$	Hexachloro-fluorescein (HEX)	$(TTTTT\ TTTTT)_3$	NH2	555

Table 6.2. Custom ssDNA sequences designed for flow cytometry assembly verification experiments.

6.3.1 Assembly verification by fluorescence microscopy

An optical microscope fitted with a system for exciting fluorophores and spatially displaying their emitted light at specific wavelengths (IX71, Olympus) was used to detect fluorescently-tagged particles. These particles were printed out of PMMA-PFPMA with either Coumarin-6 or Nile Blue dye incorporated into the copolymer before processing. The fluorescence details of the dyes are summarized in Table 6.3.

	Excitation Peak (nm)	Emission Peak (nm)	Filter Wavelength (nm)
Coumarin-6	458	505	508
Nile Blue	630	640	670

Table 6.3. Excitation and emission peak values for Coumarin-6 and Nile Blue, including the center wavelength of the filter used for detection.

The films were printed into 5 x 10 μm rectangles on 200 nm of poly(acrylic acid) (PAA)and, two sets of particles were functionalized with 50 bp single strands of polyA or polyT DNA using a reaction buffer consisting of 100 mM pH 11 carbonate buffer and 10 μM of ssDNA. The Nile blue-dyed particles were functionalized with polyA and the Coumarin-6-dyed particles were functionalized with polyT. These functionalizations were only performed on the top surface of the particles to demonstrate the assembly of particle dimers. After functionalization and patterning, the particles were lifted off the silicon substrate by dissolving the PAA with DI water for 30 minutes. A solution of the particles was then dispensed onto a microscope slide for imaging. The images in Figure 6.3 show the particles under bright field, and using filters optimized for the emitted wavelengths of Coumarin-6 and Nile Blue. It is easy to discern the ssDNA functionalization of the particles in the bright field images based on the fluorescence in the Coumarin-6 and Nile Blue images.

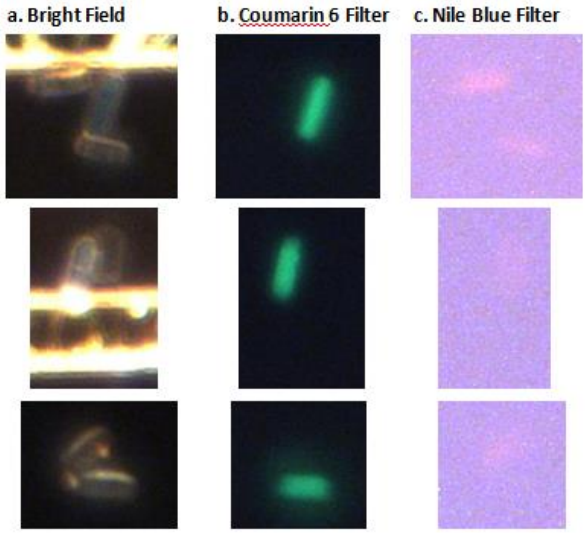

Figure 6.3. Microscope images of dyed polymer particles taken with a. bright field illumination, b. a filter collecting emitted light from Coumarin-6 dye (polyT ssDNA), and c. a filter collecting emitted light from Nile Blue dye (polyA ssDNA).

The filter used to detect the Nile Blue fluorescence was not very well matched to its emission peak, however the particle can still be roughly visualized. This technique is very useful for independently imaging differently-dyed particles that have been coupled together, unfortunately, the hybridization observed in this experiment was very poor, and less than 5% of the 735 particles seen appeared to be possible hybridizations. The weak binding results seen were due to the direct conjugation of amine-terminated ssDNA to PMMA-PFPMA particles. After performing these experiments it was discovered that the use of carbodiimide chemistry significantly increased ssDNA surface densities. This chemistry was used for the rest of the hybridization verification experiments in this chapter. Fluorescence microscopy was not very effective at detecting the fluorescence of surface-functionalized fluorophore-terminated ssDNA, however it worked well for particles where large quantities of dye was mixed into the copolymer matrix before patterning, or polystyrene beads with denser functionalizations of ssDNA.

6.3.2 Shape-based assembly verification by optical microscopy

Another strategy for verifying particle hybridization was to use different shapes which correspond to different ssDNA functionalizations. These particles were designed to be distinguishable by shape without the aid of fluorescence microscopy. For this experiment 6 μm carboxyl-modified polystyrene particles and 5 x 5 x 2.5 μm parallelepipeds were functionalized with cognate and non-cognate ssDNA strands to demonstrate selective hybridization without the aid of fluorescence. Two sets of 6 μm polystyrene particles were functionalized for 2 hours with 1,200 RPM of agitation in a reaction buffer consisting of 100 mM MES, 100 mM EDC, and 10 μM of either A'_{TYE} or B_{FAM} ssDNA; and then the beads were then rinsed 4 times with Millipore water. 2.5 μm thick PMMA-PFPMA particles were printed into 5 x 5 μm squares on 200 μm of poly(methyl glutarimide) (PMGI). The particles were printed and functionalized in situ using the same reaction buffer for 12 hours with A_{FAM} ssDNA and then released with a 4 : 1 dilution of potassium borates (400k, Clariant) stripper. A cognate mixture of A_{FAM} parallelepipeds and A'_{TYE} beads was mixed together, vortexed for 30 seconds, and then dispensed onto a microscope slide as shown in Figure 6.4a. A non-cognate mixture of A_{FAM} parallelepipeds and B_{TYE} beads is shown in Figure 6.4b.

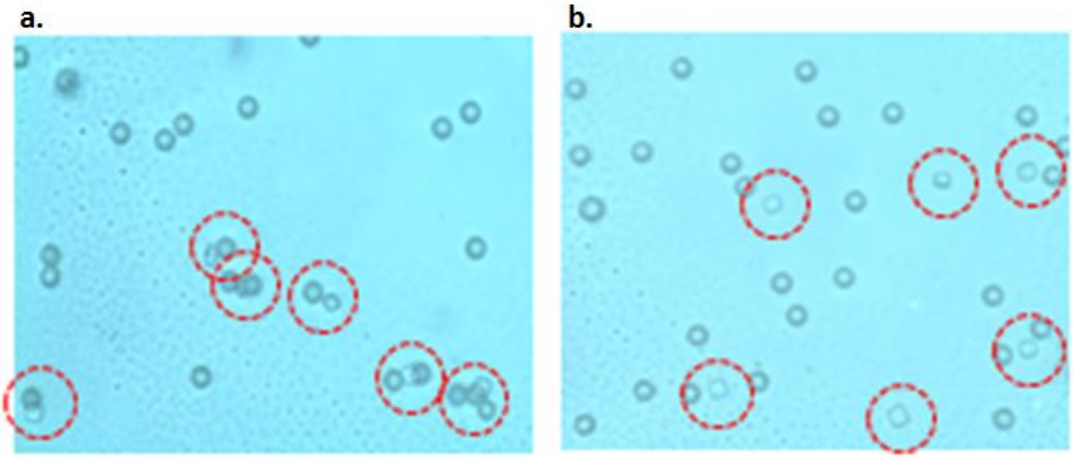

Figure 6.4. a. Cognate assembly and 5 x 5 x 2.5 µm PMMA-PFPMA parallelepipeds (A_{FAM}) and 6 µm polystyrene beads (A'_{TYE}), and b. non-cognate assembly of 5 x 5 x 2.5 µm PMMA-PFPMA parallelepipeds (A_{FAM}) and 6 µm polystyrene beads (B_{TYE}). The PMMA-PFPMA parallelepipeds are circled in red.

The cognate parallelepipeds and beads assembled together quite well. Analysis of 30 images taken resulted in a hybridization yield of roughly 40%, including a low percentage of negative hybridizations (bead-bead or parallelepiped-parallelepiped). In the non-cognate assembly, however, almost none of the particles hybridized together. This lack of hybridization for the non-cognate assembly demonstrates the selective nature of the DNA-facilitated binding. This shape-based methodology was very effective at qualitatively determining the hybridization, or lack of hybridization, for cognate and non-cognate particles with only the use of an optical microscope. However, because the particles were observed as sedimented at the bottom of a suspension, false associations are hard to distinguish and this cannot reliable be used for hybridization quantification.

6.3.3 Assembly verification by flow cytometry

Flow cytometry is a very powerful tool for characterizing cells and particles at with dimensions in the nanometer and micron regimes. The tool focuses the flow of

these objects into a very fine stream using a concentric sheath fluid in a capillary. The tool directs bright field light at the particles which scatter the light in different directions. (Figure) A forward scattering detector that is in line with the bright field source detects shallow-angle scattering which can be correlated to particle cross-sectional size. Another detector located perpendicular to the incident bright field source collects light which has been scattered at larger angles which can be correlated to the roughness or texture of the particle, as well as particle size. The cytometer is also equipped with multiple lasers which output incident light at specific wavelength bands to excite fluorophores on the particles which emit fluorescence signals that can be correlated to fluorescently-tagged DNA functionalization density.

To test the ability of single strands of complementary DNA to couple particles at high shear conditions, cognate and non-cognate sets of 1 μm and 10 μm carboxyl-functionalized polystyrene beads were mixed together for 30 seconds by vortexing and analyzed on a flow cytometer (FACSCalibur, BD Biosciences). These beads were functionalized for 2 hours in a reaction buffer consisting of 100 mM MES, 100 mM EDC, and 10 μM ssDNA. The 10 μm beads were functionalized with polyA30 ssDNA, and two sets of 1 μm beads were functionalized with either polyA30$_{HEX}$ or polyT30$_{HEX}$. First, the 1 μm and 10 μm beads were run separately on the cytometer to ensure that the different sizes could be differentiated by bright field light scattering. Figure 6.5a 6.5b are forward and side scattered signals for 10,000 events plotted against each other for the 1 μm and 10 μm beads, respectively. The 1 μm particle distribution (Fig. 6.5a) appears in the bottom left quadrant of the scatter plot with low forward and side scattering components. There is also a linear distribution along the forward scattering axis which corresponds to a significant amount of some contaminant in the system. This contaminant is visible in the bright field scattering plots for all 1 μm and 10 μm samples.

The 10 µm scattering plot (Fig. 6.5b) shows a large distribution at high forward scattering and side scattering values, which is easily differentiated from the 1 µm dataset. In Figure 6.5c, where cognate sets of 1 µm and 10 µm beads are mixed together, a small increase in both side scattering and forward scattering is seen, indicating that a significant amount of the 1 µm beads have coupled with the 10 µm beads, however there is still a significant signal representing unbound 1 µm particles in the lower left quadrant. In Figure 6.5d, a plot of a mixture of non-cognate 1 µm and 10 µm beads shows two distributions in locations similar to a combination of Figures 6.5a and 6.5b with no shift in the 10 µm bead-only distribution. The scattering plots of the cognate and non-cognate mixtures suggest that DNA-assisted aggregation is occurring, though the yield is less than complete.

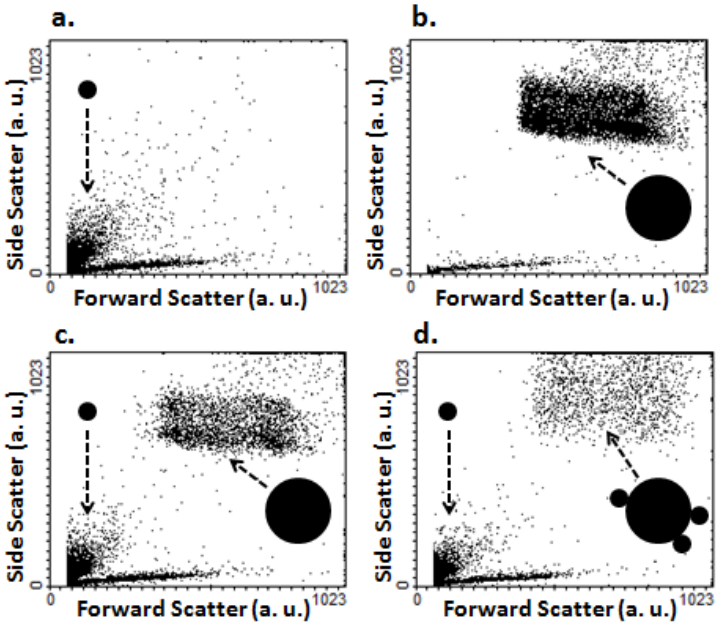

Figure 6.5. Bright field forward versus side scattering plots for a. 1 µm beads, b. 10 µm beads, c. a cognate mixture of 1 µm and 10 µm beads, and d. a non-cognate mixture of 1 µm and 10 µm beads.

This conclusion is further corroborated by fluorescence analysis of the beads. Fluorescence signal data for the same samples using a filter selected for the detection of light emitted from the HEX fluorophore were plotted versus side scattering data as shown in Figure 6.6. The 1 μm beads (Fig. 6.6a) had strong fluorescence signals and mostly low side scattering. This side scattering had a distribution including a few points at maximum values. This is can be attributed to non-selective aggregation of the 1 μm beads, or, more likely, due to multiple particles contributing to each side scattering signal due to the high concentration large concentration of 1 μm beads. The 10 μm beads (Fig. 6.6b) showed almost no fluorescence whatsoever. This result also suggests that the contamination particles seen near the x-axis of each plot in Figure 6.5 was not fluorescently-tagged ssDNA and was indeed contamination. The cognate mixture of the beads (Fig6.6c) showed a group of low side scattering and high fluorescence and a group of high scattering and high fluorescence, representing the unbound 1 μm fluorescent beads and 10 μm non-fluorescent beads bound to the 1 μm beads. Finally, Figure 6.6d is a plot of the non-cognate mixture, which contains the low side scattering 1 μm particles with high fluorescence, but surprisingly, the non-fluorescent 10 μm particles are visible at very low fluorescence (> 2 orders of magnitude lower than the 1 μm beads). This is attributed again to a weak fluorescence signal coming from neighboring 1 μm beads which are not bound to the 10 μm beads. A 3 orders of magnitude shift is seen between Figures 6.6c and 6.6d, which suggests that the 10 μm particles are coupling together.

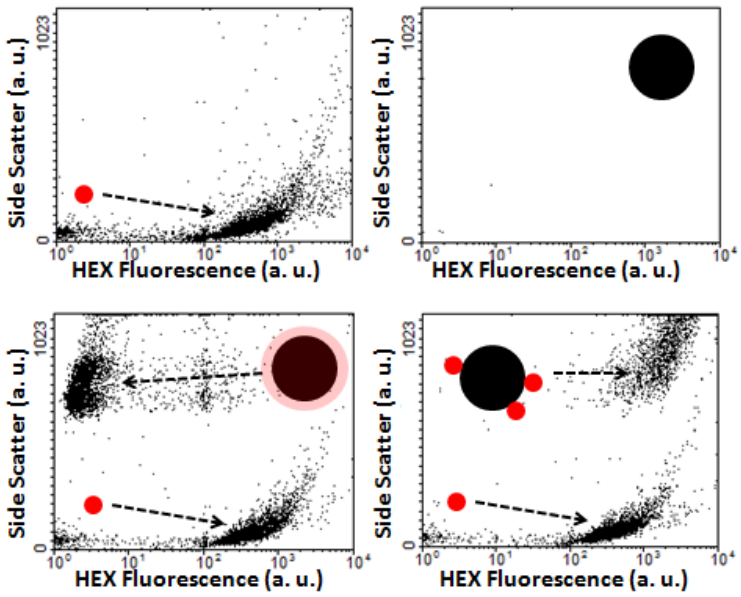

Figure 6.6. HEX fluorescence versus side scattering plots for a. 1 µm beads, b. 10 µm beads, c. a cognate mixture of 1 µm and 10 µm beads, and d. a non-cognate mixture of 1 µm and 10 µm beads.

Flow cytometry of cognate and non-cognate polystyrene beads proved to be a useful tool for characterizing self assembly in solution. However, the presence of contamination and weak fluorescence signal noise from neighboring fluorescent 1 µm particles made the data somewhat questionable since there is no way to actually image the contents of the flow cell for each data point.

6.3.4 Assembly verification by imaging flow cytometry: 5 x 5 x 2.5 µm PFPMA squares on PAA.

Imaging flow cytometry is a commonly-used technique in biology and biochemistry for characterizing cells whose contents are dyed with different fluorophores. This tool uses the same basic setup as the flow cytometer, but each time a bright field or fluorescence signal is taken for a particle event, this tool takes an image. To accomplish this, the imaging flow cytometer is equipped with a camera that can take

digital pictures of each event at a rate of several thousand per second. This technology was employed to characterize the fluorescence and size of self assembled copolymer particles, as well as to visualize the particles and aggregates in flowing in front of the light sources during detection in order to distinguish between particles which are bound together and particles which are only in each other's vicinity.

A film stack comprising 2.5 μm of PMMA-PFPMA was coated onto 200 nm of PAA and patterned into sets of 5 μm squares. Two sets of 5 μm squares were functionalized in situ for 12 hours with either A_{FAM} or A'_{TYE} cognate sequences using a reaction buffer containing 10 μM ssDNA, 100 mM EDC, and 100 mM pH 4.5 MES. After lifting the particles off the wafer chips in DI water for 30 minutes, two cognate particle solutions were produced having five out their six facets functionalized with ssDNA. These solutions were added together in a 1.24 : 1.00 ratio of A_{FAM} to A'_{TYE} and shaken on a vortex agitator for 30 seconds to achieve uniform mixing and coupling. The particles were quickly transferred to the imaging flow cytometer for hybridization analysis and a plot of FAM fluorescence intensity versus Tye665 fluorescence intensity for approximately 4,500 particles was generated as shown in Figure 6.7.

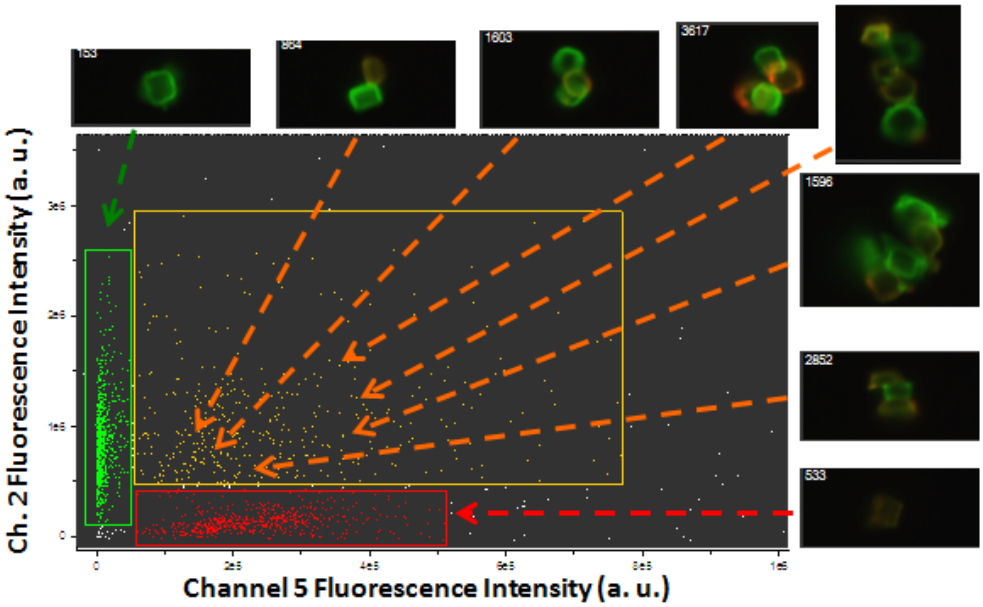

Figure 6.7. Plot of FAM fluorescence intensity versus Tye fluorescence intensity on a log-log scale for two sets of cognate 5 x 5 x 2.5 µm parallelepipeds including sample images.

The linear horizontal and vertical scatter groupings near the x and y axes were the unbound FAM or Tye665-labeled squares, and the scatter group between the linear groups represented the particles that were properly coupled together which contain both FAM and Tye665 fluorescence signals. Statistical analysis of the data showed that 30.2% of the particles were participating in hybridization. Inspection of the images that were taken for each particle or group of particles showed that there were several instances in which two or more particles were bound together. This suggests that the ssDNA functionalization is dense enough on the surfaces of these particles to hybridize multi-body aggregates which can withstand the high shear forces present in the imaging cytometer plumbing system, including a 250 µm constriction in the focusing capillary. Furthermore, the orientations of the particle couplings seem to be quite random. There were very few instances where the particles hybridized in a facet-to-facet configuration suggesting that the associations are irreversible in nature.

In many of the images, especially where multiple particles participated in hybridization, anon-uniformity was seen wherein the particles seemed to not have printed completely, leaving a resist footing profile. This non-uniformity is presumably residual PAA material that did not dissolved during the lift of step. This is corroborated by the fact that the footing region is brighter than the rest of the particle, most likely because pure MAA has a much higher density of carboxylate groups on its surface than the PMMA-PFPMA copolymer, leading to a denser functionalization of ssDNA.

In order to confirm the selectivity of these hybridizations, the 5 x 5 x 2.5 μm A'_{TYE} particles were mixed with 3 μm diameter polystyrene beads functionalized with cognate (A_{FAM}) and non-cognate (A'_{TYE}) ssDNA. These beads were carboxyl-modified polystyrene beads (PolySciences) that were reacted with ssDNA using the same reaction buffer as the PMMA-PFPMA particles; however the beads were reacted in solution under 1,200 RPM of agitation for 2 hours. Each mixture was vortexed for 30 seconds and placed immediately into the imaging cytometer for analysis. Figures 6.8 and 6.9 are fluorescence intensity plots for the cognate and non-cognate assemblies respectively. In the cognate bead-parallelepiped assembly, approximately 2,000 particles were analyzed on the tool at a ratio of 1.04 : 1.00 (beads to parallelepipeds). 49.7% of the particles participated in some sort of coupling. This is significantly higher than the cognate parallelepiped-parallelepiped assembly, presumably because the smaller 3 μm beads have increased mobility and are able to interact better with the parallelepipeds and the larger parallelepipeds are able to accommodate several dockings of the smaller beads. The region in the plot containing the hybridizations is actually segregated into defined subsections representing paralellepipeds which have bound with one, two, or three beads. To the upper right of those regions is more scattered data representing higher order aggregates which can involve multiple beads and multiple parallelepipeds.

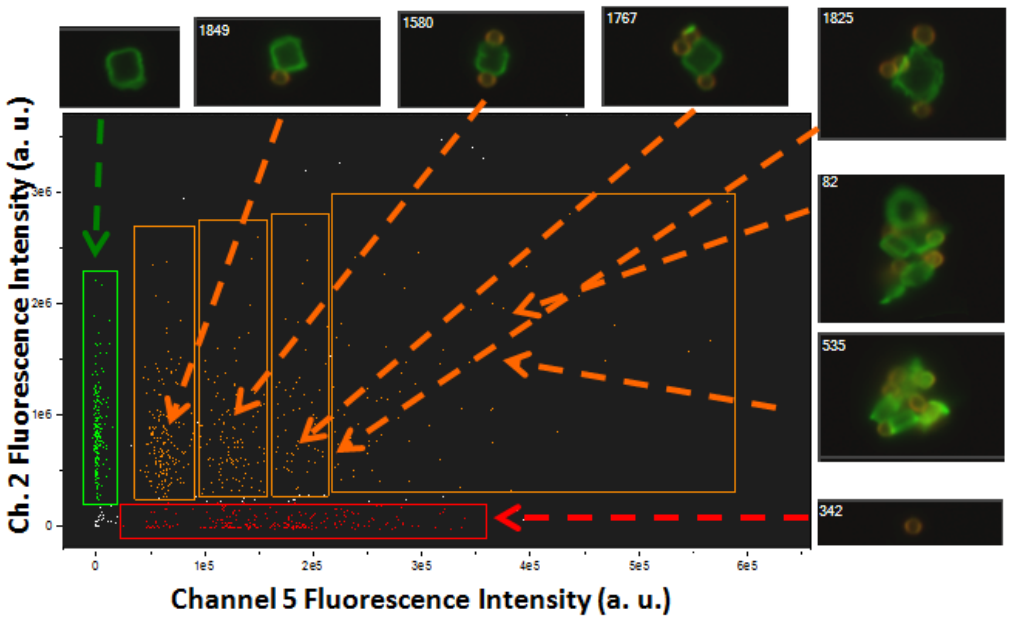

Figure 6.8 Plot of FAM fluorescence intensity versus Tye fluorescence intensity on a log-log scale for cognate 5 x 5 x 2.5 µm parallelepipeds (A_{FAM}) and 3 µm PS beads (A'_{TYE}) including sample images.

For the non-cognate assembly, Tye665 fluorescence was plotted versus forward scattering (size correlation) for an analysis of approximately 2,000 particles at a ratio of 1.18 : 1 (beads to parallelepipeds) as shown in Figure 6.8. The data was less clearly segregated because the same fluorophore was used for both sets of particles. However, inspection of the images determined that the long linear scatter region near the bottom of the plot comprised mostly beads and the large blot-shaped region above it comprised mostly parallelepipeds. The PMMA-PFPMA parallelepipeds had a higher forward scattering signal than the beads because they are larger in size than the 3 µm beads. In this assembly, only 2.7% of the particles present participated in some kind of assembly as observed in the images generated by the tool.

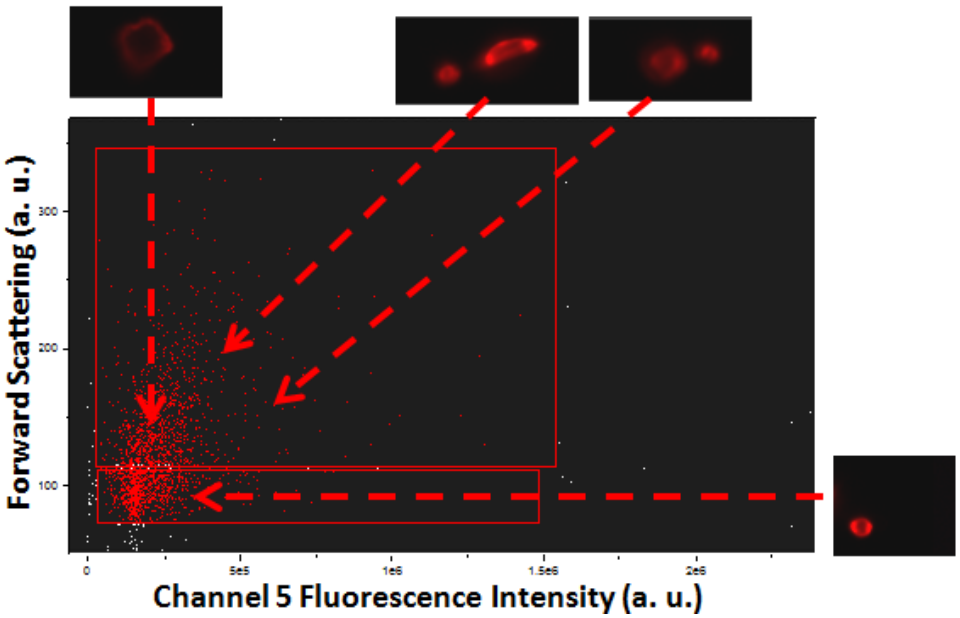

Figure 6.9 Plot of FAM fluorescence intensity versus Tye fluorescence intensity on a log-log scale for non-cognate 5 x 5 x 2.5 µm parallelepipeds (A'_{TYE}) and 3 µm PS beads (A'_{TYE}) including sample images.

These assemblies exhibited significant hybridization and good DNA-specific selectivity as evidenced by the statistical analysis of the particles summarized in Table 6.4.

Experiment	# Events Analyzed	Ratio of Mixed Particles	Assembly Yield
Cognate Parallelepipeds	2,000	1.08 : 1 (A_{FAM} parallelepipeds: A'_{TYE} parallelepipeds)	49.7%
Non-Cognate Parallelepipeds + Beads	2,000	1.14 : 1 (A'_{TYE} beads : A'_{TYE} parallelepipeds)	2.7%

Table 6.4. Summary of cognate and non-cognate particles assembled in solution and analyzed on an imaging flow cytometer using PAA lift-off layer.

At the time of the writing of this dissertation, this is the first demonstration of the selective self assembly of patternable ssDNA-conjugated polymer particles known by the author. However, these particles were fabricated using a lift-off layer (PAA) that is incapable of supporting a multi-functional particle processing scheme.

6.3.5 Assembly verification by imaging flow cytometry: 5 x 5 x 2.5 µm PFPMA squares on PMGI

After developing the PMGI LOL process to the point where it was capable of lifting off copolymer particles in an efficient and repeatable manner, a 2.5 µm PMMA-PFPMA film was coated on 200 nm of PMGI and sets of 5 x 5 µm squares were patterned. Sets of particles were functionalized in situ with A_{FAM}, A'_{TYE}, and B_{FAM} ssDNA and then lifted off using a 4 : 1 dilution of potassium borates in water (400k, Clariant). Cognate (A_{FAM} and A'_{TYE}) and non-cognate (A'_{TYE} and B_{FAM}) sets of these particles were mixed together, vortexed for 30 seconds, and introduced into the imaging flow cytometer for assembly analysis. The results of this assembly are displayed in Figures 6.10 and 6.11. The cognate mixture was an analysis if approximately 1,750 particles which had a 1.52 : 1.00 ratio of A'_{TYE} to A_{FAM} parallelepipeds, and 39.2% of the particles participated in binding. In addition the ratio of positive hybridizations to negative hybridizations was 67.2 to 1.0, meaning that a small amount of non-specific binding within each set of particles was present.

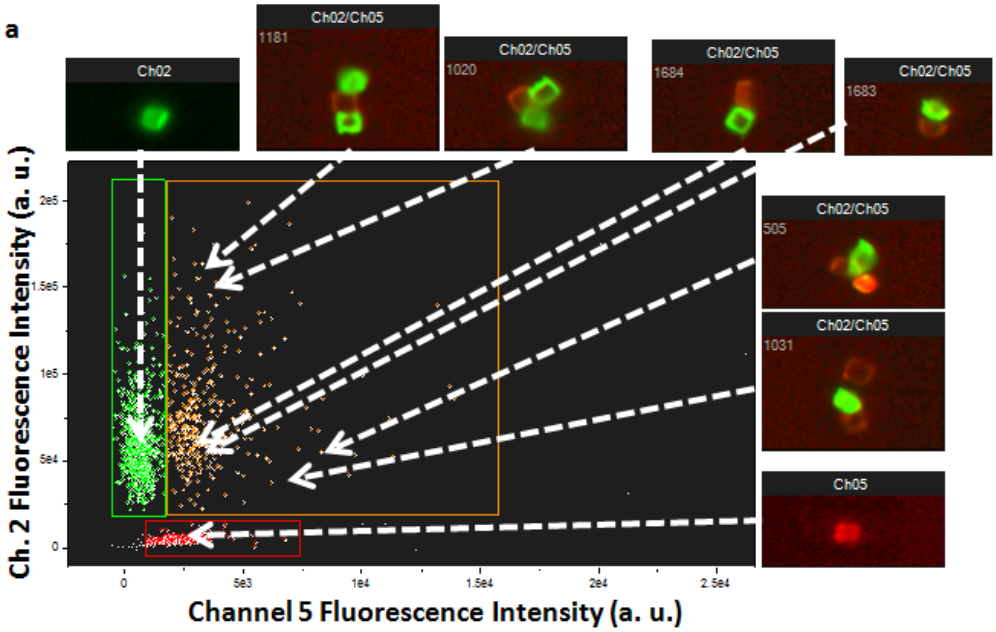

Figure 6.10. Plot of FAM fluorescence intensity versus Tye fluorescence intensity on a log-log scale for cognate 5 x 5 x 2.5 µm parallelepipeds (A_{FAM} and A'_{TYE}) including sample images.

For the non-cognate mixture case, approximately 1,750 particles were analyzed, which had a 1.50 : 1.00 ratio of A'_{TYE} to B_{FAM} parallelepipeds, and 0.5% of the particles participated in binding as shown in Figure 6.11. Of the particles which did hybridize (<10 couplings), the majority of the hybridizations were non-specific, which is a value that is on par with the non-specific binding present in the non-cognate case.

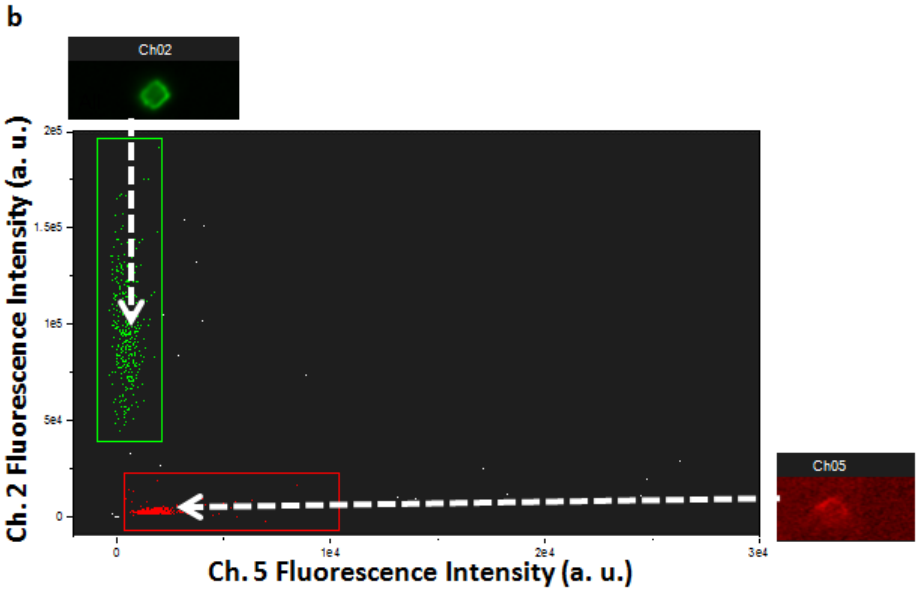

Figure 6.11. Plot of FAM fluorescence intensity versus Tye fluorescence intensity on a log-log scale for non-cognate 5 x 5 x 2.5 µm parallelepipeds (A'_{TYE} and A_{FAM}) including sample images.

Table 6.5 is a summary of the details of these assemblies, including the assembly yields and selectivity. The selectivity here is calculated as the ratio of positive hybridizations, hybridizations in which green fluorescent particles were bound to red fluorescent particles, to negative hybridizations, where red or green fluorescent particles were bound with themselves. Such negative hybridizations are expected at low levels due to the weak binding that is possible between non-cognate DNA strands. These associations could also represent situations where two particles were imaged at the exact moment when they happened to collide, even though there was no binding present.

Experiment	#Events Analyzed	Ratio of Mixed Particles	Assembly Yield	Selectivity
Cognate Parallelepipeds	1,750	1.52 : 1.00 (A_{FAM} parallelepipeds: A'_{TYE} parallelepipeds)	39.2%	67.2 : 1
Non-Cognate Parallelepipeds	1,750	1.50 : 1 (B_{FAM} parallelepipeds: A'_{TYE} parallelepipeds)	0.5%	N/A

Table 6.5. Summary of cognate and non-cognate parallelepipeds assembled in solution and analyzed on an imaging flow cytometer using a PMGI lift-off layer.

This data represents a successful verification of the selective self assembly of patterned copolymer particles at the unit micron scale. Because the PMGI LOL was employed for this assembly, the processing used to fabricate these functionalized particles is completely compatible with that of a protocol for producing polyfaceted particles with multiple independent functionalizations.

6.4 CONCLUSIONS

These experiments are the culmination of a large body of work focused on the development of several processing components with the purpose of enabling the DNA-facilitated self assembly of patternable poly-faceted shapes in solution. Several patternable acrylate-based materials were successfully patterned into polyfaceted three-dimensional shapes at the micron scale, some of which were capable of dimensions on the order of 2.5 μm. Single-stranded DNA was immobilized on the surfaces of polyfaceted particles and verified using multiple fluorescence detection methods. A lift-off layer was developed that was robust enough to last through several harsh processing steps, and which could be dissolved on demand for transfer of the particles into solution. Carboxyl-functionalized polystyrene beads were used as an analog vehicle to explore the

advantages and weaknesses of carbodiimide chemistry. Successful blocking of carboxylate groups on polystyrene was achieved and verified through hybridization testing. Finally, we used all of these techniques to generate particles capable of selectively self assembling into aggregates in solution.

The assembly of these particles was made possible by the application of various verification methodologies employing shape-based, polymer dying, and fluorescent tagging schemes. Optical and fluorescence microscopy were very helpful in superficially determining if any self assembly was taking place in solution. Unfortunately, these techniques were only able to be used for qualitative analysis. Flow cytometry, allowed for rapid quantification of potential self assembly of the particles. However, without information regarding the orientations and proximities of the particles, thorough characterization is not possible. Imaging flow cytometry is truly the most valuable analytical tool for the full characterization of DNA-facilitated particles self assembly. It affords quantitative analysis of the particle associations, determination of binding selectivity, and qualitative visual understanding of the assembled particles.

In the last section of the results, imaging flow cytometry analysis made it possible to see exactly what was occurring for each assembly. In the PMMA-PFPMA assembly in which the particles were lifted off using PAA resulting denser ssDNA functionalizations on some parts of the particles, larger assemblies were seen. This is presumably due to the particles having stronger hybridization binding at these regions, which is capable of withstanding higher shear forces. If all of the particle surfaces were more densely functionalized, it's possible that the aggregates would get so big that they would clog the tool, thus rendering analysis via cytometry useless. Clearly a balance between the hybridization-based associative forces and the shear forces exerted on the particles is necessary in order to view self assembly of these particles on a flow cytometer.

From the assembly images it was also evident that the particles are binding in seemingly random orientations, not in optimized facet-to-facet associations as in the polycarbonate tiles experiment. One would expect to see a high number of large aggregates present in cytometry images of particles where five out of the six sides are adequately functionalized with ssDNA. This was not the case, most likely because of the high shear forces in the capillary portion of the cytometer's flow cell. Larger aggregates were most likely present in the mixed solution before it was introduced into the cytometer, however the aggressive flow rates in the tool presented conditions which were incompatible with large, non-uniform assemblies. These particle associations are suggest an irreversible binding model wherein particles adjoin permanently upon collision. The advantage of this phenomenon is that it indicates that the hybridization-based binding is likely very strong.

If a suitable blocking scheme can be developed for acrylate-based reactive copolymers, then surely polyfaceted shapes can be generated with sides that are independently functionalized with different ssDNA. This would be very valuable for the field of self assembly because this photolithographic fabrication scheme has been developed such that it can be scaled down to the nanometer scale. The knowledge gained from these activities is certainly valuable for further work in DNA-facilitated self assembly of bulk particles. However, it is the hope of the author that parts of this work will inspire or be directly implementable in further research carried out by others in the field of self assembly as well as other fields.

6.5 FUTURE WORK

The assembly data in Chapter 6 is a demonstration of successful selective self assembly of patterned copolymer particles at the micron scale. The processing used to generate these particles was designed for the production of polyfaceted particles with multiple independent functionalizations for the purpose of three-dimensional assembly in solution. The only unit process that has not been fully-developed for this process is a comprehensive blocking step which would remove any double-functionalizations of ssDNA on the same facet. Although we have developed a surfactant-based blocking solution which worked well with micron-sized carboxyl-functionalized polystyrene beads which are very similar to the copolymer parallelepipeds, experiments have shown that this strategy, in its current form, was not a viable solution for the PMMA-PFPMA platform.

Further exploration of different species as covalent or adsorbed blocking agents is necessary to completely achieve independent functionalizations. A more rigorous study on the weak level of conjugation of species such as short-chain amines, short-sequence ssDNA, and surfactants may lead to improved chemistries for passivating residual active sites. It is also possible that large, negatively-charged ssDNA chains may, themselves be passivating the surface of the particles, and further exploration of this phenomenon could lead to ion-screening, ssDNA-denaturing, or some other technique that may allow for better coverage of the available active sites on the copolymer.

The self assembly of these particles would also benefit from research on how to introduce more reversibility into the particle associations so that more surface-bound ssDNA is hybridized and aligned facet-to-facet coupling is promoted. This increased reversibility would have to be balanced with some sort of technique for maintaining the stability of the aggregation during mixing. To increase reversibility of the binding, DNA

strand length could be reduced, the GC content of the strands could be minimized and the temperature of the particle solution at could be raised and slowly decreased back to room temperature similar to a polymerase chain reaction (PCR) process.

Finally, in order to avoid the need for a blocking step altogether, a processing scheme employing multiple photoresists could potentially be used to fabricate multi-faceted particles with independently functionalized facets. This would require the use of a photoresist which responds to 365 nm or higher light sources, but not to the DUV wavelengths to which our copolymer responds. In addition, the developer for the secondary photoresist must be compatible with the copolymer, the ssDNA surface functionalizations and the lift-off layer.

Chapter 7: High Throughput Sequencing of Antibodies with Paired Heavy and Light Chains

Reprinted in part with permission from DeKosky, B. J.; Ippolito, G. C.; Deschner, R. P.; Lavinder, J. J.; Wine, Y.; Rawlings, B. M.; Varadarajan, N.; Giesecke, C.; Dörner, T.; Andrews, S. F.; Wilson, P. C.; Hunicke-Smith, S. P.; Willson, C. G.; Ellington, A. D.; Georgiou, G. Nat. Biotechnol. ***2013****, 31, 166–169.*

7.1 INTRODUCTION

Antibodies are Y-shaped proteins produced by B lymphocytes (B cells) whose main function is to identify and neutralize foreign macromolecules present in the body.[1] These proteins are heavily studied by immunologists because they have the capability to immunize the body of specific antigens such as viruses, bacteria, chemicals and allergens. Antibodies are generally composed of two identical heavy chains and two light chains bound together by disulfide bonds as shown in Figure 7.1. Each heavy chain is composed of one variable polypeptide domain and three constant polypeptide domains, and each light chain is composed of one variable and one constant domain. At the ends of the heavy chain and light chain domains are antigen binding regions (F_{ab}) terminated by a paratope formed by the variable domains of the heavy and light chains, which is able to bind specific antigens. Three variable loops for each chain form this binding region.

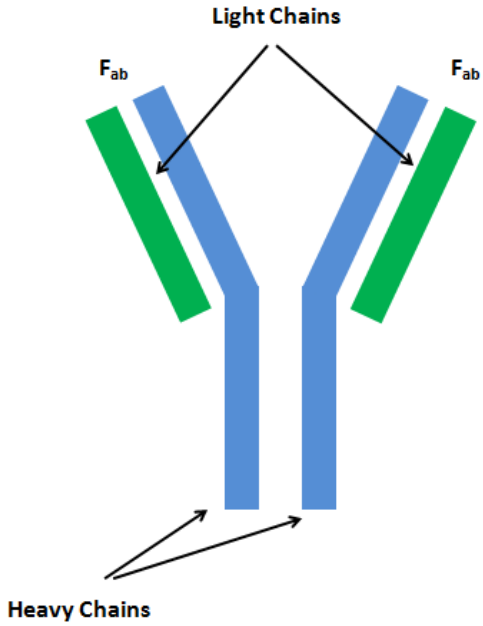

Figure 7.1. Antibody structure highlighting the heavy chains (blue), light chains (green), and the antigen binding areas (F_{ab}) .

It is the composition of these highly-diverse variable loops which determine an antibody's binding specificity for a particular antigen. Determining the composition of the variable areas of these antibodies and which antigens they bind with is the key to understanding human immune response. The ability to rapidly sequence large numbers of antibodies while retaining heavy and light chain pairing will certainly promote more efficient activities in the fields of antibody discovery, autoimmune research, vaccine development, and immunology research.

7.2 ANTIBODY SEQUENCING

Methods have been developed to accurately determine the genetic sequence of a particular antibody; however these processes are expensive and low-throughput. These techniques involve sequencing antibody-coding mRNA involve lysing B cells, isolating the mRNA, amplifying the mRNA sequence and converting it to cDNA via polymerase

chain reaction (PCR), and sequencing the result. This can be done accurately on small scales using 96-well PCR plates with individual wells for each B cell. Unfortunately, during B cell lysis information regarding the paring of the heavy and light chain variable regions (V_H and V_L) is lost. Large-scale, one-pot sequencing of V_H and V_L pairs is therefore not possible and must be done 96 wells at a time, creating a massive throughput bottleneck, and preventing a comprehensive analysis of entire human immune repertoires.

7.3 MICROWELL-BASED SEQUENCING PROCESS FLOW

The overall goal of this project was to develop a high-through methodology for sequencing heavy and light chain regions such that the pairing is retained. Lithographically-defined microwell arrays were chosen as the platform for isolating B cells during lysis because these wells can be printed cheaply and rapidly at micron-scale dimensions, allowing for hundreds of thousands of wells to be generated in an area the size of a microscope slide. This allows for high-throughput parallel processing of vast numbers of B cells in separate isolated vessels.

The original process flow for this project is summarized in Figure 7.2. First, antibody-containing B cells are harvested from the spleen of an animal, such as a mouse, which has been intravenously exposed to a particular antigen. These cells, which presumably contain high frequencies of antibodies created by the mouse's humoral immune system for the specific antigen, are loaded into the microwell array. The cells are then chemically lysed, and reagents for an overlap extension reverse transcript PCR (OE RT-PCR) process are added in. The OE RT-PCR technique[72] is designed to join together the heavy chain and light chain-specific mRNA using complementary sequence overlapping so that they can be reverse transcribed into cDNA for PCR amplification. A

glass slide is applied securely to the microwell chip to prevent cross-contamination of the contents of the different wells, and OE-RT-PCR is performed on the mRNA of each B cell independently. This PCR process serves to amplify the sequences as well as link the heavy and light chain sequence information for subsequent sequencing. The product is collected from the microwells and then transferred to a traditional 96-well plate with µL scale volumes for nested PCR. Finally, the end-product consisting of DNA sequences which contain both heavy and light chain components on the same strands are analyzed with a pyrosequencing technique.

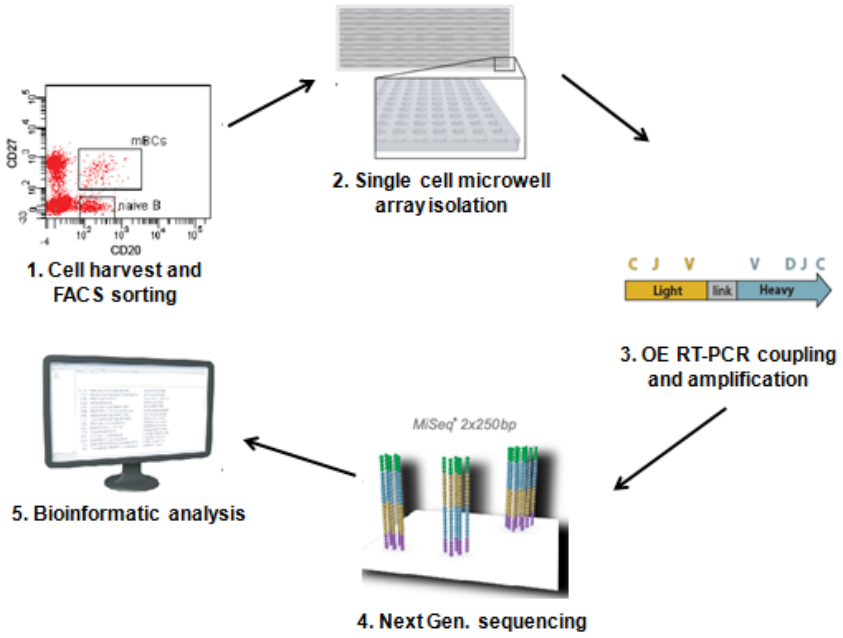

Figure 7.2. First generation microarray-based antibody sequencing process flow.

The fundamental technology which allows the mRNA of the antibodies of interest to be copied and purified is PCR. In this process, double strands of DNA are denatured (separated) at high temperature and then hybridized with small strands of primer DNA which are complementary to a few peptides on one end of each of the single strands of the DNA.[4] Next, DNA polymerase builds the primer into a fully-complementary DNA

using the deoxynucleoside triphosphate reagents in the solution. The target DNA and the newly-replicated DNA are then denatured, and the process is repeated several times to exponentially amplify the DNA of interest for improved detection.

RT-PCR is an alternate form of PCR which includes an extra reverse transcriptase step to convert mRNA to complementary DNA (cDNA), since PCR requires DNA templates. In order to characterize heavy and light chain pairing, the sequences for each one must be bound together on the same strand.[5] In order to achieve this, OE RT-PCR is employed, wherein the cDNA from the reverse transcriptase step is hybridized with primers that have extensions on them that do not hybridize with the cDNA, but do hybridize with each other. After the cDNA is denatured from its complement, the extensions from the heavy and light chain cDNA are hybridized, and further amplification can be done.

In addition, nested PCR can be done to purify the sample by isolating only the section of the DNA sequence desired. This is done by using primers that hybridize with the target DNA at some place on the strand which is not the end. This method will only replicate the DNA starting at the point where the primer was applied. This process does not need to be carried out in a microwell chip because the heavy and light chains have already been connected together in the OE RT-PCR step.

7.3 MICROWELL CHIP PLATFORM

7.3.1 Fabrication

The primary advantage us using of a microwell platform is that you can perform processing steps on large numbers of cells in parallel. Traditional PCR plates contain 96 separate tubes, whereas a microscope slide-sized chip can contain on the order of 10^5

microwells (Figure 7.3). The fabrication of arrays with such large numbers of wells was made possible by photolithography.

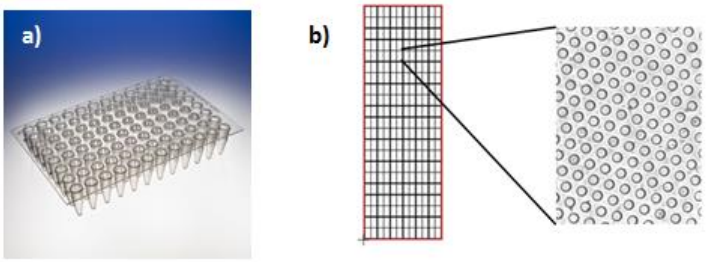

Figure 7.3. a) 96-well PCR tube array[7] and b) a single 120,376-well microchip array.

A silicone elastomer based on poly(dimethyl siloxane) (Sylgard 184, Fisher) was chosen as the array material because it is thermally-stable enough to withstand the temperature cycling of the PCR and it is flexible allowing it to be peeled from molded to and peeled from a photoresist pattern. The process flow for the fabrication of the silicone array consisted of first printing a pattern of cylinders and square posts into a photoresist, and then pouring the liquid silicone precursor onto the photoresist pattern to create a mold. The silicone precursor is then be thermally cured into a solid mold and subsequently peeled off of the substrate to yield arrays of wells.

A chrome-on-glass mask was designed with computer-aided design (CAD) software (L-edit) and acquired from a mask manufacturing company (Photronics). The 4 in x 4 in mask was designed with multiple sub-layouts with the same dimensions as a standard microscope slide (25 x 75 mm). Two slides were designed on the mask, one with large arrays of 37 µm-diameter circular features separated by 74 µm channels and another with 50 µm square features separated by 100 µm channels. These chips were designed with alphanumeric indexing to support orientation at high magnification on an optical microscope. Once the mask was acquired, a 50 µm film of negative photoresist[73]

(SU-8, MicroChem) was spin-coated onto a silicon wafer and cured on a hot plate (30 min at 95 °C). Contact lithograpy using an i-line (365 nm) light source was used to pattern the mask features into the photoresist, followed by a post-exposure bake step on a hot plate (10 min at 95 °C) and a 5 min soak in PGMEA developer. In the next step, of a 9 : 1 ratio of silicone elastomer base to initiator was mixed in a petri dish and placed in a vacuum oven for degassing to remove bubbles created during the mixing process. Next, the silicone precursor was poured onto the patterned photoresist[74] and baked at 150 °C for 10 min. The solidified PDMS was then carefully peeled off to yield a durable and flexible chip ready for PCR.[6]

7.3.2 Silicone Curing Optimization

After preparing several molds, it was found that the silicone slides would sometimes stick to the photoresist pattern, resulting in catastrophic tearing of the slides during peeling and a substrate which was unusable for subsequent molds. A curing optimization study was performed by testing the peeling process at a range of temperatures from 100 °C to 200 °C and a range of bake times from 5 minutes to 30 minutes. It was found that below 115 °C, the silicone was not fully cured and the slides would easily stretch and tear upon removal. At temperatures above 130 °C (and for longer curing times), the film was strong enough to be peeled off the substrate, but sharp tearing was experienced, usually near the center of the wafer. This phenomenon was attributed to the film shrinking at higher temperatures during crosslinking, imparting stress on the photoresist posts and creating unwanted adhesion.[75] A baking step at 120 °C for 20 minutes yielded the easiest peeling and allowed the photoresist template to be reused more than 20 times. This greatly reduced the number of photoresist templates

necessary to create silicone slides for this project. In order to ensure that the silicone slides were highly crosslinked and robust enough for processing, they were baked at 150 °C for 20 minutes after peeling.

7.3.3 Well Filling

After curing the slides, the surface of the printed silicone was very hydrophobic, making the filling of the wells with aqueous solution problematic. This problem was circumvented by exposing the silicone slide to an oxygen plasma etch process (PDC-32G, Harrick Plasma) for 5 minutes to form hydroxyl groups at the surface. Goniometry was performed on a droplet of water on the silicone surface as shown in Figure 7.4. A significant decrease in the contact angle of the water droplet from 110.7° to 71.3° is clearly seen after the 5 minute etch step.

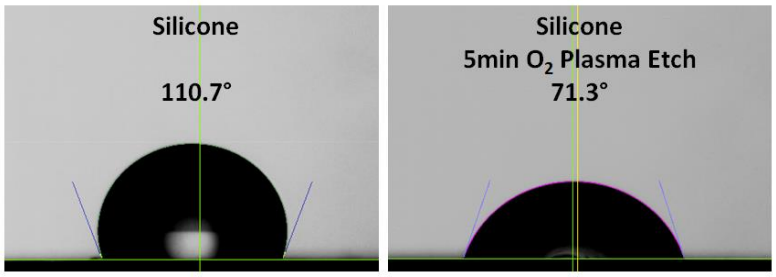

Figure 7.4. A droplet of water on the silicone slide a. before and b. after a 5 min oxygen plasma etch denoted with corresponding contact angle measurements taken on a goniometer.

Filling the wells with the B cells is a critical step in the process because depositing more than one cell can lead to H/L chain pairing mismatch errors. However, it is also desirable to fill as many wells as possible to improve throughput. Initially, cells were introduced into the wells by dispensing a concentrated solution of cells onto the

silicone slide and aspirating and redispensing the solution multiple times with 5 minute pauses in between for sedimentation. This process was effective at filling the wells at yields of up to 50% depending on how many cycles were performed. Unfortunately, wells with more than one cell were common. For a 50% yield deposition of B cells on square the square microwells, approximately 5% of the wells contained double loadings as shown in Figure 7.5.

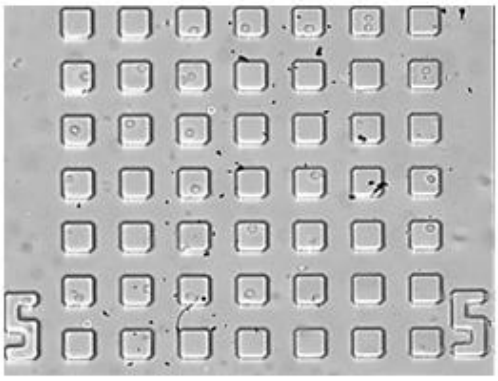

Figure 7.5. Optical microscope images of cells deposited into square PDMS wells with a yield of approximately 50%.

A drag-a-drop process[76] similar to one used in the microelectronics industry for immersion lithography in which a large droplet of cell solution was drug across the surface of the microwell array was also performed in order to maximize loading. This technique makes use of capillary force assembly to direct cells into the wells by drawing the air water contact interface across the surface of the arrays similar to convective used by Broguière et al to deposit vesicles into molded PDMS wells[77] as shown in Figure 7.6.

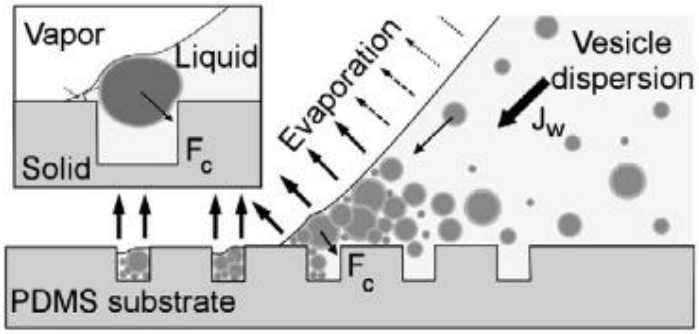

Figure 7.6. Convective capillary force assembly of vesicles into wells on a PDMS substrate. Reprinted with permission from [77]

In order to employ the drag-a-drop technique, the droplet must be sandwiched between a hydrophilic and a hydrophobic surface. A microtextured polyethylene scintillation vial lid was used as the hydrophilic surface, which pulled the cell solution droplet across the more hydrophobic silicone surface. This method was very effective for experiments even when the silicone slide was treated with oxygen plasma etch, delivering yields on the order of 90% very quickly. However, after treating the slides with bovine serum albumin (BSA) to inhibit the binding of the lysate to the microwell array surfaces, this method became impossible because the cell solution wetted the surface of the array very well (Fig. 7.7), preventing dragging.

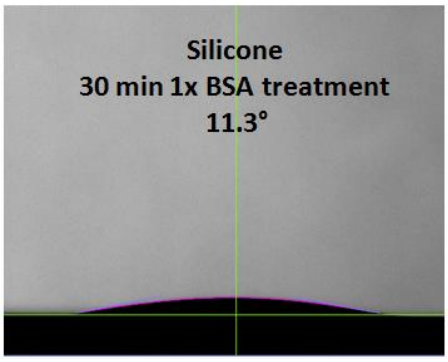

Figure 7.7. A droplet of water on the silicone slide after a 30 min 1x BSA treatment denoted with corresponding contact angle measurement.

To minimize the number of wells with multiple cells in them, a dilute solution was spread over the surface of the silicone slide such that only 10% of the wells were filled. At this well-filling yield, the percentage of wells with more than one cell in them is less than 1%. This was deemed to be acceptable for the cell isolation process and was used henceforth. Figure 7.8 is an example of a circular well array filled with cells using this loading technique.

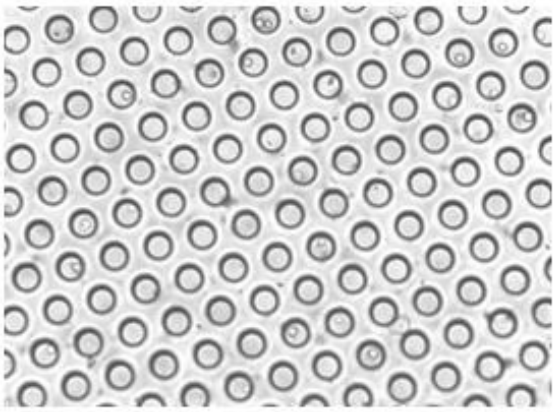

Figure 7.8. Optical microscope images of cells deposited into the circular silicone wells at approximately a 10% loading yield.

The arrays of microwells are bordered by channels that span the width and length of the chip so that when the glass slide is applied to them for sealing purposes, they can direct the excess liquid out of the chip. It was also noticed during the filling process that cells were depositing into the channels as in Figure 7.9a. A rinsing process was attempted to try to remove the cells from the channels without removing the cells out of the wells, but the rinse processes were either ineffective or too aggressive, resulting in unintentional lysis as shown in Figure 7.9b. An additional slide layout with a range of channel sizes was designed and printed in order to resolve the issue; however, even at very large channel widths (500 μm) lysis was still seen.

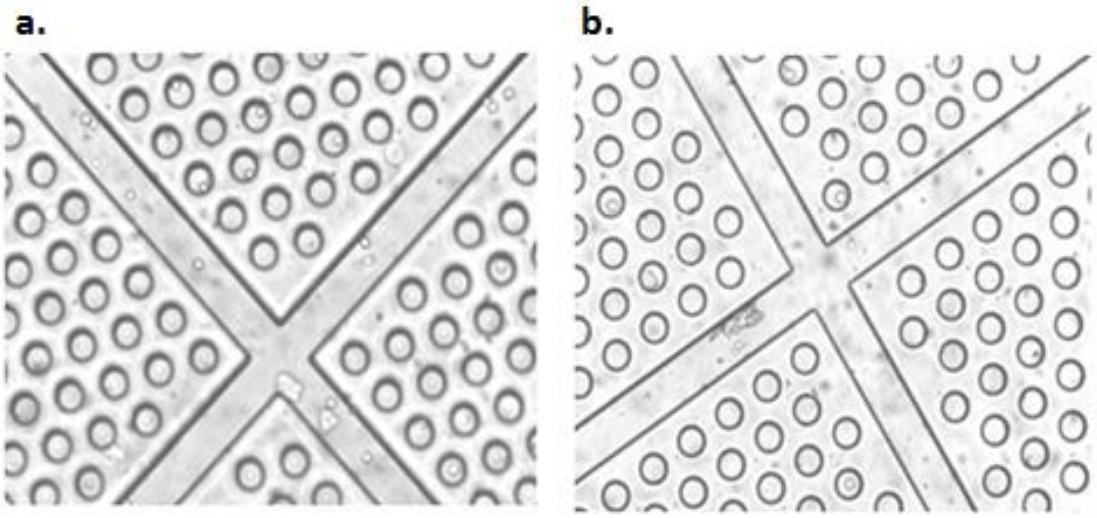

Figure 7.9. Optical microscope images of cells deposited into the circular PDMS wells and channels a. before and b. after rinsing.

7.3.4 Overlap Extension RT-PCR Using the Microwell Arrays

Despite the cells in the channels, the PCR technique was carried out on the chip, but after only three or four PCR cycles the silicone microwells completely dried out. This was assumed to be due to the poor seal between the glass and the PDMS chip (Figure 7.10a). Several stop-gap solutions to this problem were studied such as lining the edge of the chip with oil or adding extra water mid-cycle to further humidify the chamber, but these solutions failed. After observing the PCR tool during operation a few times, it was noticed that condensation was developing on the underside of the top of the lid. In order to stop the condensation, the poorly-insulated lid was then modified to include two solid-state heating ribbons connected to a variable autotransformer as shown in Figures 7.10b and 7.10c.

Figure 7.10. Images of a. the poorly-sealed microwell chip loaded into PCR b. the modified PCR lid and c. the custom temperature feedback system.

In addition, a thermocouple probe was taped to the underside of the lid to create a feedback look for the heating system. This not only allowed the lid to be heated to avoid the condensation, but the temperature could now be matched to that of the PCR unit via the thermocouple feedback to avoid further thermal issues. The PCR process was then reattempted and the unit achieved the required 35 cycles without drying out any microwells. Afterwards, nested PCR was done on the product of the OE RT-PCR process that was performed on the cells while in the chip. After several attempts, the nested PCR process did not yield distinct signatures in the base pair ranges that were expected. This was attributed to significant cross-contamination of the well contents during the PCR cycling due to the microwells not being completely isolated from each other.

7.3.5 Emulsion PCR method

As an alternative, an emulsion technique[78] in conjunction with polyT-conjugated magnetic particles was explored. In this system, magnetic beads conjugated with 12-mer strands of polythymidine were hybridized to the polyadenosine end of the mRNA of the heavy and light chains.[8,9] This step was performed in the wells after covering them with a membrane which was permeable to the lysis and bind buffer components, but not to the

mRNA. The magnetic beads loaded with the two sets of mRNA were then emulsified and placed in standard tubes for OE RT-PCR. The product mRNA was removed from the emulsion by liquid-liquid extraction and nested PCR was performed; again in standard tubes.

Gel electrophoresis was run on cells processed with the microwell-only OE RT-PCR technique as well as the microwell and emulsion OE RT-PCR technique. Only two different cell lines were used for this analysis for simplicity: MOPC 21 and MOPC 315 mouse plasmacytoma B cells. The results from these samples along with a base pair sizing ladder are shown in Figure 7.11a. It is evident from the gel that only two distinct bands are visible for the emulsion technique, whereas for the conventional PCR technique, multiple bands are present corresponding to the cross-contamination of the two sets of heavy and light chains. Figure 7.11b outlines the expected band sizes, in base pairs, for the conventional tube PCR. The numbers highlighted in green represent the band sizes that should be produced if the H/L pairing is retained. These results confirm that the emulsion technique is capable of preserving the H/L pairing, whereas the microwell-only OE RT-PCR method failed.

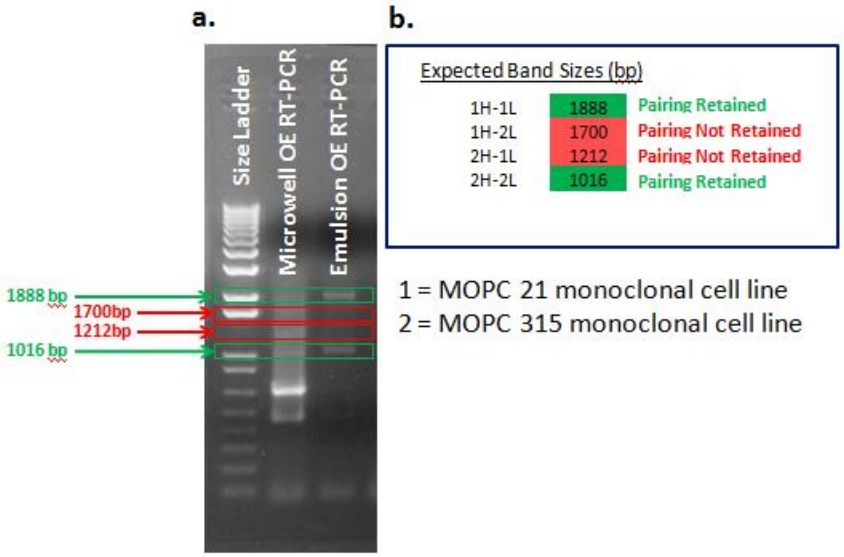

Figure 7.11. a) Gel electrophoresis results for the pairing and PCR amplification of MOPC 21 and MOPC 315 monoclonal cell lines using the microwell-only technique and the emulsion technique, and b) the expected band sizes for retained and non-retained pairing.

The results of this experiment led to the abandonment of the microwell-only strategy for a methodology for a hybrid process combining the microwell-based magnetic bead linking of the mRNA followed by emulsion OE RT-PCR. The standard process flow was modified to include the emulsion-based PCR as shown in Figure 7.12.

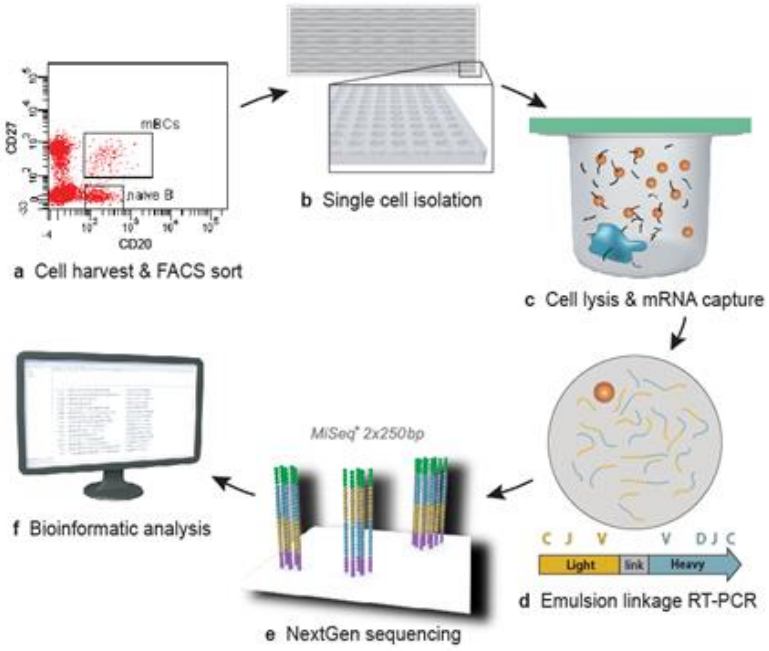

Figure 7.12. Second generation antibody sequencing process flow modified with an emulsion RT-PCR step. Reprinted with permission from [45].

7.4 SEQUENCING OF HUMAN B CELLS WITH RETAINED V_H/V_L PAIRING.

This new process flow was used to analyze the V_H/V_L repertoire of three different human B cell populations. The first experiment used 61,000 IgG^+ B cells from a healthy human blood spiked with immortalized lymphoblast cells (IM-9) which express known sequences of V_H and V_L pairings used as a control. Next, human plasmablasts ($CD19^+CD3^-CD14^-CD38^{++}CD27^{++}CD20^-$) from a healthy individual seven days after being immunized with tetanus toxoid were sorted for surface antigen binding. Approximately 400 plasmablasts were then spiked with the immortalized cell line (ARH-77) as a control. Finally, memory B cells ($CD19^-CD3^-CD27^+CD38^{int}$) were collected from a healthy human individual fourteen days after vaccination with the FluVirin influenza vaccine (2010-2011) and spiked with IM-9 as a control. Two samples were

taken from these cells for sequencing analysis using the microwell-based high-throughput sequencing process (168 cells) and the standard 96-well plate sequencing process as a comparison (8,000 cells, spiked with IM-9).

The heavy and light chain pairs from the complementarity determining region 3 (CDR-3) of the antibodies were analyzed and plotted on heat maps of heavy chain versus light chain gene family components as shown in Figure 7.13. The columns correspond to the heavy chains in the IGHV gene family and the rows correspond to the light chains in the IGLV and IGKV gene families. The legend indicates the relative percentage of pairings found in each gene family combination.

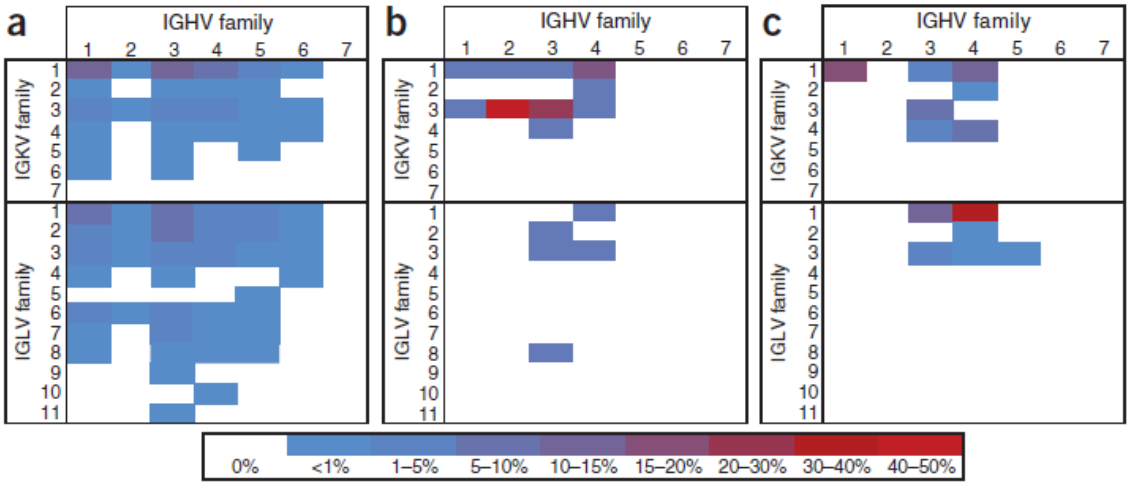

Figure 7.13. Heat maps of the CDR-3 antibody region plotted with respect to the corresponding heavy and light chain gene families for a. the healthy donor IgG^+ B cells, b. the tetanus toxoid-specific plasmablasts, and c. the influenza immunized memory B cells. *Reprinted with permission from*[45]

The first experiment using the IgG^+ B cells yielded 2,716 unique V_H/V_L pairs as shown in Figure 7.14a. The heavy pairs were found to be paired with the proper light chain at a ratio of 78 : 1 compared to background. Some of the pairings shown in this

heat map are for gene families known to be found at lower frequencies. This demonstrates that this technique is capable of analyzing pairings that are more rare as well as those that are present in larger numbers. The second experiment using the tetanus toxoid plasmablasts yielded 86 unique V_H/V_L pairs (Fig. 7.14b) and exhibited a very high known pairing accuracy ratio of 650 : 1. The third experiment for the influenza immunization yielded 240 unique V_H/V_L pairs with a very high known pairing accuracy ratio of 942 : 1 (Fig. 7.14c). A blinded analysis of the pairings generated from the microwell-based technique and the 96-well plate technique showed that the results for the two sets were in complete agreement.

These experiments display the ability of microwell-based antibody sequencing to generate correctly paired gene family sequences with high accuracy. In the first experiment very high numbers (61,000) of cells were analyzed in parallel, demonstrating the power of this high-throughput process. The reported accuracy ratios for each experiment were also very promising. A process that can analyze these large volumes of cells with such high accuracy is a very large step toward the possibility of generating a heat map for the entire human immune repertoire in a tractable time scale.

7.5 Conclusions and Future Work

A microwell-based platform was developed as method for isolating B cells and extracting genetic sequences coding for the variable regions of mammalian antibodies as part of a process flow designed to analyze V_H/V_L pairing repertoires. While the initial process involving complete isolation, mRNA extraction, pairing, and amplification in the microwells was unsuccessful, a second generation process flow proved to be functional. A microwell fabrication process using a silicone mold formed using a photoresist

template patterned by contact lithography was successfully developed. Several studies were performed to optimize the loading of the cells into the microarray by modifying the silicone surface and controlling the deposition of cells into the wells. The modified version of the process flow incorporating a magnetic bead coupling process and emulsion-based PCR amplification was used to analyze three large samples from spiked human cells with high accuracy. This system is a relatively inexpensive, rapid, and high-throughput method for isolating and amplifying the identifying mRNA structure for vast numbers of antibodies, while still fully retaining information on H/L pairing.

This technology has the potential to be used for a large range of applications which, until now, have been constrained by low-throughput processes which preserve heavy and light chain pairing. This method can be used to quickly and efficiently identify antibodies for specific antigens, which can then be replicated and used in vaccines. It can also be used to analyze the performance of vaccines and drugs in development. It can also be used in autoimmune research, which currently is primarily restricted to monoclonal cell lines. Furthermore, it can be used in diagnostics as a method for analyzing the health and response of human immune systems with quick turn-around-time.

Despite the early success of this methodology, it would benefit from further development of the cell deposition process into the wells. A loading strategy wherein the cells are deposited with limited or no double-loading of the wells needs to be devised. Initial designs for a new mask have been laid out in which new, more complex shapes can be printed in to the arrays which minimize the risk of loading multiple cells in the same well. This design uses a smaller circular well with a diameter that is slightly less than two B cell diameters surrounded by short, thin channels which are too small for cell loading. These plus-sign-shaped channels will prevent secondary cell loading, but still

give the well enough volume to accommodate proper cell lysis and mRNA extraction using the magnetic beads. This design would facilitate higher loading yield without the large increase in double-loading of the wells.

Several other experimental activities are currently underway which make use of microwell-based high-throughput sequencing. Recent work by Dr. Christien Kluwe has resulted in the successful discovery of a next-generation improved antibody for Zaire Ebolavirus. In addition, sequencing analysis is also being carried out by other researchers using this technology to discover new antibodies for the Machupo virus and severe acute respiratory syndrome. With the increased danger of worldwide epidemics of such diseases as swine flu, avian flu and SARS due to increased global travel and the prospect of biological terrorism, this technology has great potential to benefit the quality of life for human beings.

Biblography

(1) Whitesides, G. M.; Grzybowski, B. *Science* **2002**, *295*, 2418–2421.
(2) Lin, A.; Meyers, M. A. *Mater. Sci. Eng. A* **2005**, *390*, 27–41.
(3) Monnard, P.-A.; Deamer, D. W. *Anat. Rec.* **2002**, *268*, 196–207.
(4) Dixon, N. E. *Nature* **2009**, *462*, 854–855.
(5) Noll, M. *Nature* **1974**, *251*, 249–251.
(6) Zhang, S.; Marini, D. M.; Hwang, W.; Santoso, S. *Curr. Opin. Chem. Biol.* **2002**, *6*, 865–871.
(7) Donlin, M. J.; Patel, S. S.; Johnson, K. A. *Biochemistry (Mosc.)* **1991**, *30*, 538–546.
(8) Hua, F.; Sun, Y.; Gaur, A.; Meitl, M. A.; Bilhaut, L.; Rotkina, L.; Wang, J.; Geil, P.; Shim, M.; Rogers, J. A.; Shim, A. *Nano Lett.* **2004**, *4*, 2467–2471.
(9) Eigler, D. M.; Schweizer, E. K. *Nature* **1990**, *344*, 524–526.
(10) Bailey, T.; Choi, B. J.; Colburn, M.; Meissl, M.; Shaya, S.; Ekerdt, J. G.; Sreenivasan, S. V.; Willson, C. G. *J. Vac. Sci. Technol. B* **2000**, *18*, 3572–3577.
(11) Xia, Y.; Mrksich, M.; Kim, E.; Whitesides, G. M. *J. Am. Chem. Soc.* **1995**, *117*, 9576–9577.
(12) Bates, F. S.; Fredrickson, G. H. *Phys. Today* **1999**, *52*, 32.
(13) Cushen, J. D.; Bates, C. M.; Rausch, E. L.; Dean, L. M.; Zhou, S. X.; Willson, C. G.; Ellison, C. J. *Macromolecules* **2012**, *45*, 8722–8728.
(14) Bates, C. M.; Seshimo, T.; Maher, M. J.; Durand, W. J.; Cushen, J. D.; Dean, L. M.; Blachut, G.; Ellison, C. J.; Willson, C. G. *Science* **2012**, *338*, 775–779.
(15) Botiz, I.; Darling, S. B. *Mater. Today* **2010**, *13*, 42–51.
(16) Ruiz, R.; Ruiz, N.; Zhang, Y.; Sandstrom, R. L.; Black, C. T. *Adv. Mater.* **2007**, *19*, 2157–2162.
(17) Xiao, S.; Yang, X.; Edwards, E. W.; La, Y.-H.; Nealey, P. F. *Nanotechnology* **2005**, *16*, S324.
(18) Antonietti, M.; Förster, S. *Adv. Mater.* **2003**, *15*, 1323–1333.
(19) Edwards, K. A.; Baeumner, A. J. *Anal. Bioanal. Chem.* **2006**, *386*, 1613–1623.
(20) Sofou, S.; Sgouros, G. *Expert Opin. Drug Deliv.* **2008**, *5*, 189–204.
(21) Vamvakaki, V.; Chaniotakis, N. A. *Biosens. Bioelectron.* **2007**, *22*, 2848–2853.
(22) Edwards, K. A.; Curtis, K. L.; Sailor, J. L.; Baeumner, A. J. *Anal. Bioanal. Chem.* **2008**, *391*, 1689–1702.
(23) Bäumner, A. J.; Kummer, T.; Schmid, R. D. *Anal. Lett.* **1996**, *29*, 2601–2613.
(24) Duan, H.; Berggren, K. K. *Nano Lett.* **2010**, *10*, 3710–3716.
(25) Bowden, N.; Arias, F.; Deng, T.; Whitesides, G. M. *Langmuir* **2001**, *17*, 1757–1765.
(26) Cordeiro, J.; Lecarme, O.; Dias, G. O.; Peyrade, D. *J. Vac. Sci. Technol. B Microelectron. Nanometer Struct.* **2012**, *30*, 06F203.
(27) Meiring, J. E.; Grayson, S. M.; Lee, S.; Costner, E. A.; Schmid, M. J.; Michaelson, T. B.; Willson, C. G. *Opt. Eng.* **2009**, *48*, 037201–037201–14.
(28) Seeman, N. C.; Kallenbach, N. R. *Biophys. J.* **1983**, *44*, 201–209.
(29) Seeman, N. C. *J. Theor. Biol.* **1982**, *99*, 237–247.
(30) Seeman, N. C. *Nature* **2003**, *421*, 427–431.

(31) Li, X.; Yang, X.; Qi, J.; Seeman, N. C. *J. Am. Chem. Soc.* **1996**, *118*, 6131–6140.
(32) Rothemund, P. W. K. *Nature* **2006**, *440*, 297–302.
(33) Gu, H.; Chao, J.; Xiao, S.-J.; Seeman, N. C. *Nature* **2010**, *465*, 202–205.
(34) Turkevich, J.; Stevenson, P. C.; Hillier, J. *Discuss. Faraday Soc.* **1951**, *11*, 55–75.
(35) Mirkin, C. A.; Letsinger, R. L.; Mucic, R. C.; Storhoff, J. J. *Nature* **1996**, *382*, 607–609.
(36) Alivisatos, A. P.; Johnsson, K. P.; Peng, X.; Wilson, T. E.; Loweth, C. J.; Bruchez, M. P.; Schultz, P. G. *Nature* **1996**, *382*, 609–611.
(37) Kim, J.-W.; Kim, J.-H.; Deaton, R. *Angew. Chem. Int. Ed.* **2011**, *50*, 9185–9190.
(38) Cao, Y. C.; Jin, R.; Mirkin, C. A. *Science* **2002**, *297*, 1536 –1540.
(39) Rosi, N. L.; Giljohann, D. A.; Thaxton, C. S.; Lytton-Jean, A. K. R.; Han, M. S.; Mirkin, C. A. *Science* **2006**, *312*, 1027–1030.
(40) Hurst, S. J.; Lytton-Jean, A. K. R.; Mirkin, C. A. *Anal. Chem.* **2006**, *78*, 8313–8318.
(41) Thaxton, C. S.; Elghanian, R.; Thomas, A. D.; Stoeva, S. I.; Lee, J.-S.; Smith, N. D.; Schaeffer, A. J.; Klocker, H.; Horninger, W.; Bartsch, G.; Mirkin, C. A. *Proc. Natl. Acad. Sci.* **2009**, *106*, 18437–18442.
(42) Kinoshita, T.; Seino, S.; Otome, Y.; Mizukoshi, Y.; Nakagawa, T.; Nakayama, T.; Sekino, T.; Niihara, K.; Yamamoto, T. A. *MRS Online Proc. Libr.* **2005**, *877*, null–null.
(43) Willner, I.; Cheglakov, Z.; Weizmann, Y.; Sharon, E. *The Analyst* **2008**, *133*, 923.
(44) Inomata, Y.; Wada, T.; Handa, H.; Fujimoto, K.; Kawaguchi, H. *J. Biomater. Sci. Polym. Ed.* **1994**, *5*, 293–302.
(45) DeKosky, B. J.; Ippolito, G. C.; Deschner, R. P.; Lavinder, J. J.; Wine, Y.; Rawlings, B. M.; Varadarajan, N.; Giesecke, C.; Dörner, T.; Andrews, S. F.; Wilson, P. C.; Hunicke-Smith, S. P.; Willson, C. G.; Ellington, A. D.; Georgiou, G. *Nat. Biotechnol.* **2013**, *31*, 166–169.
(46) Qi, H.; Ghodousi, M.; Du, Y.; Grun, C.; Bae, H.; Yin, P.; Khademhosseini, A. *Nat. Commun.* **2013**, *4*.
(47) Lämmerhardt, N.; Merzsch, S.; Ledig, J.; Bora, A.; Waag, A.; Tornow, M.; Mischnick, P. *Langmuir* **2013**, *29*, 8410–8416.
(48) Nie, Z.; Li, W.; Seo, M.; Xu, S.; Kumacheva, E. *J. Am. Chem. Soc.* **2006**, *128*, 9408–9412.
(49) Suzuki, D.; Kawaguchi, H. *Colloid Polym. Sci.* **2006**, *284*, 1471–1476.
(50) Calcagno, L.; Compagnini, G.; Foti, G. *Nucl. Instrum. Methods Phys. Res. Sect. B Beam Interact. Mater. At.* **1992**, *65*, 413–422.
(51) Iwakura, Y.; Kurosaki, T.; Ariga, N.; Ito, T. *Makromol. Chem.* **1966**, *97*, 128–138.
(52) Sagara, K.; Kim, S. W. *J. Controlled Release* **2002**, *79*, 271–281.
(53) Francesch, L.; Borros, S.; Knoll, W.; Förch, R. *Langmuir* **2007**, *23*, 3927–3931.
(54) Lowe, A. B. *Polym. Chem.* **2010**, *1*, 17–36.
(55) Sumerlin, B. S.; Tsarevsky, N. V.; Louche, G.; Lee, R. Y.; Matyjaszewski, K. *Macromolecules* **2005**, *38*, 7540–7545.
(56) Greeneich, J. S. *J. Electrochem. Soc.* **1975**, *122*, 970–976.
(57) Lee, E.; Hahn, J. W. *J. Appl. Phys.* **2008**, *103*, 083550–083550–4.

(58) Sen, A.; Sahu, D.; Ganguly, B. *J. Phys. Chem. B* **2013**, *117*, 9840–9850.
(59) Tang, H. **2012**.
(60) Xing, Y.; Chaudry, Q.; Shen, C.; Kong, K. Y.; Zhau, H. E.; Chung, L. W.; Petros, J. A.; O'Regan, R. M.; Yezhelyev, M. V.; Simons, J. W.; Wang, M. D.; Nie, S. *Nat. Protoc.* **2007**, *2*, 1152–1165.
(61) Nakajima, N.; Ikada, Y. *Bioconjug. Chem.* **1995**, *6*, 123–130.
(62) Kokkinis, A.; Valamontes, E. S.; Raptis, I. *J. Phys. Conf. Ser.* **2005**, *10*, 401.
(63) Linder, V.; Gates, B. D.; Ryan, D.; Parviz, B. A.; Whitesides, G. M. *Small* **2005**, *1*, 730–736.
(64) Elliott, J. E.; Macdonald, M.; Nie, J.; Bowman, C. N. *Polymer* **2004**, *45*, 1503–1510.
(65) Argade, A. B.; Peppas, N. A. *J. Appl. Polym. Sci.* **1998**, *70*, 817–829.
(66) Ito, H. *J. Photopolym. Sci. Technol.* **2008**, *21*, 475–491.
(67) McCullough, A. W.; Vidusek, D. A.; Legenza, M. W.; de Grandpre, M.; Imhof, J. 1986; Vol. 0631, pp. 316–320.
(68) Brown, T.; Hunter, W. N.; Kneale, G.; Kennard, O. *Proc. Natl. Acad. Sci. U. S. A.* **1986**, *83*, 2402–2406.
(69) SantaLucia, J. *Proc. Natl. Acad. Sci.* **1998**, *95*, 1460–1465.
(70) Frank-Kamenetskii, M. D. *Biopolymers* **1971**, *10*, 2623–2624.
(71) Schildkraut, C.; Lifson, S. *Biopolymers* **1965**, *3*, 195–208.
(72) Davey, J. C.; Becker, K. B.; Schneider, M. J.; Germain, D. L. S.; Galton, V. A. *J. Biol. Chem.* **1995**, *270*, 26786–26789.
(73) Lorenz, H.; Despont, M.; Fahrni, N.; Brugger, J.; Vettiger, P.; Renaud, P. *Sens. Actuators Phys.* **1998**, *64*, 33–39.
(74) Jo, B.-H.; Beebe, D. J. 1999; Vol. 3877, pp. 222–229.
(75) Lee, S. W.; Lee, S. S. *Microsyst. Technol.* **2008**, *14*, 205–208.
(76) Bassett, D. W.; Taylor, J. C.; Conley, W.; Willson, C. G.; Bonnecaze, R. T. 2006; Vol. 6154, p. 61544P–61544P–8.
(77) Broguière, N.; Pinedo Rivera, T.; Pépin-Donat, B.; Nicolas, A.; Peyrade, D. *Microelectron. Eng.* **2011**, *88*, 1821–1824.
(78) Diehl, F.; Li, M.; He, Y.; Kinzler, K. W.; Vogelstein, B.; Dressman, D. *Nat. Methods* **2006**, *3*, 551–559.

Vita

Ryan Deschner graduated from the University of Texas at Austin with a B.S. in Chemical Engineering and, afterwards, worked for IBM in the Semiconductor Research and Development Center in East Fishkill, NY for four years. In 2008, he returned to the University of Texas at Austin to pursue his graduate work under Professor C. Grant Willson. After graduation, Ryan plans to work for NanoHybrids, Inc., a start-up company in the biotechnology sector.

Permanent Address: ryandeschner@gmail.com

This manuscript was typed by the author.